DOCTORAL THESIS

ASSESSMENT OF MATERIAL MODELS FOR SOIL AND APPLICATION TO SIMULATION OF NATM TUNNELING

DISSERTATION

BEWERTUNG VON MATERIALMODELLEN FÜR BÖDEN UND ANWENDUNG AUF SIMULATIONEN DER NATM TUNNELBAUWEISE

ausgeführt zum Zwecke der Erlangung des akademischen Grades einer
Doktorin der technischen Wissenschaften

eingereicht an der Technischen Universität Wien
Fakultät für Bauingenieurwesen

von

Dipl.-Ing. Yvonne Spira
Matrikelnummer 9726823
Webergasse 24/5, 1200 Wien, Österreich

Referent: O.Univ.Prof. Dipl.-Ing. Dr.techn. Dr.h.c.mult. Herbert Mang, Ph.D.
Institut für Mechanik der Werkstoffe und Strukturen
Technische Universität Wien
Karlsplatz 13/202, 1040 Wien, Österreich

Koreferent: Ass. Prof. Annamaria Cividini
Dipartimento di Ingegneria Strutturale
Politecnico di Milano
Piazza Leonardo da Vinci 32 - 20133 Milano, Italia

Wien, im November 2004

Acknowledgement

encouragement of some very special friends, I would not have finished the present work. Thank you very much!

Kurzfassung

In bevölkerungsreichen Gebieten, die sich durch eine hohe Bebauungsdichte auszeichnen, gibt es einen steigenden Bedarf an unterirdischer Erweiterung bestehender Infrastruktur, wie beispielsweise für Strecken des öffentlichen Verkehrs oder des motorisierten Individualverkehrs. Um Anforderungen nach Anschlüssen an bestehende Infrastruktur zu erfüllen, wird eine flexible Bauweise wie die Neue Österreichische Tunnelbaumethode gefordert. Diese Methode nutzt Kriechverformungen im Boden zur Aktivierung des Untergrundes als tragendes Element für den Tunnel. Die eingebrachte Spritzbetonschale kann aufgrund der sich entwickelnden Steifigkeit und Festigkeit der Einwärtsbewegung des Bodens zumehmend widerstehen. Zudem ist zur Vermeidung von Schäden an bestehender Bebauung oder Infrastruktur die Minimierung von Bodenverformungen und Oberflächensetzungen essentiell. Zu diesem Zweck wird vielfach Bodenverbesserung vorgenommen. Die beschriebenen Tunnelvortriebsmethoden sind durch eine starke Boden/Stützmittel Interaktion gekennzeichnet, in welcher die eingebundenen hydrierenden jungen zementbasierten Materialien sowie die Bodenart und ihre spezifischen Eigenschaften wesentlich sind.

In dieser Arbeit wird ein Überblick über das Verhalten granularer und kohäsiver Böden gegeben. Darauf basierend werden elasto-viskoplastische Materialmodelle entwickelt. Zur Beschreibung granularer Böden werden nicht-assoziierte Drucker-Prager und Mohr-Coulomb Materialmodelle gewählt, die reibungsbehaftete Ver- und Entfestigung unter Schubbeanspruchung berücksichtigen. Regularisierung des Entfestigungsastes ist über das *charakteristische Längenkonzept* beschrieben. Zeitabhängige Prozesse werden mit der Duvaut-Lions Formulierung viskoplastischer Tragwerksantwort berücksichtigt. Auf der anderen Seite wird kohäsives Bodenverhalten mit einem Cam-Clay Materialmodell beschrieben, das der *critical state* Theorie entstammt. Basierend auf Ergebnissen hydrostatischer Kompressionstests werden volumetrisches Ver-und Entfestigungsverhalten und nichtlinear elastisches Verhalten erhalten. Zusätzlich wird für Vergleichszwecke ein linear elastisches Gesetz formuliert. Für das Cam-Clay Modell wird die Perzyna Formulierung verwendet, um viskoplastisches Materialverhalten zu berücksichtigen.

Mit Hilfe von Nachrechnungen von Standard-Labortests wird die Fähigkeit der Modelle zur Wiedergabe experimentell beobachteten Verhaltens gezeigt. Zu diesem Zweck wurden an der Technischen Universität Graz Triaxialtests an granularem und kohäsivem Boden durchgeführt. Die erhaltenen Materialeigenschaften dienen als Eingangsparameter für die Nachrechnung von Laborversuchen zu Tunnelvortrieben. Hierbei werden Möglichkeiten und Grenzen der angewandten Regularisierungsmethode für Entfestigungsverhalten innerhalb von Finite Element Simulationen gezeigt.

Zum Schluß wird im Rahmen zweier Anwendungen die Interaktion für Vortriebsprozesse nach der Neuen Österreichischen Tunnelbaumethode auf Strukturebene untersucht. Hierfür werden Materialmodelle für junge zementbasierte Materialien eingesetzt, die an der Technischen Universität Wien entwickelt worden sind. Im Rahmen der ersten Anwendung wird das Strukturverhalten bei Einsatz von Bodenverbesserungsmaßnahmen mittels Hochdruck-Bodenvermörtelung in granularem, bzw. kohäsivem Boden untersucht. Im Rahmen des

zweiten Anwendungsbeispiels werden strukturelle Auswirkungen der Wahl des elastischen Gesetzes für Tunnelvortriebe in kohäsivem Boden ermittelt.

Abstract

In highly populated areas characterized by high density of constructions, there is an increasing need for subsurface extensions of infrastructure like routes for public transport or for motorized individual traffic. In order to satisfy demands on structural connections to other infrastructure, a flexible construction mode such as the New Austrian Tunneling Method is required. This method uses the creep deformation of the soil for the activation of the ground as primary support of the tunnel. The applied shotcrete lining increasingly resists the inward moving soil because of strength and stiffness evolution in consequence of hydration, and hence, leads to a limitation of soil deformation. Additionally, minimization of soil deformation and surface settlements is essential in order to avoid damage to existing buildings and infrastructure. For this purpose, ground improvement is frequently applied. The described tunneling processes are characterized by a strong soil/support interaction, in which the involved hydrating cement-based materials and the kind of soil and its individual characteristics are essential.

In this work, the behavior of granular and cohesive soil is reviewed, and elasto-viscoplastic material models are developed. For description of granular soil, non-associative Drucker-Prager and Mohr-Coulomb material models are chosen, accounting for frictional hardening/softening under shear loading. Regularization of the softening branch is performed by means of the *characteristic-length* concept. Time-dependent processes are considered via the Duvaut-Lions formulation of viscoplastic response. Cohesive soil behavior, on the other hand, is described by a Cam-Clay model, emanating from the *critical state theory*. Based on results from hydrostatic compression tests, volumetric hardening/softening and a non-linear elastic behavior evolve. Additionally, for comparison, a linear elastic law is formulated. For the Cam-Clay model, the Perzyna formulation is adopted to account for viscoplastic material behavior.

By means of recomputation of standard laboratory tests, the ability of the developed models to reproduce the observed experimental behavior is shown. For this purpose, triaxial tests on granular and cohesive soil were performed at the Graz University of Technology. The obtained material properties serve as input for recomputation of laboratory experiments on tunnel excavations, illustrating the possibilities and restrictions of the employed regularization technique for material softening within Finite Element simulations.

Finally, the structural interaction of the soil/support compound structure in tunneling processes according to the New Austrian Tunneling Method is investigated by means of two applications. Hereby, material models for early-age cement-based materials developed at the Institute for Strength of Materials, Vienna University of Technology, are used. In the first application, the structural performance of ground improvement by means of jet grouting in granular and cohesive soil, respectively, is studied. In the second application, structural effects of the choice of the elastic law in tunneling applications in cohesive soil are investigated numerically.

Contents

Chapter 1

Industrial context and aim of the work

Construction of extensions of urban infrastructure such as ways for motorized individual traffic or public transportation is frequently performed underground. Because of infrastructural requirements or safety reasons, the resulting tunnel constructions are characterized by variations of tunnel cross-sections and intersections with other tunnels or shafts. Hence, such underground structures require a rather flexible mode of construction.

The New Austrian Tunneling Method (NATM) has proved to be such a flexible and also economic tool for the construction of underground structures. When driving tunnels according to the NATM, after the excavation of a cross-section, shotcrete is applied onto the tunnel walls, constituting a thin, flexible shell. The NATM is characterized by a strong interaction between the hardening/creeping shotcrete shell and the viscous ground, exerting pressure onto the lining. The relatively large compliance of young shotcrete is the source for the deformations required for the activation of the load-carrying capacity of the surrounding ground. In urban areas, however, these deformations must be minimized in order to avoid damage of buildings and infrastructure. In order to achieve this goal, the load-carrying capacity of the soil surrounding the tunnel may be improved by means of ground improvement like grouting or soil freezing.

Hence, the investigation of the interaction between the apparent ground and the hardening shotcrete lining is essential for the estimation of stability of the excavation and other important issues like the loading of the lining, the expected surface settlements or displacements of the tunnel cross-section. Furthermore, an evaluation of the effect of ground improvement prior to excavation on the surface settlements is highly desirable in order to assess the benefits gained from the planned additional support means.

Consequently, the present work aims at an elucidation of the soil-support interaction. Additionally, an increased understanding of the complex structural interaction between the hardening shotcrete shell and the viscous ground allows the optimization of support means with respect to apparent ground conditions. Such optimization may increase the high economy of NATM tunneling.

This work is organized as follows: Chapter 2 serves as an introduction to tunneling practice and computational mechanics, demonstrating the necessity of application of simplifications for numerical simulations of tunnel construction processes.

In Chapter 3, experimentally observable behavior of soil and and its numerical modeling by means of the plasticity theory is dealt with. Herein, constitutive models describing the behavior of granular and cohesive soil are contained. Also, numerical problems arising from formulations of the chosen material models are shortly addressed in this Chapter.

The proposed material models are assessed in Chapter 4 by means of numerical simulations of laboratory experiments on tunnel failure.

Applications of the proposed material models for soft soil are presented in Chapter 5 by means of numerical simulations of tunneling processes. Herein, effects of ground improvement in different geological conditions are investigated as well as the role of nonlinear elasticity for tunnel construction processes.

Chapter 6 contains a short summary and some conclusions.

Chapter 2

Tunneling practice and computational mechanics

In this Chapter, current tunneling practice using the NATM will be outlined in order to illustrate the strong ground-support interaction. Additionally, the possibilities and restrictions of computational mechanics will be elucidated. For this purpose, the set-up of the geometrical model, the choice of the material model, and the accessibility of information about the ground will be discussed. On this basis, the necessity of simplifications will become plausible. The resulting restrictions concerning the quality of the obtained results will be illustrated. Finally, the benefits gained from simplified computation of soil-structure interaction will be pointed out.

This Chapter serves as a foundation for the choice of the material models described in Chapter 3 and for the choice of the simplifications made in the numerical simulations (see Chapter 5).

2.1   Current tunneling practice

Today, two modes of excavation in soft soil are frequently used [57]: mechanized tunneling using tunnel boring machines (TBM), and the New Austrian Tunneling Method (NATM) with shotcrete.

For TBM tunneling, the soil behavior determines mainly the excavation speed and the means of excavation, but the lining of the tunnel is generally uniform. Hence, there is no essential interaction between the soil and the tunnel structure [57].

In contrast to TBM tunneling, the soil is the essential compound in NATM tunneling [61], as its creep properties are used to minimize the forces acting on the lining. It was already shown by Rabcewicz in 1944 [71] that tunnel excavation causes time-dependent changes in stresses and strains in the vicinity of the cross-section of the tunnel. The vanishing of the radial stresses along the surface of the excavation results in a stress-redistribution,

causing inelastic deformations connected with strain hardening or softening in the soil. Accordingly, a so-called *protection zone* around the tunnel develops.

Based on these observations, a profound knowledge of the behavior of the soil surrounding the excavation is required for an appropriate tunnel support installation. However, in practical applications, adaptations of the excavation process, such as the excavation speed and the excavation scheme, and adaptations of the applied tunnel support such as the thickness of the shotcrete lining, the application of anchors, soil freezing and/or jet grouting, are much in the hand of the experienced engineer at the construction site, who interprets the deformation field in the tunnel. Hence, the NATM is still applied in a largely empirical manner.

Nevertheless, static computations providing the stability of the tunnel construction are required. Unfortunately, the use of classical engineering calculation schemes using safety coefficients gives misleading results as regards the stresses in the soil and in the lining, as the occurring stress-redistributions are based on real soil and lining strength properties. For this reason, classical analyses fail. Anyway, a generally valid and accepted analysis for the safety of tunnel constructions is still missing [93].

However, there are many attempts and approaches to estimate the stability of an excavation by static computations. Considering the plane case, the required strength of the lining was e.g. estimated by hand calculations [14, 48]. Because of the bunch of simplifications, on which these hand calculations are based, their applicability is rather restricted. A more general approach is the use of the analysis of moving rigid bodies [19]. By computation of different possible failure mechanisms, a lower limit of the required lining strength can be found. Another approach is the use of connected rods and springs representing the tunnel lining and its foundation on an elastic half plane [95]. But again, consideration of the soil as a purely elastic medium is too restrictive for the general case. However, by now, the most promising tool for analysing the soil-lining interaction seems to be computational mechanics using the Finite Element Method (FEM). Generally, this tool is able to model arbitrary geometries as well as to account for various phenomena. Numerical analyses using the FEM can thus give good insight into the load-carrying behavior of the tunnel-support compound structure.

Therefore, the role of computational mechanics will be briefly discussed in the following subsection. The power of computer analyses will be pointed out. However, also deficiencies in numerical tools and drawbacks concerning applications to structural soil behavior will be mentioned.

2.2 Computational mechanics

The FEM is a powerful tool for computation of various tasks in engineering practice. Its applicability to a wide range of materials is undisputed. However, the application of the FEM to some materials such as soil is a topic of ongoing research, as is revealed by the vast number of different material models (elastoplastic models, damage models, hypoplastic

models, micromechanics models, etc.) in the open literature. The great number and the diversity of these models make clear that there is no consent on modeling of soil for various geomechanical tasks. Reasons for the difficulty of modeling soil behavior are the great number of different types of soil, i. e., rock, sand, gravel, clay, and organic, resulting in different characteristic material behavior, and the variety of phenomena existing in soil mechanics. These phenomena include, e. g., mechanical and transportation phenomena as well as hydromechanical and chemomechanical couplings. Therefore, it is generally accepted that the choice of the model depends on the specific problem to be solved.

Hence, sophisticated modeling of an excavation process is a challenging task. Apart from the modeling of the occurring phenomena, the applied structural model and the loading history have to account for the different construction stages and the applied support means.

As regards the numerical simulation of excavation processes, this work focusses on the basic time-dependent deformational behavior of soil, which will be modelled within the framework of elasto-viscoplasticity accounting for hardening and softening. By means of such simple models, basic differences of the structural behavior of two different soil types in excavation processes will be elaborated. Other phenomena will not be considered, in order not to extend the scope of this work. This restriction does not mean that these phenomena may not be investigated for special cases. Nevertheless, some phenomena which are considered to be of general relevance for excavation processes, and their numerical modeling shall be discussed in a separate paragraph.

Results from numerical simulations based on very sophisticated models are only as good as the quality of the input data. In the author's view, this is one of the most severe drawbacks concerning the relevance of numerically obtained results from the simulation of tunneling processes. Profound knowledge about the soil surrounding the excavation is essential as concerns the deformational behavior of the soil. Unfortunately, essential constituents for such a profound knowledge, like spatial distributions of soil types and respective soil properties, present water conditions, *in-situ* stresses and anisotropies, as well as the existence of inhomogeneities and their respective characteristics, are not exactly quantified for tunneling projects, as the required effort would be too expensive and time-consuming. Instead, estimates from experience and geologic information as well as interpolation from pointwise estimated data are used as input. Consequently, results from numerical simulation of tunneling can only provide an approximation or estimate of the real structural behavior.

The above discussion already indicates that numerical simulation of tunneling processes aims more at qualitative rather than quantitative results. Consequently, this work seeks to contribute to basic qualitative insight into the structural ground-support interaction in consequence of excavation under different geologic conditions. In this respect, use of simple material models and simplifications of the structural model are justified in order to obtain a qualitative insight into the different structural behavior. Finally, simplified analyses are very economic, as comparative studies can be performed in order to obtain information concerning the benfits gained from chosen construction schemes or from application of additional tunnel support means.

Discussion on some phenomena occurring in tunneling processes and on their respective numerical modeling for FE computations. First of all, most natural soils exhibit anisotropic behavior in consequence of former consolidation processes or other non-isotropic loading. Hence, material anisotropy should be accounted for in a numerical model. Unfortunately, although elastic and inelastic anisotropy can mathematically be handled [98, 18], less academic applications than recomputation of laboratory experiments [29, 51] can rarely be found in the open literature because of lack of robustness of the numerical models. Moreover, the physical significance and the ability to determine parameters describing the anisotropy may not be available. However, the information gained from consideration of anisotropy is not seen to compensate the uncertainties introduced into the material model. For these reasons, material anisotropy is left out of the scope in this work.

Often, there are also relevant changes of soil properties resulting from the presence of water in the ground observed in experiments. Additionally, excavation in moist or wet ground can cause flow of water which can crucially alter the settlements. Numerically, such hydromechanical couplings can be accounted for by application of porous media theory. Here, the pores of a continuum with internal structure are filled with fluid and/or gaseous phases [55]. A thermodynamically founded continuum approach of this theory can be found in [17]. Although hydromechanical couplings can alter the structural behavior crucially, they will not be considered in this work, as this work primarily aims at the basic interaction between soil and tunnel structure. However, for future work such couplings should definitely be accounted for.

As regards the rate-independent mechanical behavior of soil, the models used in this work will be based on classical elasto-plasticity for its foundation on the concept of therodynamics.

A basic property of soils which possibly has the greatest impact on the structural behavior of NATM tunnel excavations, is the time-dependence of the soil deformations. Almost as manifold as the possibilities for modeling the rate-independent soil behavior, are the possiblities for modeling the time-dependence of soil behavior. Phenomenological approaches like rheological models are used as well as functions describing experimentally observed 1D creep curves. Additionally, models from fluid dynamics as well as from classical viscoplasticity are applied. However, the present work is concerned with classical elasto-plasticity. Hence, the application of classical viscoplasticity models is a natural choice. Besides, phenomenological models, often successfully applied to settlement situations, are one-dimensional. This is certainly not the case for tunneling.

Finally, tunnel excavation, especially near the surface, can lead to the development of shear bands if the shear resistance of the material is exceeded. Such shear bands can lead to failure of the entire structure. Hence, modeling of shear bands is an important feature within the framework of numerical modeling of tunneling situations. Since the 1990's, numerical mathematical tools for the initiation and formation of shear bands have been developed. The works from [63, 64, 72] are leading in this field. They report on the good performance of numerical models for the simulation of shear band initiation and

propagation, for plane examples. Nevertheless, a satisfactory theory for three-dimensional computation and for applications to respective structural situations are still missing. Since tunneling is a three-dimensional process, and since shear bands tend to develop around the tunnel face, pertinent three-dimensional solution strategies are essential. However, as there is currently no satisfactory solution of the general problem, and as presented indicators for material failure are strongly model-dependent, the modeling of such shear failure shall not be considered in this work, even though studies on failure of excavations will be shown later on in Chapter 4.

Chapter 3

Material modeling of soil

Material models are an essential tool to make numerical analysis of engineering structures feasible. As numerical analysis aims at realistic simulation of structural behavior under loading, the applied material description (material model) has to take the relevant features of the considered situation into account. Consequently, only an adequate description of the material renders realistic numerical simulations feasible.

Therefore, the first part of this Chapter illustrates experimentally observable soil behavior. Next, the theory of plasticity will be outlined to give insight into the numerical treatment of the modeling of materials. Then, two phenomenological material models describing the two limiting cases of soil mechanics, sands and clays, will be introduced. The essential material characteristics are captured by the chosen models. The required model parameters can be identified by means of a set of standard laboratory tests. Finally, these models will be verified by means of re-computation of laboratoy tests.

3.1   Soil behavior – experimental observations

Soil is a three-phase mixture, consisting of a solid, a fluid, and a gaseous phase. The solid skeleton consists of single particles which are different in form and size (see Figure 3.1). Such particles vary from very fine particles with a flat shape (see Figure 3.1(c)) to coarse particles with a more or less spherical shape (see Figure 3.1(a) and (b)). Typical representatives of both limiting cases are clayey soils and sands [87]. The gaseous phase usually consists of air; the fluid phase of water. A detailed general mechanical description of three-phase mixtures is contained in [46] and [17]. The different microscopic characteristics of sand and clay result in a different macroscopic behavior. In contrast to dry sand, clays exhibit cohesive behavior. This cohesive behavior follows from the adhesion of water on electrostatically loaded particles [33]. Both the frictional and the cohesive response of the material depend on the velocity of the applied load or applied deformation, the permeability of the soil, the degree of compaction, the arrangement of the particles and the water conditions [87]. The macroscopic description of sand and clay as a homogeneous and
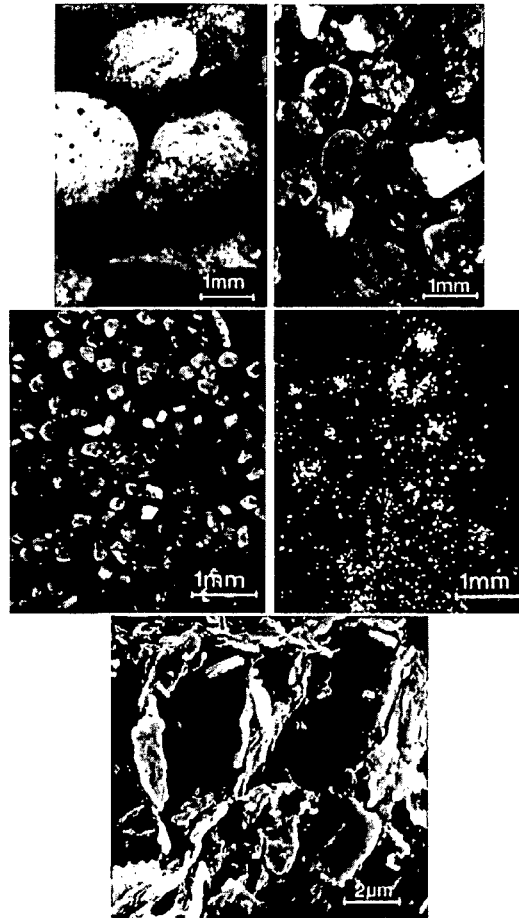
Figure 3.1: Material to be described in this work: upper 4 photographs show
            granular material like gravel or sand, consisting of spherical shaped parti-
            cles; the bottom photograph shows clayey material with small platy parti-
            cles

isotropic medium results in a characterization by means of volumetric and dilative stresses
and strains [46]. The material response is either reversible or irreversible, instantaneous
or delayed. Discontinuous fracture processes, however, need to be described in terms of
jumps in the displacement field (see e.g.[84]). Discontinuous failure in soil is always an
irreversible process. For a phenomenological description of the mechanical behavior of soil,
certain types of laboratory experiments as well as procedures for field measurements are
well established.
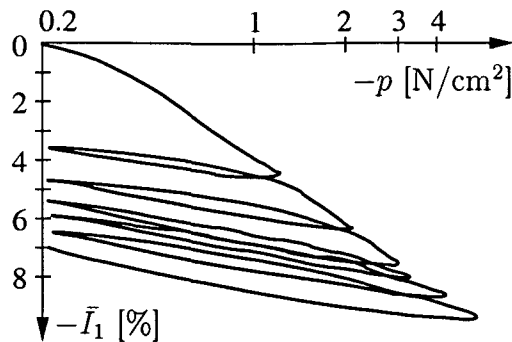
Figure 3.2: Relation between volumetric strain and effective hydrostatic pressure obtained from laboratory tests on Newfield clay (from [100])

3.1.1 Elastic behavior of sand and clay

Elastic material behavior in unloading and reloading paths is characterized by the absence of energy dissipation. Triaxial tests on dense and loose Fuji River sand (see e. g.[98]) or oedometer tests performed by Al-Tabaa (see e. g.[98]) on kaolin, support the classical split of the total strains into elastic strains during unloading and reloading and inelastic strains during loading. The volumetric strain - mean effective pressure curves $(-\bar{I}_1 - \log(-p))$ in Figure 3.2 (see e. g.[100]) obtained from Newfield clay exhibit quasi-elastic behavior in the unloading-reloading branches. The nearly linear relation of the unloading and reloading branches of the $-\bar{I}_1 - \log(-p)$ curve indicates pressure-dependence of the compression modulus. Consequently, also the shear modulus and/or Poisson's ratio must depend on the pressure. A shear modulus varying with the mean pressure was indeed found experimentally by Houlsby [41].

3.1.2 Inelastic behavior of sand and clay

Graham, Noonan and Lew [98] deduced yield- and loading surfaces (see Figure 3.3(a)) and vectors of plastic strains from triaxial tests performed on undisturbed Winnipeg clay. These surfaces represent the loci of the limit of elastic behavior in the $p - \sqrt{3J_2}$ space, where p is the effective hydrostatic pressure and $\sqrt{3J_2}$ is a measure of deviatoric stress.

Similar tests were performed by Poorooshasb, Holubec and Sherbourne (in e. g.[98]) (see Figure 3.3(b)) on dense Ottawa sand. Typical yield loci and experimentally obtained plastic strains are illustrated in Figure 3.3(b). The shapes of the yield surfaces differ considerably from the ones obtained for clay. The differences in the inelastic behavior of sand and clay reflects the different microstructural mechanisms of both materials: Sand particles exhibit sliding when subjected to shear loading. In clays, shear loading additionally results in an alignment of the particles during sliding.

However, similar compaction-dilation characteristics for sands and clays, which depend on the degree of particle compaction, are observed. The relation between the overconsolidation
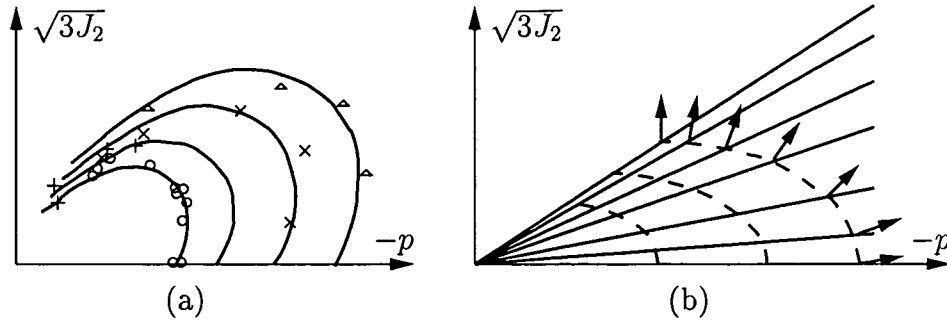
Figure 3.3: Inelastic behavior of clay and sand (from [98]): (a) Yield and loading surfaces obtained from undisturbed Winnipeg clay for different preconsolidation pressures ($\circ, +, x, \triangle$), from Graham, Noonan and Lew; (b) yield surfaces (–), plastic potentials (- -) and vectors of plastic strains obtained from dense Ottawa Sand

ratio and the volume change was investigated experimentally (see, e. g., the experimental work by Parry on Weald clay [66]). Overconsolidated soil exhibits volume increase during shear, whereas normally consolidated soil decreases in volume during shear.

Yielding of sands is characterized by irrecoverable changes in the particle arrangement [98]. Tests by Lade and Yamamuro on sands over a wide range of confining pressures (see [99, 52]) show that apart from the particle rearrangement in consequence of shear loading also particle crushing can be observed in case of high hydrostatic loading. However, when shear loading is the dominating influence, the stress ratio $\sqrt{3J_2}/p$ or the mobilized friction angle φ_{mob} are the driving effects for yielding.

Sands usually follow a non-associated flow rule: the plastic potentials do not coincide with the yield surfaces. If associated flow is assumed, then the plastic dilation is larger than the one observed for sands.

Furthermore, experiments from Desrues and Hammad [21] on loose and dense sands show that the friction angle φ and the dilatancy angle ψ are dependent of the inital density of the material and of the preconsolidation pressure. Therefore, the friction and dilatancy angles have an influence on the direction of shear bands in case of localized deformation.

3.1.3 Viscous material behavior of sand and clay

Generally speaking, the time-dependent deformational behavior of soil has two sources: water in the soil, on the one hand, and a delayed straining of the solid particles, on the other hand [25, 50, 33]. In the present work, only drained conditions and slow application of the load (i. e., no strain rate effects) will be taken into consideration. Pore pressure development or diffusion processes are topics addressed elsewhere [16, 65]. Because of the assumed drained conditions, only the water bound to the solid particles causes time-dependent effects. Flat and platy shaped particles rather than spherically shaped particles exhibit adhesive forces. As a consequence of electrostatic loading, water may be bound

to these particles [33]. Therefore, the release of water in cohesive materials under loading conditions is time-dependent.

Lade and Liu [50] have performed experimental studies on drained Antelope Valley sand. They concluded that viscous behavior exists also for cohesionless, frictional materials in form of delayed straining of the solid skeleton. In experimental investigations, viscoelastic as well as viscoplastic deformations are observed [32]. Viscoelastic response was detected by Leinenkugel (see e. g.[32]). The viscoplastic deformational behavior of soil, investigated by means of creep and consolidation tests of clay and sand specimens, is documented in the literature (see e. g.[50, 6]).

Considering consolidation, two processes can be observed in the soil: First, during primary consolidation, the change of pore water pressures with time in consequence of the flow of water in the pores can be observed. Consequently, primary consolidation is a diffusion process for drained conditions [98]. Next, creep or secondary consolidation is characterized by the readjustment of particle contacts at essentially constant effective stresses.

Other time effects that are relevant to soil mechanics are, e. g., the cementation between particles or other aging phenomena like weathering. These effects will not be discussed in this work.

3.2 Constitutive modeling of soil: Plasticity theory

In this Section, the theory of plasticity will be reviewed in order to elucidate the algorithmic treatment of the chosen material models. First, classical rate-independent plasticity including multi-surface plasticity will be introduced. The algorithmic treatment will be outlined subsequently by elaboration of the time integration and of the algorithmic elastoplastic moduli, which describe the stress-strain relationship for discrete displacement increments in elasto-plastic processes. Next, the extension to viscoplasticity will be presented to account for the time-dependent behavior of soft soil.

3.2.1 Classical rate-independent plasticity

The modeling of the behavior of soil is considered in this work in the framework of geometrically linear theory. This implies an additive decomposition of the total strains into an elastic and a plastic part:

$$\varepsilon = \varepsilon^e + \varepsilon^p .$$ (3.1)

The basic governing equations for general rate independent plasticity theory are summarized in the following (see also [79]). The equations already include the case of the elastic domain being described by more than one yield or loading function. This case is called multi-surface plasticity.

Elastic stress-strain relations, derived from the hyperelastic law, can be formulated as

$$\boldsymbol{\sigma} = \partial_{\boldsymbol{\varepsilon}^e} \mathcal{W}(\boldsymbol{\varepsilon}^e) \; ; \tag{3.2}$$

$$\mathbf{C} = \partial^2_{\boldsymbol{\varepsilon}^e \boldsymbol{\varepsilon}^e} \mathcal{W}(\boldsymbol{\varepsilon}^e) \; . \tag{3.3}$$

Here, $\mathcal{W}(\boldsymbol{\varepsilon}^e)$ denotes the elastic potential of stored energy, and $\boldsymbol{\sigma}$ and $\mathbf{C}$ are the stress and the elastic tangent modulus, respectively. Hence, a general constitutive relation can be written in differential form as $d\boldsymbol{\sigma} = \mathbf{C} d\boldsymbol{\varepsilon}^e$. For a constant elastic modulus, $\boldsymbol{\sigma} = \mathbf{C}\boldsymbol{\varepsilon}^e$ holds. The elastic domain in the stress space is given for the general case of multi-surface plasticity as:

$$\mathbb{E}_{\boldsymbol{\sigma}} = \{\boldsymbol{\sigma} \; : \; f_k(\boldsymbol{\sigma}, \mathbf{q}) \leq 0 \text{ for } k = 1, \ldots, m\} \; , \tag{3.4}$$

with the vector $\mathbf{q}$ containing the stress-like internal variables, $\mathbf{q} = \{q_1, \ldots, q_m\}^T$. m is the number of yield surfaces defining the closed elastic domain in the stress space.

A general form of the evolution equation for plastic strains, the so-called flow rule, reads, for the case of multi-surface plasticity, according to Koiter [47]

$$\dot{\boldsymbol{\varepsilon}}^p = \sum_{k=1}^{m_{act}} \gamma_k \, \mathbf{r}_k(\boldsymbol{\sigma}, \mathbf{q}) \; , \tag{3.5}$$

where $\mathbf{r}$ are functions describing the direction of plastic flow and γ is a Lagrangian multiplier denoting the amount of plastic flow. m_{act} stands for the number of active yield surfaces (with $m_{act} \leq m$).

The evolution equation for hardening/softening behavior can be formulated as

$$\dot{\boldsymbol{\alpha}} = \sum_{k=1}^{m_{act}} \gamma_k \, \mathbf{h}_k(\boldsymbol{\sigma}, \mathbf{q}) \; . \tag{3.6}$$

Here, $\mathbf{h}_k$ are prescribed functions defining the type of hardening, and $\boldsymbol{\alpha}$ is the vector of strain-like internal variables, $\boldsymbol{\alpha} = \{\alpha_1, \ldots, \alpha_m\}^T$. The vectors of the stress-like and strain-like internal variables $\mathbf{q}$ and $\boldsymbol{\alpha}$ are related by a constitutive hardening law, which can be written in differential form as $d\mathbf{q} = -\mathbf{D} d\boldsymbol{\alpha}$, with $\mathbf{D}$ standing for the hardening/softening modulus.

Finally, the Kuhn-Tucker loading/unloading conditions and the consistency condition read as

$$f_k(\boldsymbol{\sigma}, \mathbf{q}) \leq 0 \; , \quad \gamma_k \geq 0 \; , \quad \gamma_k f_k(\boldsymbol{\sigma}, \mathbf{q}) = 0 \; ; \tag{3.7}$$

$$\gamma_k \dot{f}_k(\boldsymbol{\sigma}, \mathbf{q}) = 0 \; . \tag{3.8}$$

3.2.2   Time integration: Return Map Algorithm

In the course of the global Newton-Raphson iteration for the load increment $n + 1$, $t_n \leq t \leq t_{n+1}$, the total and the plastic strains and the internal variables are assumed to be known at the time instant $t = t_n$:

$$\{\boldsymbol{\varepsilon}_n, \boldsymbol{\varepsilon}_n^p, \boldsymbol{\alpha}_n\} \text{ given data at time } t_n \; . \tag{3.9}$$

Time integration of the evolution laws for the plastic strains and the internal strain-like variables is performed for a prescribed displacement increment $\Delta \mathbf{u}$. The problem may be formulated as follows:

> Find the set of history variables $\{\boldsymbol{\varepsilon}^p_{n+1}, \boldsymbol{\alpha}_{n+1}\}$ for the prescribed total strains
> $\boldsymbol{\varepsilon}_{n+1} = \boldsymbol{\varepsilon}_n + \boldsymbol{\nabla}^s(\Delta \mathbf{u})$ according to the discrete form of the Kuhn-Tucker conditions

$$f_k(\boldsymbol{\sigma}_{n+1}, \mathbf{q}_{n+1}) \leq 0 \ , \quad \Delta\gamma_{k,n+1} \geq 0 \quad \text{and} \quad \Delta\gamma_{k,n+1} f_k(\boldsymbol{\sigma}_{n+1}, \mathbf{q}_{n+1}) = 0 \ . \quad (3.10)$$

An implicit integration scheme, the backward Euler scheme[1], is used for the integration of the evolution equations, yielding

$$\boldsymbol{\varepsilon}^p_{n+1} \ = \ \boldsymbol{\varepsilon}^p_n + \int_{t_n}^{t_{n+1}} \dot{\boldsymbol{\varepsilon}}^p dt = \boldsymbol{\varepsilon}^p_n + \dot{\boldsymbol{\varepsilon}}^p_{n+1}\Delta t_{n+1} = \boldsymbol{\varepsilon}^p_n + \sum_{k \in J_{act}} \Delta\gamma_{k,n+1}\mathbf{r}_k(\boldsymbol{\sigma}_{n+1}, \mathbf{q}_{n+1}) \quad (3.11)$$

$$\boldsymbol{\alpha}_{n+1} \ = \ \boldsymbol{\alpha}_n + \int_{t_n}^{t_{n+1}} \dot{\boldsymbol{\alpha}} dt = \boldsymbol{\alpha}_n + \dot{\boldsymbol{\alpha}}_{n+1}\Delta t_{n+1} = \boldsymbol{\alpha}_n + \sum_{k \in J_{act}} \Delta\gamma_{k,n+1}\mathbf{h}_k(\boldsymbol{\sigma}_{n+1}, \mathbf{q}_{n+1}) \quad (3.12)$$

with $\Delta\gamma_{k,n+1} = \Delta t_{n+1}\gamma_{k,n+1}$. Equations (3.11) and (3.12), together with the loading/unloading conditions $f_{k,n+1} \leq 0$, form a set of nonlinear equations for the unknowns $\Delta\gamma_{k,n+1}$, $\boldsymbol{\varepsilon}^p_{n+1}$ and $\boldsymbol{\alpha}_{n+1}$. Hence, the elastoplastic constitutive equations are reformulated by introducing a trial elastic state, which is obtained by freezing the plastic flow during the time step Δt_{n+1}:

$$\boldsymbol{\varepsilon}^{e,trial}_{n+1} \ := \ \boldsymbol{\varepsilon}_{n+1} - \boldsymbol{\varepsilon}^p_n \qquad\qquad (3.13)$$

$$\boldsymbol{\sigma}^{trial}_{n+1} \ := \ \boldsymbol{\sigma}\left(\boldsymbol{\varepsilon}^{e,trial}_{n+1}\right) \qquad\qquad (3.14)$$

$$\boldsymbol{\alpha}^{trial}_{n+1} \ := \ \boldsymbol{\alpha}_n \qquad\qquad (3.15)$$

$$f^{trial}_{k,n+1} \ := \ f_k\left(\boldsymbol{\sigma}^{trial}_{n+1}, \mathbf{q}^{trial}_{n+1}\right) \qquad\qquad (3.16)$$

Whether plastic loading or elastic unloading is occurring in the time increment Δt_{n+1}, is decided from the value of the yield function based on the trial state (see Equation (3.16)):

$$f^{trial}_{k,n+1} \ < \ 0 \ \Rightarrow \ \text{elastic step} \ \Leftrightarrow \ \Delta\gamma_{k,n+1} = 0 \ , \qquad (3.17)$$

$$f^{trial}_{k,n+1} \ \geq \ 0 \ \Rightarrow \ \text{plastic step} \ \Leftrightarrow \ \Delta\gamma_{k,n+1} > 0 \ . \qquad (3.18)$$

Here, Equation (3.18) also specifies the set of active yield surfaces J_{act} as (see [79])

$$J_{act} = \left\{ k \in 1, \ldots, m \mid f_k(\boldsymbol{\sigma}^{trial}_{n+1}, \mathbf{q}^{trial}_{n+1}) \geq 0 \ . \right\} \qquad (3.19)$$

---

[1]The backward Euler scheme is based on the generalized midpoint rule $\int_{t_n}^{t_{n+1}} f(t)dt = f(t_\xi) \int_{t_n}^{t_{n+1}} dt = f(t_\xi)\Delta t_{n+1}$, where t_ξ is taken at the end of the time increment $t_\xi = t_{n+1}$. This integration scheme is convergent, first-order accurate and unconditionally stable [79].

Equation (3.17) states that for the elastic step the assumption of frozen plastic flow holds. Consequently, the set of state variables is given as $\{\varepsilon_{n+1}^p, \alpha_{n+1}\} = \{\varepsilon_n^p, \alpha_n\}$. For the plastic step, the state variables have to be evaluated. Therefore, a general residual formulation for the state variables and for the violated yield criteria is applied, reading

$$
\mathbf{R}(\mathbf{x}) = \left\{ \begin{array}{c} R^{\varepsilon^p} \\ \hline R^{\alpha} \\ \hline R^{f_k} \end{array} \right\} = \left\{ \begin{array}{c} -\varepsilon_{n+1}^p + \varepsilon_n^p + \sum_{k \in J_{act}} \Delta\gamma_{k,n+1} \mathbf{r}_{k,n+1} \\ -\alpha_{n+1} + \alpha_n + \sum_{k \in J_{act}} \Delta\gamma_{k,n+1} \mathbf{h}_{k,n+1} \\ \hline f_{k,n+1} \end{array} \right\} = 0 , \qquad (3.20)
$$

where $(\cdot)_{k,n+1} = (\cdot)_k(\sigma_{n+1}, \mathbf{q}_{n+1})$. Solving Equation (3.20) with a Newton scheme $\mathbf{R} + (d\mathbf{R}/d\mathbf{x})\Delta\mathbf{x} = 0$, where $\mathbf{x} = (\varepsilon_{n+1}^p, \alpha_{n+1}|\Delta\gamma_{k,n+1})^T$, and using the differential (infinitesimally incremental) constitutive law $-d\varepsilon_{n+1}^p = \mathbf{C}_{n+1}^{-1} d\sigma_{n+1}$ and the differential (infinitesimally incremental) hardening law $-d\alpha_{n+1} = \mathbf{D}_{n+1}^{-1} d\mathbf{q}_{n+1}$ yields

$$
\mathbf{R} + \left[\begin{array}{c|c} \mathbf{A}^{-1} & \nabla g_k \\ \hline \nabla f_k^T & 0_{kk} \end{array} \right] \left[\begin{array}{cc|c} -\mathbf{C}_{n+1} & 0 & 0 \\ 0^T & -\mathbf{D}_{n+1} & 0 \\ \hline 0^T & 0^T & 1_{kk} \end{array} \right] \left\{ \begin{array}{c} \Delta\varepsilon_{n+1}^p \\ \Delta\alpha_{n+1} \\ \hline \Delta(\Delta\gamma_{k,n+1}) \end{array} \right\} = 0 , \qquad (3.21)
$$

where $\mathbf{A}^{-1}$, ∇f_k, and ∇g_k are given as

$$
\mathbf{A}^{-1} = \left\{ \left[\begin{array}{cc} \mathbf{C}_{n+1}^{-1} & 0 \\ 0^T & \mathbf{D}_{n+1}^{-1} \end{array} \right] + \left[\begin{array}{cc} \sum_{k \in J_{act}} \Delta\gamma_{k,n+1} \partial_\sigma \mathbf{r}_{k,n+1} & \sum_{k \in J_{act}} \Delta\gamma_{k,n+1} \partial_q \mathbf{r}_{k,n+1} \\ \sum_{k \in J_{act}} \Delta\gamma_{k,n+1} \partial_\sigma \mathbf{h}_{k,n+1} & \sum_{k \in J_{act}} \Delta\gamma_{k,n+1} \partial_q \mathbf{h}_{k,n+1} \end{array} \right] \right\}
$$
$$
(3.22)
$$

$$
\nabla f_k = \left\{ \begin{array}{c} \partial_\sigma f_{k,n+1} \\ \partial_q f_{k,n+1} \end{array} \right\} , \qquad \nabla g_k = \left\{ \begin{array}{c} \mathbf{r}_{k,n+1} \\ \mathbf{h}_{k,n+1} \end{array} \right\} . \qquad (3.23)
$$

Note that the differentials $d\varepsilon_n^p$, $d\alpha_n$ and $d\varepsilon_{n+1}$ become zero, as ε_n^p, α_n and ε_{n+1} remain constant during time integration.

The increments of the plastic strains, internal variables, and of the consistency parameter follow from reformulation of Equation (3.21) as

$$
\left\{ \begin{array}{c} \Delta\varepsilon_{n+1}^p \\ \Delta\alpha_{n+1} \\ \hline \Delta(\Delta\gamma_{k,n+1}) \end{array} \right\} = - \left(\left[\begin{array}{c|c} \mathbf{A}^{-1} & \nabla g_k \\ \hline \nabla f_k^T & 0_{kk} \end{array} \right] \left[\begin{array}{cc|c} -\mathbf{C}_{n+1} & 0 & 0 \\ 0^T & -\mathbf{D}_{n+1} & 0 \\ \hline 0^T & 0^T & 1_{kk} \end{array} \right] \right)^{-1} \mathbf{R} . \qquad (3.24)
$$

The updated plastic strains, strain-like internal variables, and the consistency parameter read

$$
\varepsilon_{n+1}^p = \varepsilon_n^p + \Delta\varepsilon_{n+1}^p , \qquad (3.25)
$$

$$
\alpha_{n+1} = \alpha_n + \Delta\alpha_{n+1} , \qquad (3.26)
$$

$$
\Delta\gamma_{k,n+1} = \Delta\gamma_{k,n} + \Delta(\Delta\gamma_{k,n+1}) . \qquad (3.27)
$$

After the projection of the stress point onto the yield surface, a check of the active yield surfaces has to be performed. In case the assumed set of active yield surfaces before projection (J_{act}^i) is not equal to the set of active yield surfaces after projection (J_{act}^{i+1}), a repetition of the return map algorithm is required with the new set of active yield surfaces.

3.2.3   Consistent linearization. Elastoplastic moduli

An important advantage of the described algorithm is that it can be directly linearized in closed form [83]. This leads to the notion of consistent tangent stiffness matrices for the case of elastoplasticity. For the purpose of determining these matrices, the discrete residuum (see Equation (3.20)) yields $\mathbf{R}(\varepsilon_{n+1}^p, \alpha_{n+1} | \Delta\gamma_{k,n+1}) = \mathbf{0}$. Linearization of the time integration scheme, i. e., using the condition $d\mathbf{R}(\varepsilon_{n+1}^p, \alpha_{n+1} | \Delta\gamma_{k,n+1}) = \mathbf{0}$ yields

$$
\left[
\begin{array}{c|c}
\mathbf{A}^{-1} & \boldsymbol{\nabla} g_k \\
\hline
\boldsymbol{\nabla} f_k^T & \mathbf{0}_{kk}
\end{array}
\right]
\left\{
\begin{array}{c}
d\boldsymbol{\sigma}_{n+1} \\
d\mathbf{q}_{n+1} \\
\hline
d\left(\Delta\gamma_{k,n+1}\right)
\end{array}
\right\}
-
\left\{
\begin{array}{c}
d\boldsymbol{\varepsilon}_{n+1} \\
0 \\
0_k
\end{array}
\right\}
= \mathbf{0} ,
\tag{3.28}
$$

where the differential form of the constitutive law $-d\varepsilon_{n+1}^p = \mathbf{C}_{n+1}^{-1} d\boldsymbol{\sigma}_{n+1} - d\boldsymbol{\varepsilon}_{n+1}$ and of the hardening law $-d\boldsymbol{\alpha}_{n+1} = \mathbf{D}_{n+1}^{-1} d\mathbf{q}_{n+1}$ are applied. Note that $d\boldsymbol{\varepsilon}_{n+1} \neq \mathbf{0}$.

Solving Equation (3.28) for $\{d\boldsymbol{\sigma}_{n+1}, d\mathbf{q}_{n+1}\}^T$ finally gives the relation for the elastoplastic tangent modulus, which can be extracted from the relation

$$
\left\{
\begin{array}{c}
d\boldsymbol{\sigma}_{n+1} \\
d\mathbf{q}_{n+1}
\end{array}
\right\}
=
\left[\mathbf{A} - g_{kl}^{inv}\mathbf{A}\boldsymbol{\nabla} g_k \boldsymbol{\nabla} f_l^T \mathbf{A}\right]
\left\{
\begin{array}{c}
d\boldsymbol{\varepsilon}_{n+1} \\
0
\end{array}
\right\} ,
\tag{3.29}
$$

where

$$
g_{kl} = \boldsymbol{\nabla} f_k^T \mathbf{A} \boldsymbol{\nabla} g_l .
\tag{3.30}
$$

3.2.4   Extension to account for viscoplastic behavior

A basic difference between viscoplasticity, i. e., rate-dependent plasticity, and rate-independent plasticity is that the former model allows stress-states outside the elastic domain. Hence, classical viscoplasticity may be interpreted as a regularization of rate-independent plasticity, as the viscoplastic answer lies between the elastic answer and the rate-independent plastic answer. The extension to viscoplasticity is shown for the one-dimensional case by the following evolution equations for plastic flow and hardening

$$
\dot{\varepsilon}^{vp} = \frac{\langle f(\sigma, q)\rangle}{\eta} \partial_\sigma f
\tag{3.31}
$$

$$
= \frac{1}{\eta}(\sigma - \sigma_\infty) ,
\tag{3.32}
$$

$$\dot{\alpha} = \frac{\langle f(\sigma, q) \rangle}{\eta} \partial_q f \tag{3.33}$$

$$= \frac{1}{\eta}(q - q_\infty), \tag{3.34}$$

where η [Pa s] shall denote a constant viscosity parameter throughout this work, $\langle \cdot \rangle$ represents the McAuley brackets, and σ_∞ and q_∞ are the stress response and the internal stress-like response for the inviscid case. The Equations (3.31) and (3.33) are known as the viscoplastic and hardening constitutive equations by Perzyna [79], whereas the reformulations in Equations (3.32) and (3.34) are ascribed to Duvaut and Lions [23]. Instead of Equation (3.32), often the characteristic time $\tau = \eta/E$ [s] is introduced in the evolution of plastic flow, yielding

$$\dot{\varepsilon}^{vp} = \frac{E^{-1}}{\tau}(\sigma - \sigma_\infty) . \tag{3.35}$$

Accordingly, the evolution of the hardening variable is postulated as

$$\dot{\alpha} = \frac{D^{-1}}{\tau}(q - q_\infty) . \tag{3.36}$$

The choice of this simple type of viscoplastic model is supported by experimental observations [50], indicating that the shape representing the viscoplastic potential differs only little from the respective shape of the plastic potential for the inviscid case. Additionally, the extension of the Duvaut-Lions and Perzyna formulations to multi-dimensional stress-states is straightforward. First, for models of the Perzyna type, the constitutive evolution equations for viscoplastic strains and hardening can be postulated in a general formulation as [80]

$$\dot{\varepsilon}^{vp} = \frac{\langle f(\boldsymbol{\sigma}, \mathbf{q}) \rangle}{\eta} \mathbf{r}(\boldsymbol{\sigma}, \mathbf{q}) \tag{3.37}$$

$$\dot{\alpha} = \frac{\langle f(\boldsymbol{\sigma}, \mathbf{q}) \rangle}{\eta} \mathbf{h}(\boldsymbol{\sigma}, \mathbf{q}) , \tag{3.38}$$

where $\mathbf{r}$ and $\mathbf{h}$ are again functions describing the direction of plastic flow and the type of hardening, respectively (see Section 3.2.1). For the special case of associated plasticity, $\mathbf{r} = \partial_{\boldsymbol{\sigma}} f$ and $\mathbf{h} = \partial_{\mathbf{q}} f$ hold.

Second, for the general case of multidimensional states of stress, the evolution equations for viscoplastic strains and hardening are postulated for the Duvaut-Lions model [80] in the form

$$\dot{\varepsilon}^{vp} = \frac{1}{\tau} \mathbf{C}^{-1}(\boldsymbol{\sigma} - \boldsymbol{\sigma}_\infty) , \tag{3.39}$$

$$\dot{\alpha} = \frac{1}{\tau} \mathbf{D}^{-1}(\mathbf{q} - \mathbf{q}_\infty) , \tag{3.40}$$

with τ [s] denoting a fluidity parameter[2], and $\mathbf{C}$ and $\mathbf{D}$ representing the elastic tangent modulus and the hardening modulus, respectively.

The algorithmic treatment of both models will be outlined in the following Section.

3.2.5   Time integration for viscoplasticity

This Section will be separated in two parts, as both viscoplastic formulations have special advantages and disadvantages for application to single-surface/multi-surface plasticity combined with linear/nonlinear elasticity.

On the one hand, it is shown in [80] that the application of a Perzyna model to multisurface plasticity with non-smooth intersecting yield surfaces gives incorrect results in the projection scheme, as *all* violated yield function values contribute to the evolution of of plastic strains, i.e. there is no check whether each violated yield surface is ultimately active. On the contrary, the Duvaut-Lions model yields the correct answer because of the interpolation between the elastic and the rate-independent plastic answer.

On the other hand, the Duvaut-Lions model uses the elastic tangent modulus for determination of the plastic strain rate. Hence, the application of a nonlinear elastic law $\boldsymbol{\sigma} = \boldsymbol{\sigma}(\boldsymbol{\varepsilon}^e)$ with an elastic tangent modulus $\mathbf{C} = \mathbf{C}(\boldsymbol{\varepsilon}^e)$, where $\dot{\boldsymbol{\sigma}} \neq \mathbf{C}\dot{\boldsymbol{\varepsilon}}^e$, requires an iterative solution. In the course of a Newton scheme, among others, the derivative of the elastic tangent modulus with respect to the stresses is required, resulting in a 6th order tensor. Clearly, the accurate derivation of such a tensor can be quite tedious. However, the application of a Perzyna model results in a Newton scheme quite similar to the one obtained from the rate-independent solution. Thus, the algorithmic treatment of a Perzyna model is straightforward and rather simple.

The algorithmic treatment of the Duvaut-Lions model in linear elasticity and multisurface plasticity as well as the Perzyna model in nonlinear elasticity and single-surface plasticity will be illustrated in the following.

3.2.5.1   Time integration in linear elasticity for the Duvaut-Lions model

For the general case of multidimensional states of stress, the constitutive evolution equations for viscoplastic strains and hardening are postulated for the Duvaut-Lions model [80] in the form

$$\dot{\boldsymbol{\varepsilon}}^{vp} = \frac{1}{\tau}\mathbf{C}^{-1}(\boldsymbol{\sigma} - \boldsymbol{\sigma}_\infty) \ , \tag{3.42}$$

---

[2]Note that the fluidity parameter τ in Equation (3.39) is not equal to the characteristic time τ in Equation (3.35), as Equation (3.39) with $\tau = \eta/E$ would yield for an unconfined uniaxial viscoplastic loading

$$\dot{\boldsymbol{\varepsilon}}^{vp} = \frac{1}{\eta}E\mathbf{C}^{-1}(\boldsymbol{\sigma} - \boldsymbol{\sigma}_\infty) \ , \tag{3.41}$$

which only reduces to Equation (3.35) if Poisson's effects were zero. Therefore, the use of τ from now on will be in the sense of a fluidity parameter.

$$\dot{\boldsymbol{\alpha}} = \frac{1}{\tau}\mathbf{D}^{-1}(\mathbf{q} - \mathbf{q}_{\infty}) \ . \tag{3.43}$$

Here, τ [s] is a fluidity parameter.

The introduction of a linear elastic law and of its rate form yields

$$\boldsymbol{\sigma} = \mathbf{C}\left(\boldsymbol{\varepsilon} - \boldsymbol{\varepsilon}^{vp}\right) \ , \tag{3.44}$$

$$\dot{\boldsymbol{\sigma}} = \mathbf{C}\left(\dot{\boldsymbol{\varepsilon}} - \dot{\boldsymbol{\varepsilon}}^{vp}\right) \ . \tag{3.45}$$

Inserting the evolution equation (Equation (3.42)) into the rate form of the constitutive law (Equation (3.45)) results in

$$\dot{\boldsymbol{\sigma}} = \mathbf{C}\left(\dot{\boldsymbol{\varepsilon}} - \frac{1}{\tau}\mathbf{C}^{-1}(\boldsymbol{\sigma} - \boldsymbol{\sigma}_{\infty})\right). \tag{3.46}$$

According to [80], the application of an implicit backward Euler algorithm yields a first-order accurate formula for the stresses at the end of the time-step as

$$\Delta\boldsymbol{\sigma}_{n+1} = \mathbf{C}\left(\Delta\boldsymbol{\varepsilon}_{n+1} - \frac{\Delta t_{n+1}}{\tau}\mathbf{C}^{-1}\left(\boldsymbol{\sigma}_{n+1} - \boldsymbol{\sigma}_{\infty,n+1}\right)\right) \ . \tag{3.47}$$

Using the relations $\Delta\boldsymbol{\sigma}_{n+1} = \boldsymbol{\sigma}_{n+1} - \boldsymbol{\sigma}_n$, $\boldsymbol{\sigma}_n + \mathbf{C}\Delta\boldsymbol{\varepsilon}_{n+1} = \boldsymbol{\sigma}_{n+1}^{trial}$, and rearranging Equation (3.47) finally yields

$$\boldsymbol{\sigma}_{n+1} = \frac{\boldsymbol{\sigma}_{n+1}^{trial} - \dfrac{\Delta t_{n+1}}{\tau}\boldsymbol{\sigma}_{\infty,n+1}}{1 + \dfrac{\Delta t_{n+1}}{\tau}} \ . \tag{3.48}$$

The stress-like internal variables are obtained by analogy. Postulating the rate-form of the hardening law as $\dot{\mathbf{q}} = -\mathbf{D}\dot{\boldsymbol{\alpha}}$, the evolution of the stress-like internal variables is obtained as

$$\dot{\mathbf{q}} = -\frac{1}{\tau}(\mathbf{q} - \mathbf{q}_{\infty}) \ . \tag{3.49}$$

Again, numerical integration with the backward Euler scheme produces an expression corresponding to Equation (3.48)

$$\mathbf{q}_{n+1} = \frac{\mathbf{q}_{n+1}^{trial} - \dfrac{\Delta t_{n+1}}{\tau}\mathbf{q}_{\infty,n+1}}{1 + \dfrac{\Delta t_{n+1}}{\tau}} \ . \tag{3.50}$$

Hence, the rate-dependent solution is simply obtained by an interpolation between the trial solution and the inviscid solution.

3.2.5.2   Time integration in nonlinear elasticity for the Perzyna model

As opposed to the previous Section, a Perzyna formulation is adopted for the case of nonlinear elasticity and single-surface plasticity, as the Perzyna formulation yields in this case a numerical time integration scheme very similar to the rate-independent time integration scheme, as will be shown later on.

However, for the general case of multidimensional states of stress, the evolution equations for viscoplastic strains and hardening can be postulated for the Perzyna model [80] as

$$\dot{\boldsymbol{\varepsilon}}^{vp} = \gamma\, \mathbf{r}(\boldsymbol{\sigma}, q) \tag{3.51}$$

$$\dot{\alpha} = \gamma\, h(\boldsymbol{\sigma}, q)\,, \tag{3.52}$$

with

$$\gamma = \frac{1}{\eta}\, \langle f\,(\boldsymbol{\sigma}, q)\rangle\,, \tag{3.53}$$

where η [Pa·s] denotes a constant viscosity parameter. As already applied for the computation of the rate-independent solution (see Section 3.2.2), an implicit integration scheme, namely, the backward Euler scheme, is used for the integration of the evolution equations, yielding

$$\Delta\boldsymbol{\varepsilon}^{vp}_{n+1} = \Delta\gamma_{n+1}\, \mathbf{r}(\boldsymbol{\sigma}_{n+1}, q_{n+1})\,, \tag{3.54}$$

$$\Delta\alpha_{n+1} = \Delta\gamma_{n+1}\, h(\boldsymbol{\sigma}_{n+1}, q_{n+1})\,, \tag{3.55}$$

with

$$\Delta\gamma_{n+1} = \frac{\Delta t_{n+1}}{\eta}\, \langle f\,(\boldsymbol{\sigma}_{n+1}, q_{n+1})\rangle\,. \tag{3.56}$$

These equations form a set of nonlinear equations for the unknowns $\boldsymbol{\varepsilon}^{vp}_{n+1}$, α_{n+1}, and $\Delta\gamma_{n+1}$. Hence, the elasto-viscoplastic constitutive equations are reformulated by introducing a trial elastic state, which is obtained by freezing viscoplastic flow during the time step Δt_{n+1}:

$$\boldsymbol{\varepsilon}^{e,trial}_{n+1} := \boldsymbol{\varepsilon}_{n+1} - \boldsymbol{\varepsilon}^{vp}_n \tag{3.57}$$

$$\boldsymbol{\sigma}^{trial}_{n+1} := \boldsymbol{\sigma}\left(\boldsymbol{\varepsilon}^{e,trial}_{n+1}\right) \tag{3.58}$$

$$\alpha^{trial}_{n+1} := \alpha_n \tag{3.59}$$

$$f^{trial}_{n+1} := f\left(\boldsymbol{\sigma}^{trial}_{n+1}, q^{trial}_{n+1}\right) \tag{3.60}$$

Whether viscoplastic loading or elastic unloading occurs in the time increment Δt_{n+1} is decided from the value of the yield function based on the trial state (see Equation (3.60)):

$$f^{trial}_{n+1} < 0 \Rightarrow \text{elastic step} \Leftrightarrow \Delta\gamma_{n+1} = 0\,, \tag{3.61}$$

$$f^{trial}_{n+1} \geq 0 \Rightarrow \text{viscoplastic step} \Leftrightarrow \Delta\gamma_{n+1} > 0\,. \tag{3.62}$$

Equation (3.61) states that for the elastic step the assumption of frozen viscoplastic flow holds, and consequently the set of state variables is given as $\{\boldsymbol{\varepsilon}^{vp}_{n+1}, \alpha_{n+1}\} = \{\boldsymbol{\varepsilon}^{vp}_n, \alpha_n\}$. For

the viscoplastic step, the state variables have to be evaluated. Therefore, a general residual formulation for the state variables and for the consistency parameter is applied, reading

$$
\mathbf{R}(\mathbf{x}) = \left\{ \begin{array}{c} R^{\boldsymbol{\varepsilon}^{vp}} \\ \hline R^{\alpha} \\ \hline R^{\Delta\gamma} \end{array} \right\} = \left\{ \begin{array}{c} -\boldsymbol{\varepsilon}_{n+1}^{vp} + \boldsymbol{\varepsilon}_n^{vp} + \Delta\gamma_{n+1}\,\mathbf{r}_{n+1} \\ \hline -\alpha_{n+1} + \alpha_n + \Delta\gamma_{n+1}\,h_{n+1} \\ \hline -\Delta\gamma_{n+1} + \dfrac{\Delta t_{n+1}}{\eta}\,f_{n+1} \end{array} \right\} = \mathbf{0}\ .
\tag{3.63}
$$

As in Section 3.2.2, a Newton scheme $\mathbf{R} + (d\mathbf{R}/d\mathbf{x})\Delta\mathbf{x} = \mathbf{0}$ with $\mathbf{x} = (\boldsymbol{\varepsilon}_{n+1}^{vp}, \alpha_{n+1} | \Delta\gamma_{n+1})^T$ is applied for the solution of Equation (3.63). Accordingly, the Newton scheme yields

$$
\mathbf{R} + \left[\begin{array}{cc|c} \mathbf{A}^{-1} & & \nabla g \\ \hline \dfrac{\Delta t_{n+1}}{\eta}\nabla f^T & & -1 \end{array} \right] \left[\begin{array}{cc|c} -\mathbf{C} & 0 & 0 \\ 0^T & -D & 0 \\ \hline 0^T & 0 & 1 \end{array} \right] \left\{ \begin{array}{c} \Delta\boldsymbol{\varepsilon}_{n+1}^p \\ \Delta\alpha_{n+1} \\ \hline \Delta\left(\Delta\gamma_{n+1}\right) \end{array} \right\} = \mathbf{0}\ .
\tag{3.64}
$$

The updated viscoplastic strains, the hardening variables, and the consistency parameter during the Newton iteration are computed from

$$
\boldsymbol{\varepsilon}_{n+1}^{vp} = \boldsymbol{\varepsilon}_n^{vp} + \Delta\boldsymbol{\varepsilon}_{n+1}^{vp}
\tag{3.65}
$$

$$
\alpha_{n+1} = \alpha_n + \Delta\alpha_{n+1}
\tag{3.66}
$$

$$
\Delta\gamma_{n+1} = \Delta\gamma_n + \Delta\left(\Delta\gamma_{n+1}\right)\ .
\tag{3.67}
$$

A comparison of the Perzyna approach with the rate-independent solution shows that the residual formulations are rather similar. Hence, the application of the Perzyna type of viscoplastic formulation is straightforward for the case of single-surface plasticity.

3.2.6 Consistent linearization. Elasto-viscoplastic moduli

3.2.6.1 Elasto-viscoplastic moduli for Duvaut-Lions model

For linear elasticity and application of the Duvaut-Lions model, the elasto-viscoplastic tangent modulus $\mathbf{C}_{T,n+1}$ is obtained by derivation of the stresses with respect to the total strains at the end of the time increment and reads as

$$
\mathbf{C}_{T,n+1} = \frac{\mathbf{C}_{n+1} - \dfrac{\Delta t_{n+1}}{\tau}\mathbf{C}_{\infty,n+1}}{1 + \dfrac{\Delta t_{n+1}}{\tau}}\ ,
\tag{3.68}
$$

where $\mathbf{C}_{\infty}$ is the rate-independent elastoplastic tangent modulus.

3.2.6.2 Elasto-viscoplastic moduli for Perzyna model

For nonlinear elasticity and application of the Perzyna model, the discrete residuum (see Equation (3.63)) yields $\mathbf{R(x)} = \mathbf{0}$. Linearization of the time integration scheme, i.e. using the condition $d\mathbf{R}(\varepsilon_{n+1}^{vp}, \alpha_{n+1}|\Delta\gamma_{n+1}) = \mathbf{0}$ yields

$$\left[\begin{array}{c|c} \mathbf{A}^{-1} & \boldsymbol{\nabla} g \\ \hline \dfrac{\Delta t_{n+1}}{\eta}\boldsymbol{\nabla} f^T & -1 \end{array} \right] \left\{ \begin{array}{c} d\boldsymbol{\sigma}_{n+1} \\ dq_{n+1} \\ \hline d\left(\Delta\gamma_{n+1}\right) \end{array} \right\} - \left\{ \begin{array}{c} d\varepsilon_{n+1} \\ 0 \\ 0 \end{array} \right\} = \mathbf{0} \ . \tag{3.69}$$

Again, the differential form of the constitutive law $-d\varepsilon_{n+1}^p = \mathbf{C}_{n+1}^{-1} d\boldsymbol{\sigma}_{n+1} - d\varepsilon_{n+1}$ and of the hardening law $-d\alpha_{n+1} = D_{n+1}^{-1} dq_{n+1}$ are applied. Note that $d\varepsilon_{n+1} \neq 0$.

Solving Equation (3.69) for $\{d\boldsymbol{\sigma}_{n+1}, dq_{n+1}\}^T$ finally gives the relation for the elasto-viscoplastic tangent modulus, which can be extracted from the relation

$$\left\{ \begin{array}{c} d\boldsymbol{\sigma}_{n+1} \\ dq_{n+1} \end{array} \right\} = \left[\mathbf{A} - \tilde{g}^{inv}\mathbf{A}\boldsymbol{\nabla} g\boldsymbol{\nabla} f^T \mathbf{A} \right] \left\{ \begin{array}{c} d\varepsilon_{n+1} \\ 0 \end{array} \right\} \ , \tag{3.70}$$

where

$$\tilde{g} = \frac{\eta}{\Delta t_{n+1}} + \boldsymbol{\nabla} f^T \mathbf{A}\boldsymbol{\nabla} g \ . \tag{3.71}$$

3.3 Material models for granular soil

As described in Section 3.1, shearing of a granular mass such as sand does not exclusively result in particle movement in the direction of shear. At low to moderate confining pressures, particles push adjacent grains out of their way or move up and over them. Such pushing or climbing is termed interlocking. It generates an increase of the shear resistance of the material and, hence, an increase of the angle of internal friction φ. Figure 3.4 shows this increase by means of an illustrative load-displacement curve of a simple shear test. After the peak load level has been reached, the load-carrying capacity decreases with increasing deformation. This behavior is associated with the formation of zones of limited thickness where irreversible strains localize. Strain localization causes a change in the local structure of the material. The material is losing its shear resistance (see dashed line in Figure 3.4). Finally, when the shear band is fully developed, a residual amount of shear resistance remains. It is characterized by a constant angle of internal friction φ.

This behavior of granular soil can be formulated adequately in the framework of the following two plasticity models of Drucker-Prager type and Mohr-Coulomb type, respectively. The Mohr-Coulomb model, presented in this work, is based on the well-known Mohr-Coulomb failure criterion, which is commonly used in classical soil mechanics. Consequently, a Mohr-Coulomb model is best suited for application to numerical simulations
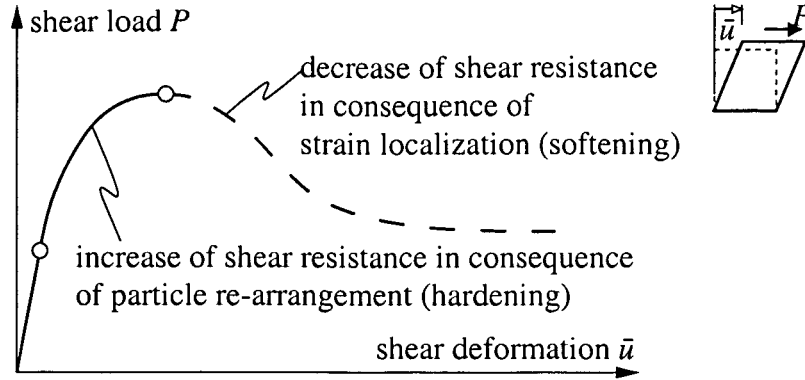
Figure 3.4: On the evolution of the shear resistance (friction angle φ) under shear loading

in soil mechanics. However, the corner regions of the of the hexagonal shape of the loading surface cause a significant reduction of numerical robustness. Therefore, an additional model, the Drucker-Prager model, will also be presented, as its cone-shaped loading surface can be calibratd corresponding to a defined meridonal section of the Mohr-Coulomb criterion. Additionally, the cone-shaped loading surface is smooth and, thus, provides great numerical robustness. Both models are formulated in a similar manner to enable a comparison. After the numerical derivation of the two models, both of them will be verified using laboratory tests.

3.3.1 Drucker-Prager and Mohr-Coulomb plasticity models

3.3.1.1 Yield surfaces

In this work, the change of the friction angle φ is considered in the framework of the Drucker-Prager and the Mohr-Coulomb yield criterion, respectively. The first one is well suited for the description of the inelastic behavior of granular materials under moderate compressive loading states. The second one is the classical one for the description of strength characteristics of granular materials like sand or rock under moderate compressive loading states.

The loading functions for both criteria are given by (see [94] for a similar approach for the Drucker-Prager criterion, and [87, 94] for the Mohr-Coulomb criterion):

$$f_{DP}(\boldsymbol{\sigma}, q_{DP}) = \sqrt{J_2} + \kappa_{DP}(I_1 - k_{DP}) , \tag{3.72}$$

$$f_{MC}(\boldsymbol{\sigma}, q_{MC}) = \frac{1}{2}(\sigma_1 - \sigma_3) + \kappa_{MC}\left(\frac{1}{2}(\sigma_1 + \sigma_3) - k_{MC}\right) , \tag{3.73}$$

where κ_{DP}, κ_{MC} and k_{DP}, k_{MC} are material parameters. κ_{DP} and k_{DP} are derived from the tensile and compressive meridian, respectively of the loading surface according to the

Mohr-Coulomb criterion as (see, e. g.[72])

$$\kappa_{DP} = \frac{2\sin\varphi}{\sqrt{3}(3 \pm \sin\varphi)} \quad \text{and} \quad k_{DP} = \frac{3c}{\tan\varphi} , \tag{3.74}$$

and κ_{MC} and k_{MC} are given as

$$\kappa_{MC} = \sin\varphi \quad \text{and} \quad k_{MC} = \frac{c}{\tan\varphi} . \tag{3.75}$$

In both equations, c and φ denote the cohesion and the friction angle, respectively. For the description of the material response under tensile loading, the tension-cut-off criterion is employed. It is characterized by the following loading function:

$$f_{TC}(\boldsymbol{\sigma}) = I_1 - f_{tu} . \tag{3.76}$$

f_{tu} represents the uniaxial tensile strength of the material. In general, the tensile strength of granular soil is negligible.

3.3.1.2 Plastic flow rule

Dense (as opposed to loose) granular soil exhibits volume dilation when subjected to shear deformations. In the context of the described Drucker-Prager and Mohr-Coulomb models, the use of an associative flow rule would result in an overestimation of this dilation [98]. Consequently, a nonassociative flow rule is adopted, characterized by the plastic potentials g_{DP} and g_{MC}. For the tension-cut-off criterion, an associative flow rule, i.e., $g_{TC} = f_{TC}$, is used. The respective evolution equations for the plastic strain tensor are given by

$$\dot{\boldsymbol{\varepsilon}}^p = \gamma_{DP}\, \partial_{\boldsymbol{\sigma}} g_{DP} + \gamma_{TC}\, \partial_{\boldsymbol{\sigma}} f_{TC} \quad \text{for the Drucker-Prager model,} \tag{3.77}$$

$$\dot{\boldsymbol{\varepsilon}}^p = \gamma_{MC}\, \partial_{\boldsymbol{\sigma}} g_{MC} + \gamma_{TC}\, \partial_{\boldsymbol{\sigma}} f_{TC} \quad \text{for the Mohr-Coulomb model,} \tag{3.78}$$

where γ_{DP}, γ_{MC} and γ_{TC} are the consistency parameters. The plastic potentials employed for the Drucker-Prager criterion, g_{DP}, and for the Mohr-Coulomb criterion, g_{MC}, are characterized by a modification of the yield function f with respect to its volumetric part, reading

$$g_{DP} = \sqrt{J_2} + \bar{\kappa}_{DP} I_1 , \tag{3.79}$$

$$g_{MC} = \frac{1}{2}(\sigma_1 - \sigma_3) + \bar{\kappa}_{MC}\left(\frac{1}{2}(\sigma_1 + \sigma_3)\right) , \tag{3.80}$$

where $\bar{\kappa}_{DP}$ and $\bar{\kappa}_{MC}$ are material parameters. They are related to the angle of dilatancy ψ in the same way as κ to φ in Equations $(3.74)_1$ and $(3.75)_1$ (see [8]):

$$\bar{\kappa}_{DP} = \frac{2\sin\psi}{\sqrt{3}(3 \pm \sin\psi)} , \tag{3.81}$$

$$\bar{\kappa}_{MC} = \sin\psi . \tag{3.82}$$

Generally, the angle of dilatancy ψ is smaller than the friction angle φ.
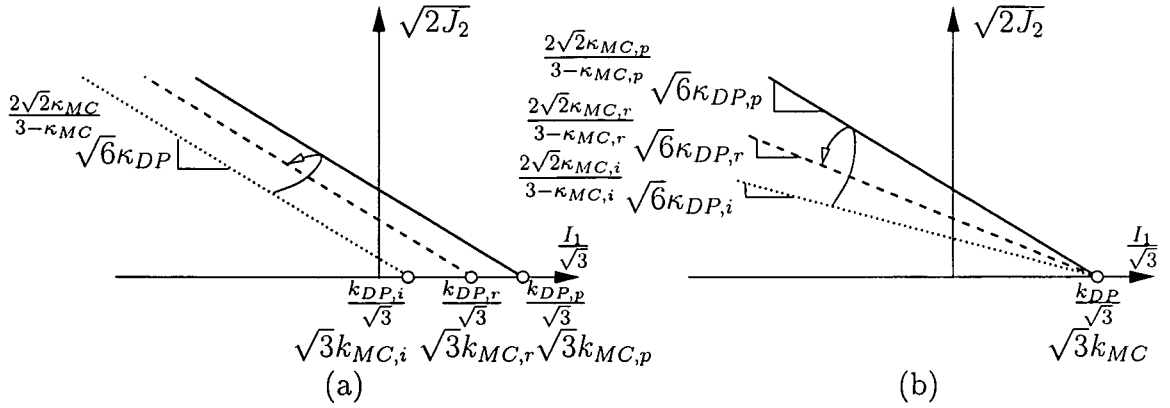
Figure 3.5: Illustration of hardening/softening for the Drucker-Prager and Mohr-Coulomb criterion, respectively: (a) cohesion and (b) friction hardening (κ, k: material parameters; subindices i, p, and r refer to the initial, peak, and residual value)

3.3.1.3 Hardening/softening rule

As regards the Drucker-Prager and the Mohr-Coulomb criterion, respectively, two basic modes of isotropic hardening can be distinguished [94]: cohesion and friction hardening (see Figure 3.5). Consideration of a changing friction angle φ results in a combination of both modes of hardening (see Equations (3.74) and (3.75)). By a first approximation, k_{DP} and k_{MC} are assumed to be constant, with

$$k_{DP} = \frac{3c}{\tan\varphi_p} , \tag{3.83}$$

$$k_{MC} = \frac{c}{\tan\varphi_p} , \tag{3.84}$$

where φ_p denotes the peak value of the friction angle φ. This results in pure friction hardening, characterized by a change of κ_{DP} and κ_{MC} only [58]. This assumption of friction hardening is valid for soils with no or small cohesion, like gravel or uncemented sands. The initial, peak, and residual values of κ_{DP} and κ_{MC} are obtained from the respective friction angle as

$$\kappa_{DP,i} = \frac{2\sin\varphi_i}{\sqrt{3}(3 \pm \sin\varphi_i)} , \quad \kappa_{DP,p} = \frac{2\sin\varphi_p}{\sqrt{3}(3 \pm \sin\varphi_p)} , \quad \kappa_{DP,r} = \frac{2\sin\varphi_r}{\sqrt{3}(3 \pm \sin\varphi_r)} , \tag{3.85}$$

$$\kappa_{MC,i} = \sin\varphi_i , \quad \kappa_{MC,p} = \sin\varphi_p , \quad \kappa_{MC,r} = \sin\varphi_r . \tag{3.86}$$

Based on these values, square-root hardening and exponential softening behavior is assumed (see Figure 3.6). As the following formulae apply identically to both models, the
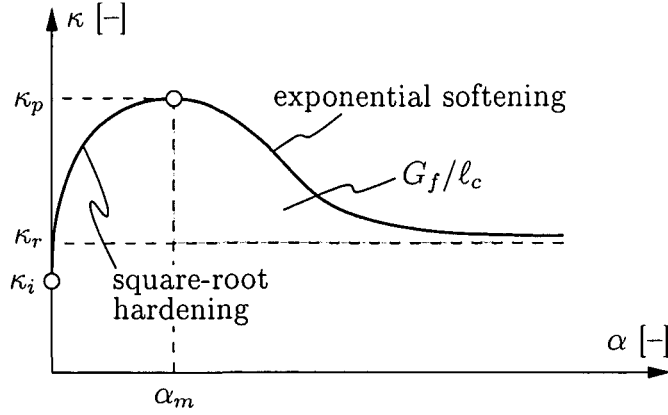
Figure 3.6: Hardening/softening law adopted for the Drucker-Prager and the Mohr-Coulomb criterion, respectively (G_f: softening material parameter; ℓ_c: *characteristic length*) (The indices DP nad MC are omitted here for simplicity)

indices DP and MC will be omitted for the sake of simplicity. The applied hardening/softening formulae read

$$
\kappa = \begin{cases} \kappa_i + (\kappa_p - \kappa_i)\sqrt{\dfrac{\alpha(2\alpha_m - \alpha)}{\alpha_m^2}} & \text{for } \alpha \leq \alpha_m \ , \\[4mm] (\kappa_p - \kappa_r)\exp\left[-\left(\dfrac{\alpha - \alpha_m}{\alpha_u}\right)^2\right] + \kappa_r & \text{for } \alpha \geq \alpha_m \ , \end{cases} \tag{3.87}
$$

where α_u is a calibration parameter. It follows from setting the area under the softening branch (see Figure 3.6),

$$
\int\limits_{\alpha_m}^{\infty} (\kappa - \kappa_r)\, d\alpha \ , \tag{3.88}
$$

equal to the softening material parameter divided by the *characteristic length*, G_f/ℓ_c. Inserting κ according to Equation (3.87) into Equation (3.88) yields α_u as

$$
\alpha_u = \frac{2}{\kappa_p - \kappa_r}\frac{G_f}{\ell_c\sqrt{\pi}} \ . \tag{3.89}
$$

The evolution of κ is controlled by means of the strain-like internal variable α. Since friction hardening/softening is connected with deviatoric deformations, α is related to the deviatoric part of the plastic strain tensor, $\mathbf{e}^p$. The following form is chosen for this relationship (see [72, 85, 94] for similar definitions):

$$
\dot{\alpha} = \sqrt{\frac{2}{3}\, \dot{\mathbf{e}}^{p,T}\dot{\mathbf{e}}^{p}} \ . \tag{3.90}
$$
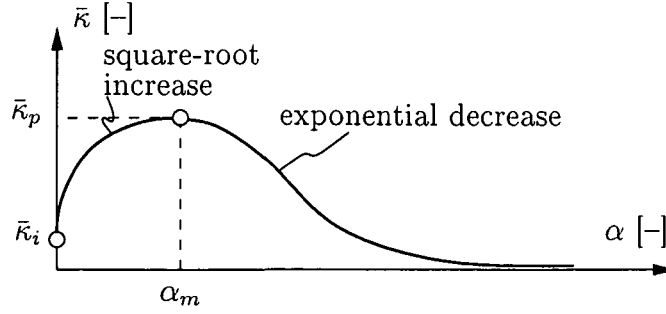
Figure 3.7: Consideration of varying angle of dilatancy by a variable value of $\bar{\kappa}$ in the plastic potential g (The indices DP and MC are omitted here for simplicity)

Consideration of

$$\dot{\mathbf{e}}^p = \gamma \partial_s g \ , \tag{3.91}$$

where $\mathbf{s}$ denotes the deviatoric stress tensor, in Equation (3.90) finally gives, for both models,

$$\dot{\alpha} = \gamma \sqrt{\frac{2}{3} \left(\partial_s g \right)^T \left(\partial_s g \right)} \ . \tag{3.92}$$

The tension-cut-off criterion is based on the assumption of ideally-plastic behavior. The strain-like internal variable α_{TC} is related to the volumetric part of the plastic strain tensor. The evolution equation for α_{TC} becomes

$$\dot{\alpha}_{TC} = \gamma_{TC} \ . \tag{3.93}$$

3.3.1.4 Angle of dilatancy ψ

The changing dilatancy of granular soils during shear loading is accounted for by a variable angle of dilatancy ψ (see [94]). Under medium compressive loading, the angle of dilatancy ψ is assumed to increase during shear deformation from an initial value ψ_i to a peak value ψ_p. Continuation of shear loading results in the decrease of ψ to zero. ψ is employed for the determination of $\bar{\kappa}$ (see Equation (3.81)). The evolution of $\bar{\kappa}$ is controlled by α [91], see Figure 3.7. The initial value and the peak value, respectively, of $\bar{\kappa}$, related to the corresponding dilatancy angle, are given by

$$\bar{\kappa}_{DP,i} = \frac{2 \sin \psi_i}{\sqrt{3}(3 \pm \sin \psi_i)} \quad \text{and} \quad \bar{\kappa}_{DP,p} = \frac{2 \sin \psi_p}{\sqrt{3}(3 \pm \sin \psi_p)} \ , \tag{3.94}$$

$$\bar{\kappa}_{MC,i} = \sin \psi_i \quad \text{and} \quad \bar{\kappa}_{MC,p} = \sin \psi_p \ , \tag{3.95}$$

respectively. The evolution of the slope $\bar{\kappa}$ of the plastic potential (see Equations (3.79) and (3.80)) is assumed to be similar to the evolution of κ given in Figure 3.6. Hence, the peak

values κ_p and $\bar{\kappa}_p$ occur at the same value α_m (see also [91]). The evolution of $\bar{\kappa}$ reads

$$\bar{\kappa} = \begin{cases} \bar{\kappa}_i + (\bar{\kappa}_p - \bar{\kappa}_i)\sqrt{\dfrac{\alpha(2\alpha_m - \alpha)}{\alpha_m^2}} & \text{for } \alpha \le \alpha_m \ , \\[2ex] \bar{\kappa}_p \exp\left[-\left(\dfrac{\alpha - \alpha_m}{\alpha_u}\right)^2 \right] & \text{for } \alpha \ge \alpha_m \ . \end{cases} \tag{3.96}$$

3.3.1.5 Time integration of the evolution equations for the Drucker-Prager model

As outlined in Section 3.2.2, for the time integration of the evolution equations the Return Map Algorithm is applied [79]. Assuming two active yield surfaces, the implicit integration scheme yields (see Equations (3.11) and (3.12))

$$\varepsilon_{n+1}^p = \varepsilon_n^p + \Delta\varepsilon_{n+1}^p \tag{3.97}$$

$$\alpha_{DP,n+1} = \alpha_{DP,n} + \Delta\alpha_{DP,n+1} \tag{3.98}$$

$$\alpha_{TC,n+1} = \alpha_{TC,n} + \Delta\alpha_{TC,n+1} \tag{3.99}$$

Rewriting Equations from (3.97) to (3.99) in residual form gives

$$\mathbf{R}(\varepsilon_{n+1}^p, \alpha_{DP,n+1}, \alpha_{TC,n+1} | \Delta\gamma_{DP,n+1}, \Delta\gamma_{TC,n+1}) = \left\{ \begin{array}{c} \mathbf{R}^{\varepsilon^p} \\ R^{\alpha_{DP}} \\ R^{\alpha_{TC}} \\ \hline R^{f_{DP}} \\ R^{f_{TC}} \end{array} \right\} =$$

$$\left\{ \begin{array}{c} -\varepsilon_{n+1}^p + \varepsilon_n^p + \Delta\gamma_{DP,n+1}\partial_{\boldsymbol{\sigma}}g_{DP,n+1} + \Delta\gamma_{TC,n+1}\partial_{\boldsymbol{\sigma}}g_{TC,n+1} \\ -\alpha_{DP,n+1} + \alpha_{DP,n} + \Delta\gamma_{DP,n+1}\sqrt{\tfrac{2}{3}(\partial_s g_{DP,n+1})^T \partial_s g_{DP,n+1}} \\ -\alpha_{TC,n+1} + \alpha_{TC,n} + \Delta\gamma_{TC,n+1} \\ \hline f_{DP,n+1} \\ f_{TC,n+1} \end{array} \right\} = \mathbf{0} \ . \tag{3.100}$$

The matrices ∇f_{DP}, ∇f_{TC}, ∇g_{DP}, ∇g_{TC}, and $\mathbf{A}^{-1}$, required for the solution of the Newton scheme, are given as

$$\nabla f_{DP} = \left\{ \begin{array}{c} \partial_{\boldsymbol{\sigma}}f_{DP} \\ \partial_{q_{DP}}f_{DP} \\ \partial_{q_{TC}}f_{DP} \end{array} \right\} \quad \text{and} \quad \nabla f_{TC} = \left\{ \begin{array}{c} \partial_{\boldsymbol{\sigma}}f_{TC} \\ \partial_{q_{DP}}f_{TC} \\ \partial_{q_{TC}}f_{TC} \end{array} \right\} \tag{3.101}$$

$$\nabla g_{DP} = \left\{ \begin{array}{c} \partial_{\boldsymbol{\sigma}}g_{DP} \\ \sqrt{\tfrac{2}{3}(\partial_s g_{DP})^T(\partial_s g_{DP})} \\ 0 \end{array} \right\} \quad \text{and} \quad \nabla g_{TC} = \nabla f_{TC} \tag{3.102}$$

$$
\mathbf{A}^{-1} = \begin{bmatrix} \mathbf{C}^{-1} & \mathbf{0} & \mathbf{0} \\ \mathbf{0}^T & D_{DP}^{-1} & 0 \\ \mathbf{0}^T & 0 & D_{TC}^{-1} \end{bmatrix} + \left[\begin{array}{cc} \Delta\gamma_{DP}\partial_{\boldsymbol{\sigma}\boldsymbol{\sigma}}^2 g_{DP} + \Delta\gamma_{TC}\partial_{\boldsymbol{\sigma}\boldsymbol{\sigma}}^2 g_{TC} \\ \Delta\gamma_{DP}\dfrac{2}{3}\dfrac{(\partial_s g_{DP})^T \partial_{\boldsymbol{\sigma}\boldsymbol{\sigma}}^2 g_{DP}}{\sqrt{\frac{2}{3}(\partial_s g_{DP})^T(\partial_s g_{DP})}} \\ \Delta\gamma_{TC}\partial_{q_{TC}\boldsymbol{\sigma}}^2 g_{TC} \end{array} \right.
$$

$$
\left. \begin{array}{cc} \Delta\gamma_{DP}\partial_{\boldsymbol{\sigma} q_{DP}}^2 g_{DP} + \Delta\gamma_{TC}\partial_{\boldsymbol{\sigma} q_{DP}}^2 g_{TC} & \Delta\gamma_{DP}\partial_{\boldsymbol{\sigma} q_{TC}}^2 g_{DP} + \Delta\gamma_{TC}\partial_{\boldsymbol{\sigma} q_{TC}}^2 g_{TC} \\ \Delta\gamma_{DP}\dfrac{2}{3}\dfrac{(\partial_s g_{DP})^T \partial_{\boldsymbol{\sigma} q_{DP}}^2 g_{DP}}{\sqrt{\frac{2}{3}(\partial_s g_{DP})^T(\partial_s g_{DP})}} & \Delta\gamma_{DP}\dfrac{2}{3}\dfrac{(\partial_s g_{DP})^T \partial_{\boldsymbol{\sigma} q_{TC}}^2 g_{DP}}{\sqrt{\frac{2}{3}(\partial_s g_{DP})^T(\partial_s g_{DP})}} \\ \Delta\gamma_{TC}\partial_{q_{TC} q_{DP}}^2 g_{TC} & \Delta\gamma_{TC}\partial_{q_{TC} q_{TC}}^2 g_{TC} \end{array} \right] \tag{3.103}
$$

3.3.1.6 Consistent elastoplastic tangent modulus

The elastoplastic tangent modulus can be extracted from the relation (see Equation (3.29))

$$
\left\{ \begin{array}{c} d\boldsymbol{\sigma}_{n+1} \\ dq_{DP,n+1} \\ dq_{TC,n+1} \end{array} \right\} = [\mathbf{A} \quad - \quad g_{11}^{inv}\mathbf{A}\nabla g_{DP}\nabla f_{DP}^T\mathbf{A} - g_{12}^{inv}\mathbf{A}\nabla g_{DP}\nabla f_{TC}^T\mathbf{A} \tag{3.104}
$$

$$
- \quad g_{21}^{inv}\mathbf{A}\nabla g_{TC}\nabla f_{DP}^T\mathbf{A} - g_{22}^{inv}\mathbf{A}\nabla g_{TC}\nabla f_{TC}^T\mathbf{A}] \left\{ \begin{array}{c} d\boldsymbol{\varepsilon}_{n+1} \\ 0 \\ 0 \end{array} \right\},
$$

with

$$
\mathbf{g}^{inv} = \begin{bmatrix} g_{11}^{inv} & g_{12}^{inv} \\ g_{21}^{inv} & g_{22}^{inv} \end{bmatrix} \quad \text{and} \quad \mathbf{g} = \begin{bmatrix} \nabla f_{DP}^T\mathbf{A}\nabla g_{DP} & \nabla f_{DP}^T\mathbf{A}\nabla g_{TC} \\ \nabla f_{TC}^T\mathbf{A}\nabla g_{DP} & \nabla f_{TC}^T\mathbf{A}\nabla g_{TC} \end{bmatrix}. \tag{3.105}
$$

3.3.1.7 Extension to account for viscoplastic behavior

For the Drucker-Prager material model and the linear elastic law, the Duvaut-Lions viscoplastic formulation is applied. Hence, the stresses and the hardening variables are computed acc. to the Equations (3.48) and (3.50) as

$$
\boldsymbol{\sigma}_{n+1} = \frac{\boldsymbol{\sigma}_{n+1}^{trial} - \dfrac{\Delta t_{n+1}}{\tau}\boldsymbol{\sigma}_{\infty,n+1}}{1 + \dfrac{\Delta t_{n+1}}{\tau}} \tag{3.106}
$$

$$
\mathbf{q}_{n+1} = \frac{\mathbf{q}_{n+1}^{trial} - \dfrac{\Delta t_{n+1}}{\tau}\mathbf{q}_{\infty,n+1}}{1 + \dfrac{\Delta t_{n+1}}{\tau}}. \tag{3.107}
$$

The viscoplastic strains and the internal variables after time integration are obtained by means of the linear elastic law and the hardening rule (see Equation (3.87)) as

$$\varepsilon^{vp}_{n+1} = \varepsilon_{n+1} - \mathbf{C}^{-1}\sigma_{n+1} \tag{3.108}$$

$$\alpha_{DP,n+1} = \alpha_{DP,n+1}(q_{DP,n+1}) . \tag{3.109}$$

The elasto-viscoplastic tangent is also obtained by interpolation and reads

$$\mathbf{C}_{T,n+1} = \frac{\mathbf{C}_{n+1} - \dfrac{\Delta t_{n+1}}{\tau}\mathbf{C}_{\infty,n+1}}{1 + \dfrac{\Delta t_{n+1}}{\tau}} . \tag{3.110}$$

3.3.1.8 Time integration of the evolution equations for the Mohr-Coulomb model

As outlined in Section 3.2.2, for the time integration of the evolution equations the Return Map Algorithm is applied [79]. Assuming two active yield surfaces in one of the corners of the Mohr-Coulomb irregular hexagonal yield surface, the implicit integration scheme yields (see Equations (3.11) and (3.12))

$$\varepsilon^{p}_{n+1} = \varepsilon^{p}_{n} + \Delta\varepsilon^{p}_{n+1} \tag{3.111}$$

$$\alpha_{MC,n+1} = \alpha_{MC,n} + \Delta\alpha_{MC,n+1} \tag{3.112}$$

Note that for the projection onto the corner of the Mohr-Coulomb yield surface, a fictitious yield surface $f_{MCf} = \sigma_i - \sigma_j$ is introduced, where $i,j = 1,2,3$. Together with associative evolution of plastic flow $\dot{\varepsilon}^{p} = \gamma_{MCf}\partial_{\sigma}f_{MCf}$ and ideal plastic behavior $\dot{\alpha}_{MCf} = 0$, the residual is obtained as

$$\mathbf{R}(\varepsilon^{p}_{n+1}, \alpha_{MC,n+1}|\Delta\gamma_{MC,n+1}, \Delta\gamma_{MCf,n+1}) = \left\{ \begin{array}{c} \mathbf{R}^{\varepsilon^p} \\ R^{\alpha_{MC}} \\ \hline R^{f_{MC}} \\ R^{f_{MCf}} \end{array} \right\} =$$

$$\left\{ \begin{array}{c} -\varepsilon^{p}_{n+1} + \varepsilon^{p}_{n} + \Delta\gamma_{MC,n+1}\partial_{\sigma}g_{MC,n+1} + \Delta\gamma_{MCf,n+1}\partial_{\sigma}f_{MCf,n+1} \\ -\alpha_{MC,n+1} + \alpha_{MC,n} + \Delta\gamma_{MC,n+1}\sqrt{\frac{2}{3}(\partial_{s}g_{MC,n+1})^{T}\partial_{s}g_{MC,n+1}} \\ \hline f_{MC,n+1} \\ f_{MCf,n+1} \end{array} \right\} = 0 . \tag{3.113}$$

The matrices required for the solution of the Newton scheme (see Equations from (3.21) to (3.23)) follow as

$$\nabla f_{MC} = \left\{ \begin{array}{c} \partial_{\sigma}f_{MC} \\ \partial_{q_{MC}}f_{MC} \end{array} \right\} \quad \text{and} \quad \nabla f_{MCf} = \left\{ \begin{array}{c} \partial_{\sigma}f_{MCf} \\ 0 \end{array} \right\} \tag{3.114}$$

$$\nabla g_{MC} = \left\{ \frac{\partial_\sigma g_{MC}}{\sqrt{\frac{2}{3}(\partial_s g_{MC})^T(\partial_s g_{MC})}} \right\} \quad \text{and} \quad \nabla g_{MCf} = \nabla f_{MCf} \tag{3.115}$$

and $\mathbf{A}^{-1}$ reduces to

$$\mathbf{A}^{-1} = \begin{bmatrix} \mathbf{C}^{-1} & \mathbf{0} \\ \mathbf{0}^T & D_{MC}^{-1} \end{bmatrix} . \tag{3.116}$$

3.3.1.9   Consistent elastoplastic tangent modulus

Assuming two active yield surfaces in one of the corners of the Mohr-Coulomb criterion, the elastoplastic tangent modulus for the case of two active yield surfaces can be extracted from the relation

$$\left\{ \begin{array}{c} d\boldsymbol{\sigma}_{n+1} \\ dq_{MC,n+1} \end{array} \right\} = [\mathbf{A} \quad - \quad g_{11}^{inv}\mathbf{A}\nabla g_{MC}\nabla f_{MC}^T\mathbf{A} - g_{12}^{inv}\mathbf{A}\nabla g_{MC}\nabla f_{MCf}^T\mathbf{A} \tag{3.117}$$

$$- \quad g_{21}^{inv}\mathbf{A}\nabla f_{MCf}\nabla f_{MC}^T\mathbf{A} - g_{22}^{inv}\mathbf{A}\nabla f_{MCf}\nabla f_{MCf}^T\mathbf{A}] \left\{ \begin{array}{c} d\boldsymbol{\varepsilon}_{n+1} \\ 0 \\ 0 \end{array} \right\} ,$$

with

$$\mathbf{g} = \begin{bmatrix} \nabla f_{MC}^T\mathbf{A}\nabla g_{MC} & \nabla f_{MC}^T\mathbf{A}\nabla f_{MCf} \\ \nabla f_{MCf}^T\mathbf{A}\nabla g_{MC} & \nabla f_{MCf}^T\mathbf{A}\nabla f_{MCf} \end{bmatrix} . \tag{3.118}$$

3.3.1.10   Extension to account for viscoplastic behavior

For the Mohr-Coulomb material model incorporating a linear elastic law, the Duvaut-Lions viscoplastic formulation is applied. Hence, the stresses and the hardening variables are computed acc. to Equations (3.48) and (3.50) as

$$\boldsymbol{\sigma}_{n+1} = \frac{\boldsymbol{\sigma}_{n+1}^{trial} - \dfrac{\Delta t_{n+1}}{\tau}\boldsymbol{\sigma}_{\infty,n+1}}{1 + \dfrac{\Delta t_{n+1}}{\tau}} \tag{3.119}$$

$$\mathbf{q}_{n+1} = \frac{\mathbf{q}_{n+1}^{trial} - \dfrac{\Delta t_{n+1}}{\tau}\mathbf{q}_{\infty,n+1}}{1 + \dfrac{\Delta t_{n+1}}{\tau}} . \tag{3.120}$$

The viscoplastic strains and the internal variables after time integration are obtained by means of the linear elastic law and the hardening rule as

$$\boldsymbol{\varepsilon}_{n+1}^{vp} = \boldsymbol{\varepsilon}_{n+1} - \mathbf{C}^{-1}\boldsymbol{\sigma}_{n+1} \tag{3.121}$$

$$\boldsymbol{\alpha}_{n+1} = \boldsymbol{\alpha}_{n+1}(\mathbf{q}_{n+1}) . \tag{3.122}$$

The elasto-viscoplastic tangent is obtained by interpolation and reads

$$\mathbf{C}_{T,n+1} = \frac{\mathbf{C}_{n+1} - \dfrac{\Delta t_{n+1}}{\tau}\mathbf{C}_{\infty,n+1}}{1 + \dfrac{\Delta t_{n+1}}{\tau}} \; . \tag{3.123}$$

3.3.2 Verification of the Drucker-Prager model: Simple shear test

3.3.2.1 Determination of missing material parameters

A series of direct shear tests performed with an artificial frictional material in form of an assembly of aluminium bars is used for the verification of the Drucker-Prager model. These tests are reported in [85]. However, the material properties given in [85] (see Table 3.1) are not sufficient for the Drucker-Prager material model. Hence, the missing material

set of material parameters	
bulk unit weight, γ [N/mm^3]	$0.219 \cdot 10^{-3}$
Young's modulus, E [MPa]	3.387
Poisson's ratio, ν [–]	0.18
peak friction angle, φ_p [°]	30.7
residual friction angle, φ_r [°]	23.2
cohesion, c [MPa]	0
peak dilation angle, ψ_p [°]	8.7

Table 3.1: Material properties for aluminium bar assembly as given in [85]

properties as well as an improved value of φ_p are determined by means of back analysis [68] using the experimental data reported in [85]. Four different tests with different vertical pressure σ_v were performed. All of them are used in the course of back analysis.

The employed numerical model is characterized by a single plane-strain finite element[3] (see Figure 3.8(a)).

The size of the element was adapted to the shear band width of 30 mm as reported in [85]. Accordingly, $\ell_c = \sqrt{A^e} = 30$ mm. For this example, the Drucker-Prager model derived

---

[3]The choice of plane stress conditions would also have been reasonable as the direct shear test with the aluminium bars was conducted without use of a front wall, thus, $\sigma_{out-of-plane} = 0$. But as the material behavior of the aluminium bar assembly is much stiffer in the out-of-plane direction than in the in-plane direction, the plane-stress assumption together with the isotropic material model yields numerical results which understimate the experimentally observed shear load remarkably. However, an adequately stiff answer in the out-of-plane direction can be obtained using the plane-strain assumption. Consequently, this assumption is adopted, additionally justified by the consideration of a 1 mm slice in the middle of the bars. With this assumption, the experimentally observed shear load can be reproduced with the isotropic material model.
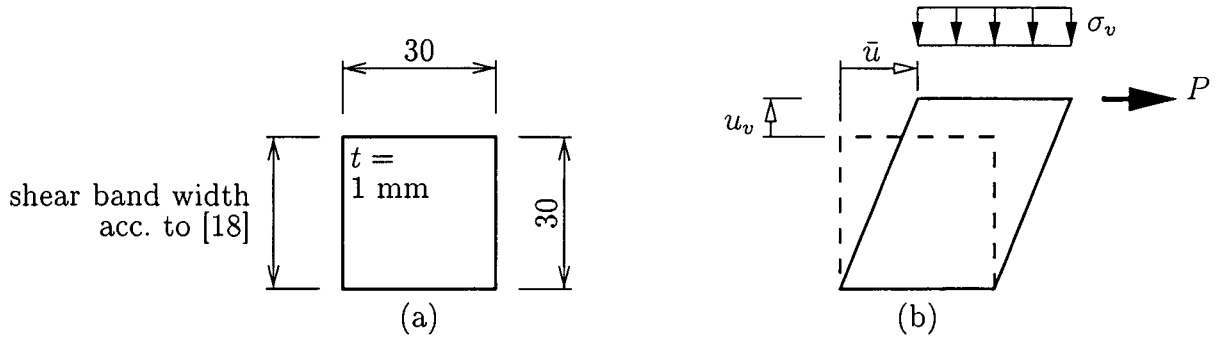
Figure 3.8: Determination of missing material parameters by means of back analysis: (a) geometric dimensions of employed model (in [mm]) and (b) applied mode of deformation ($\bar{u}$: prescribed displacement at top edge of finite element)

final set of missing material parameters	
initial friction angle, φ_i [°]	5.928
peak friction angle, φ_p [°]	32.109
softening material parameter, G_f [mm]	0.1067
internal variable α_{DP} at $\varphi = \varphi_p$, $\alpha_{DP,m}$ [–]	0.04547

Table 3.2: Determination of missing material parameters and adaptation of φ_p by means of back analysis: final set of missing and adapted material parameters [68]

from the tensile meridian of the Mohr-Coulomb model is used, as numerical simulations of plane strain direct shear tests using a Mohr-Coulomb criterion had shown that the stress point was mainly located in the region of the tensile corner.

The final set of missing material parameters obtained from back analysis is listed in Table 3.2. In order to achieve an optimal correspondence of experimentally and numerically obtained load-displacement curves, φ_p was also adapted by means of back analysis. The initial angle of dilatancy was assumed to be zero. The respective numerical results are shown in Figure 3.9. Good agreement between numerically obtained $P/A_s - \bar{u}$ curves and the respective experimental data is observed (see Figure 3.9(a)). A_s represents the area of the shear plane, with $A_s = 30 \cdot 1$ mm^2. Figure 3.9(b) shows the $u_v - \bar{u}$ curves representing the volumetric dilation in consequence of plastic deformations. Since the parameter $\bar{\kappa}(\alpha_{DP})$ in the plastic potential (see Equation (3.79)) is assumed to be independent of hydrostatic pressure, almost the same results for the vertical displacements u_v are obtained from the numerical analysis. Nevertheless, in view of the rather simple plastic potential, a good approximation of the experimental results was achieved.
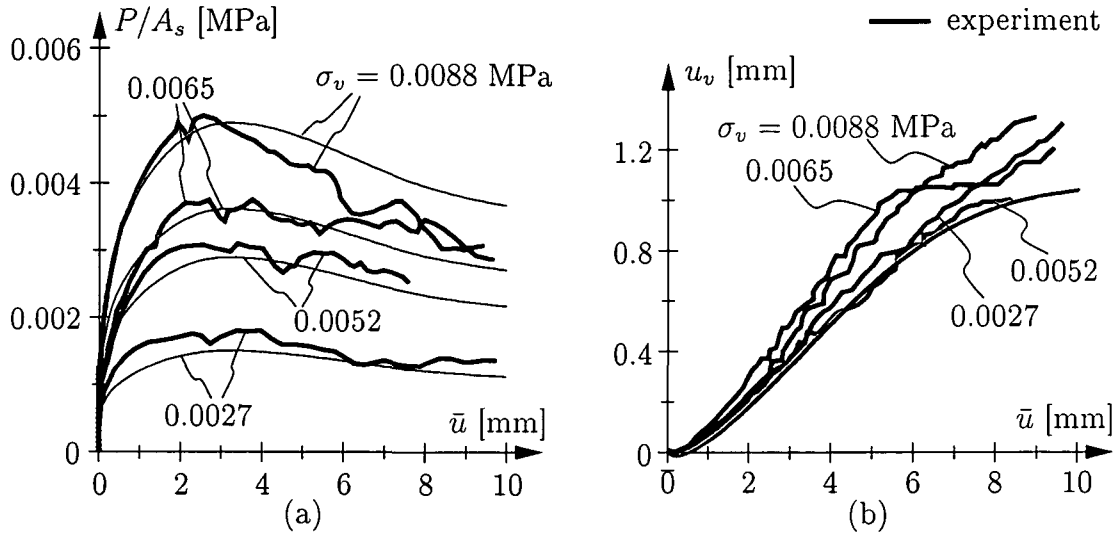
Figure 3.9: Determination of missing material parameters by means of back analysis: (a) $P/A_s - \bar{u}$ (A_s: area of shear plane, with $A_s = 30 \cdot 1$ mm^2) and (b) $u_v - \bar{u}$ curves obtained on the basis of the final set of parameters

3.3.3 Verification of the Mohr-Coulomb model: Triaxial compression tests (TU Graz)

A series of triaxial tests performed by the Geotechnical Laboratory of the Technical University of Graz, Austria, is used in addition to experimental results reported in [59] for the validation of the Mohr-Coulomb model. The tested and reported material consists mainly of sand with small fractions of clay and water. This natural granular soil is expected to be adequately modelled by means of the Mohr-Coulomb model presented in Section 3.3.1.

3.3.3.1 Determination of missing material parameters

The material properties given in [59] (see Table 3.3) are not sufficient for the Mohr-Coulomb model presented in Section 3.3.1. Therefore, six additional triaxial compression tests with

material parameters derived from torsional direct shear test	
peak friction angle, φ_p [°]	29.0
cohesion, c [MPa]	$0.55 \cdot 10^{-3}$

Table 3.3: Material properties for mixture of sand with 1% clay determined from torsional direct shear tests as given in [59]

three different confining pressures $\sigma_c = (3.0/6.0/10.0) \cdot 10^{-3}$ MPa were conducted in the Geotechnical Laboratory of the Graz University of Technology. These tests were perfomed
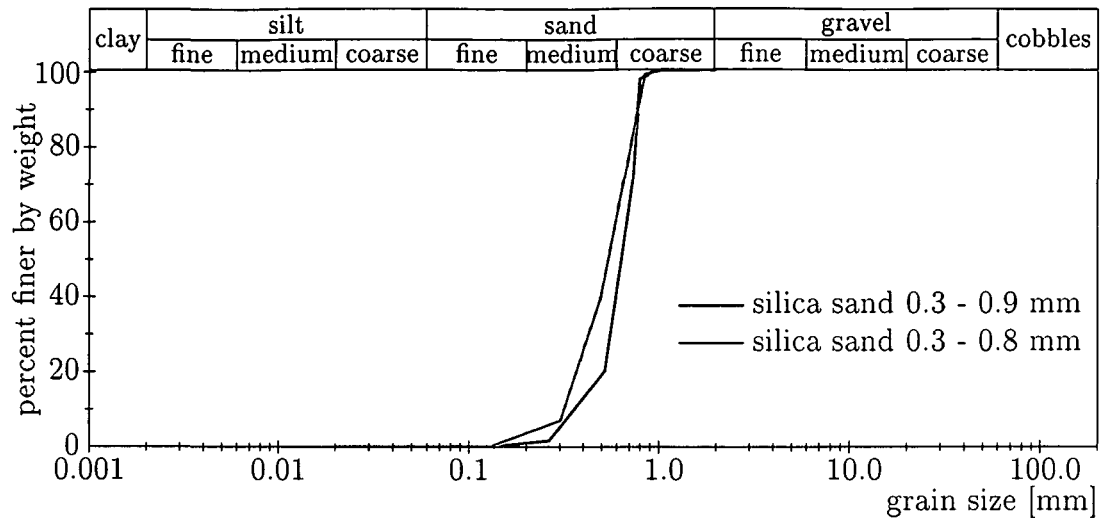
Figure 3.10: Grain size distributions of the silica sand used in [59] (0.3-0.8 mm) and of the silica sand used in the triaxial compression tests (0.3–0.9 mm)

with a material similar to the one used by Melix. As described in [59], the mixture used for the tunnel failure experiments consisted of a silica sand, a 1% clay fraction and a water content of 1.2% of the entire mixture. The silica sand was characterized by grain sizes ranging between 0.3 and 0.8 mm (see Figure 3.10). The 1% clay fraction was a kaolin from the pit Goldhausen in Germany.

This material was remixed in the Geotechnical Laboratory of the TU Graz using a silica sand with grain sizes ranging between 0.3 and 0.9 mm as depicted in Figure 3.10. The 1% clay fraction was also a kaolin from the pit Goldhausen in Germany. Like in [59], the entire mixture had an initial water content of 1.2%.

The material parameters estimated from the six conducted standard triaxial compression tests performed with a bulk unit weight of $\gamma = 14.24 \cdot 10^{-6}$ N/mm^3 are listed in Table 3.4. But still, the Mohr-Coulomb model requires some extra parameters accounting for the

set of material parameters derived from triaxial tests	
Young's modulus, E [MPa]	42.5/46.5/54.0
Poisson's ratio, ν [–]	0.36/0.45/0.48
peak friction angle, φ_p [°]	34.7
cohesion, c [MPa]	$9.0 \cdot 10^{-3}$

Table 3.4: Material properties for mixture of sand with 1% clay determined from triaxial compression tests with cell pressures of $\sigma_c = (3.0/6.0/10.0) \cdot 10^{-3}$ MPa

hardening/softening behavior and for the dilatancy behavior. They were determined by means of back analysis using the experimental results from the triaxial compression tests.
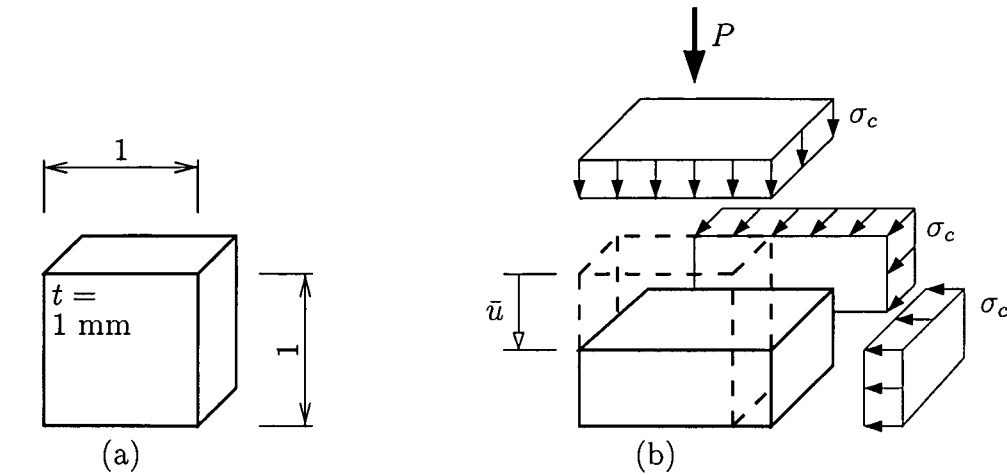
Figure 3.11: Determination of missing material parameters by means of back analysis: (a) geometric dimensions of employed model (in [mm]) and (b) applied mode of deformation ($\bar{u}$: prescribed displacement at top surface of finite element)

The employed numerical model is characterized by a single finite element (see Figure 3.11(a)). The applied loading is depicted in Figure 3.11(b) and consists of the application of an initial preconsolidation pressure followed by the increase of the axial displacement under constant cell pressure.

The final set of applied material parameters is listed in Table 3.5. In order to have a unique set of material parameters for the performed numerical simulations, all material parameters are assumed to be independent of the preconsolidation pressure.

The experimentally obtained results and the respective numerical results achieved with the material parameters listed in Table 3.5 are shown in Figure 3.12. Qualitatively, the tested soil resembles a material with medium density, as a small decrease of the axial load after the peak value in the load-displacement curve of the experiment (see Figure 3.12(a)) can be observed as well as as some overall volumetric dilation (see Figure 3.12(b)). This indicates that failure of the specimens occurred while dilatancy was still positive.

However, good agreement between numerically obtained $P/(2A) - \bar{u}$ curves and the respective experimental data is observed (see Figure 3.12(a)). Figure 3.12(b) shows the $\bar{I}_1 - \bar{u}$ curves representing the volumetric strains in consequence of axial deformations. As has been mentioned already in Section 3.3.1, almost the same results for the volumetric strain $\bar{I}_1$ are obtained from the numerical analyses, because the parameter $\bar{\kappa}_{MC}(\alpha_{MC})$ in the plastic potential (see Equation (3.80)) is assumed to be independent of the hydrostatic pressure. However, the assumption of a zero initial dilatancy angle clearly reflects the experimental result of the triaxial compression test, whereas the qualitative decrease in the dilatancy in the end of the numerical simulation is not observed in the experimentally obtained curves. This indicates that for this experiment the decrease in dilatancy does not simultaneously occur with the decrease in the axial load. Therefore, the assumption of

final set of material parameters	
[1] bulk unit weight, γ [N/mm^3]	$14.24 \cdot 10^{-6}$
[3] Young's modulus, E [MPa]	42.5
[3] Poisson's ratio, ν [-]	0.42
[2] cohesion, c [MPa]	0.009
[4] initial friction angle, φ_i [°]	23.0
[2] peak friction angle, φ_p [°]	33.5
[4] residual friction angle, φ_r [°]	33.49
[4] peak dilatancy angle, ψ_p [°]	4.0
[4] softening material parameter, G_f [mm]	0.01
[4] internal variable α_{MC} at $\varphi = \varphi_p$, $\alpha_{MC,m}$ [-]	0.03

[1] value obtained by measurement   [3] mean value of experimentally obtained values
[2] value obtained by experiment   [4] value obtained by back analysis

Table 3.5: Determination of missing material parameters by means of back analysis: final set of material parameters used in the numerical simulations

only *one* internal variable α_m governing the evolutions of the hardening parameter κ and of the dilatancy parameter $\bar{\kappa}$ might only hold for selected stress paths (see Section 3.3.2). Nevertheless, in view of the rather simple plastic potential, a satisfactory approximation of the experimental results was achieved.

3.3.4   Numerical aspects: Regularization of strain softening

In general, modeling of localized deformations such as shear bands results in a dependence of the finite element (FE) solution on the discretization. Several concepts to regain objectivity of the numerical results with respect to the element size were proposed in the open literature. They are ranging from non-local plasticity [4] and gradient plasticity [20] over the Cosserat theory [60] to the strong discontinuity approach [63, 82]. For the simulation of tunnel collapse, a regularization technique employing the element size as regularization parameter was used in [85]. This technique is commonly applied to the simulation of cracking of plain concrete [40]. The regularization parameter is referred to as *characteristic length*. Based on the *characteristic length*, the localized deformations are distributed over the size of the finite element. They are represented by the respective plastic strains (*smeared crack approach*). The analytical derivation concerning the *smeared crack approach* given in [44] and numerical results presented in [42] have shown an artificial increase of stress with increasing crack opening for mode I cracking of concrete, referred to as element locking. The amount of element locking was found to depend on the deviation of the direction of localization from the one of the edges of the finite element, with the localization in form of respective plastic strains. In this paper, the *characteristic length* is adapted aiming at a reduction of element locking in case of localized deformations.
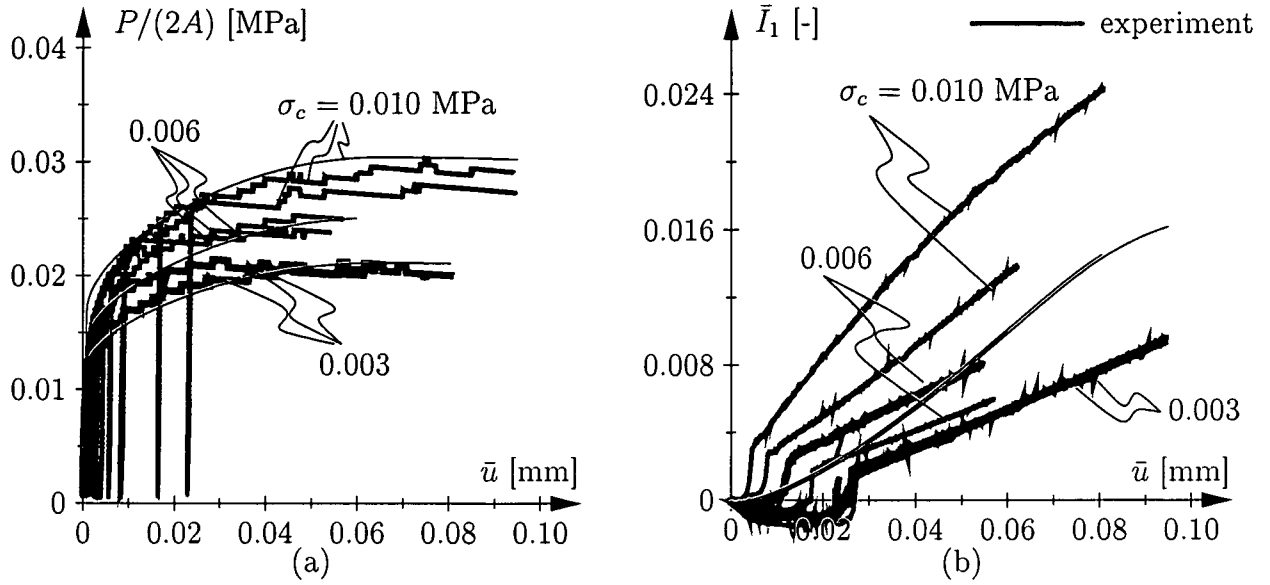
Figure 3.12: Determination of missing material parameters by means of back analysis: (a) $(P/(2A)) - \bar{u}$ (A: horizontal cross-section, with $A = 1 \cdot 1 \text{ mm}^2$ and (b) $\bar{I}_1 - \bar{u}$ curves obtained on the basis of the final set of parameters

In this work, a modification of the previously described calibration of the softening curve of the Drucker-Prager and Mohr-Coulomb criteria is proposed. The purpose of this modification is to compensate the effect of element locking in case of localization. This approach is based on the so-called *acoustic tensor*, and is used for the purpose of the adaptation of the *characteristic length*.

3.3.4.1   Adaptation of the softening curve

The *characteristic length* and, hence, the area under the softening curve is adapted in order to compensate the effect of element locking on the structural response. The adaptation is controlled by the deviation between the direction of the localization and the one of the element edges of the respective finite element.

In this work, only plane problems are considered. The orientation of an in-plane localization plane is defined by means of the angle ϑ enclosed by the x-axis and the normal $\mathbf{n}$ of the localization plane (see Figure 3.13(a)). For a given value of ϑ, the eigenvalue problem for the determination of localization reads

$$\left[Q_{jl}^{p}(\vartheta) - \mu^{p}(\vartheta)\delta_{jl} \right] m_l(\vartheta) = 0_j \; , \tag{3.124}$$

where μ^p denotes an eigenvalue of the acoustic tensor Q_{jl}^p, and m_l stands for the corresponding eigenvector. Physically, the eigenvalue μ^p is a measure of the stability of the material. Eigenvalues $\mu^p > 0$ indicate intact material, whereas eigenvalues $\mu^p \leq 0$ indicate
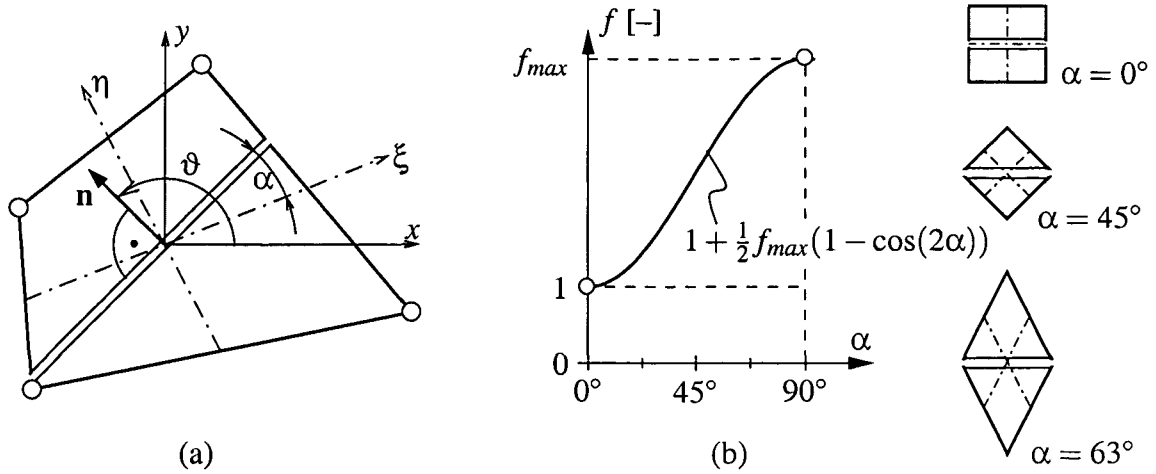
Figure 3.13: Adaptation of softening curve: (a) illustration of the minimum angle, α, enclosed by the localization plane and the isoparametric coordinate axis and (b) function $f(\alpha)$ proposed as magnification factor for the *characteristic length* ℓ_c (ξ, η: isoparameteric coordinate axes)

failure of material, i.e., localization. The eigenvector m_l gives the direction of propagation of the localization. The acoustic tensor Q_{jl}^p in Equation (3.124) is defined as [39]

$$Q_{jl}^p = C_{ijkl}^p n_i n_k \ , \tag{3.125}$$

where C_{ijkl}^p represents the elastoplastic tangent of the material model. The angle ϑ corresponding to the smallest eigenvalue μ_{min}^p represents

(a) in case of $\mu_{min}^p > 0$, the preferred normal direction of a future localization plane, and

(b) in case of $\mu_{min}^p = 0$, the normal direction of a localization plane.

For $\mu_{min}^p < 0$, localization has already occurred. For the adaptation of the softening curve, the angle α is introduced. α is the angle between the localization plane and the closest isoparametric coordinate axis (ξ or η) (see Figure 3.13(a)). The adaptation is performed by increasing the *characteristic length* ℓ_c by the factor f, giving

$$\ell_c^{incr} = f \ell_c \ . \tag{3.126}$$

f ranges from 1 for a localization plane parallel to an isoparametric coordinate axis, i.e., for $\alpha = 0$, to f_{max} for $\alpha = 90°$ (see Figure 3.13(b)). For $0° < \alpha < 90°$, a smooth function with vanishing derivatives at $\alpha = 0°$ and $90°$ is employed for the evaluation of $f(\alpha)$. Generally, f_{max} is obtained by means of back analysis. However, in the re-analysis of experiments, the maximum characteristic length, $\ell_c^{incr}(\alpha = 90°) = f_{max}\ell_c$, must not exceed the specimen size.
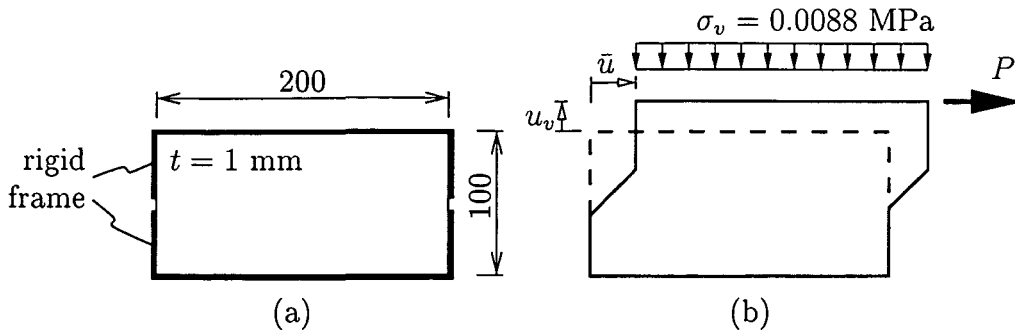
Figure 3.14: Direct shear test with $\sigma_v = 0.0088$ MPa: (a) geometric dimensions (in [mm]) and (b) applied mode of deformation
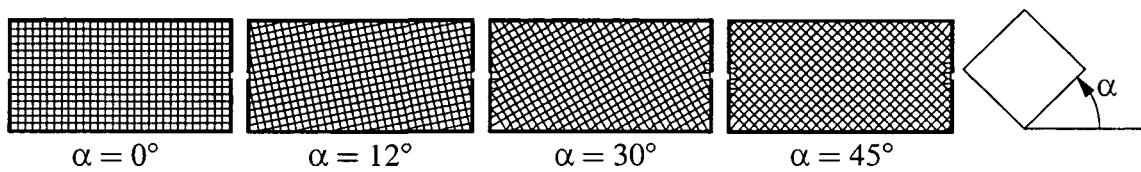

Figure 3.15: Direct shear test with $\sigma_v = 0.0088$ MPa: FE meshes

3.3.4.2 Assessment of the proposed regularization technique

The proposed adaptation of the *characteristic length* ℓ_c is assessed by means of re-analysis of the shear box test described in Section 3.3.2 with a vertical pressure of $\sigma_v = 0.0088$ MPa. In contrast to the analysis reported in Section 3.3.2, where only one element was used for the simulation of the shear band, the entire shear box is considered during the assessment of the regularization technique, see Figure 3.14. For this purpose, four different FE meshes (see Figure 3.15), characterized by different orientations of the element edges, are used. For all meshes, finite elements of similar size are used. This size is characterized by $\ell_c = 6.67$ mm. In this analysis, the tension-cut-off criterion was added (see Table 3.6). The initial state of

additional material parameter
tensile strength, f_{tu} [MPa] ≈ 0

Table 3.6: Direct shear test: additional material parameter for tension-cut-off criterion

the material is characterized by $\alpha_{DP} = \alpha_{DP,m}$. Hence, only softening is considered during the simulation. For the assessment of the proposed regularization technique, this mode of analysis is sufficient.

Figure 3.16 shows the obtained results using a constant value of ℓ_c^{incr}, with $\ell_c^{incr} = \ell_c$. Hence, $f_{max} = 1$. Expectedly, a great influence of the mesh orientation on both the applied load ($P/A_s - \bar{u}$ curve, Figure 3.16(a)) and the volumetric dilation ($u_v - \bar{u}$ curve,
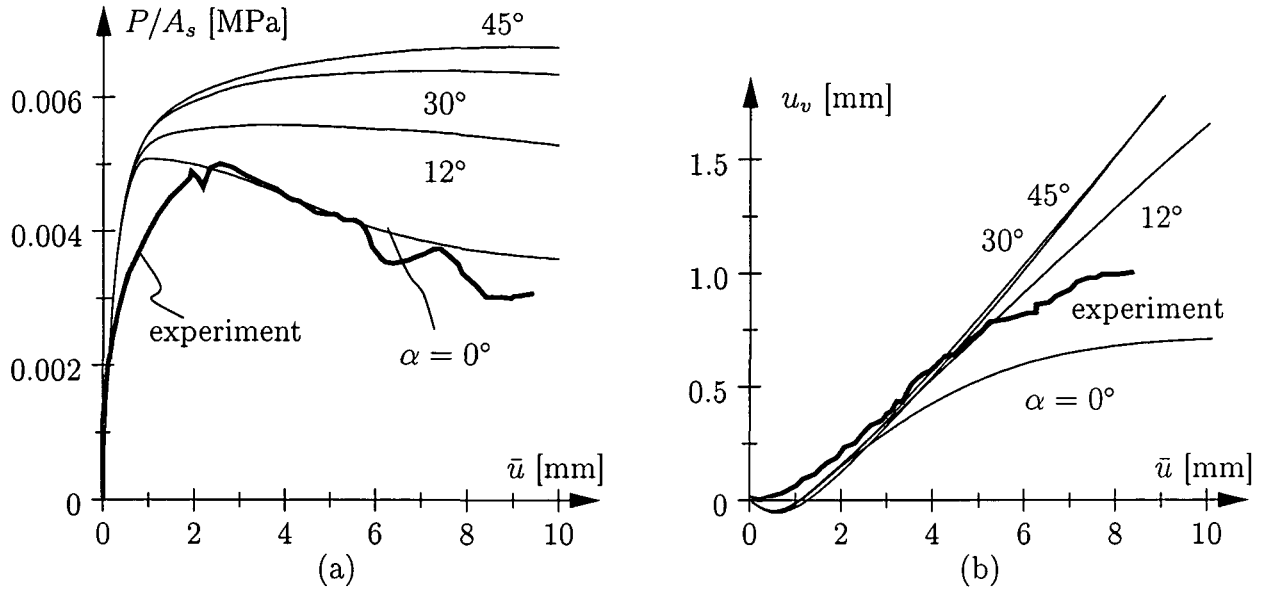
Figure 3.16: Direct shear test with $\sigma_v = 0.0088$ MPa: (a) $P/A_s - \bar{u}$ and (b) $u_v - \bar{u}$ curves obtained from constant ℓ_c on the basis of different FE meshes (A_s: area of shear plane, with $A_s = 200 \cdot 1$ mm^2)

Figure 3.16(b)) is observed. Moreover, for the analysis on the basis of the fourth mesh ($\alpha = 45°$), no softening is encountered. Additionally, the $u_v - \bar{u}$ curves of the analyses based on the meshes with $\alpha = 12°$, 30° and 45° show no tendency for vanishing dilation under continued shear. The results obtained from the analyses considering the adaptation of ℓ_c to the orientation of the element edges α are given in Figure 3.17. In these analyses, f_{max} was related to the maximum possible shear band width for this experiment: $f_{max} = 15$, giving $\ell_c^{incr}(\alpha = 90°) = 100$ mm. A considerable reduction of the influence of the mesh orientation is observed. Moreover, softening is encountered for all meshes (see Figure 3.17(a)). But still, the peak and residual shear resistance are overestimated for the rotated meshes. Also a reduction in the overestimation of the dilatancy is observed, although, still, little tendency for vanishing dilation under continued shear is observed for the analyses based on the meshes with $\alpha = 30°$ and 45°.

3.4 Material model for cohesive soil

A good description of the behavior of cohesive soils, i. e., clays, yields the so-called critical state theory [76]. This theory is based on the observation that under continued shearing cohesive material seems to reach a state, where volumetric strains become constant and the stress state does not change any more [76]. This specific state, where the soil behaves like a purely frictional material, is called a *critical state*.

This behavior of cohesive soil can adequately be formulated in the framework of the fol-
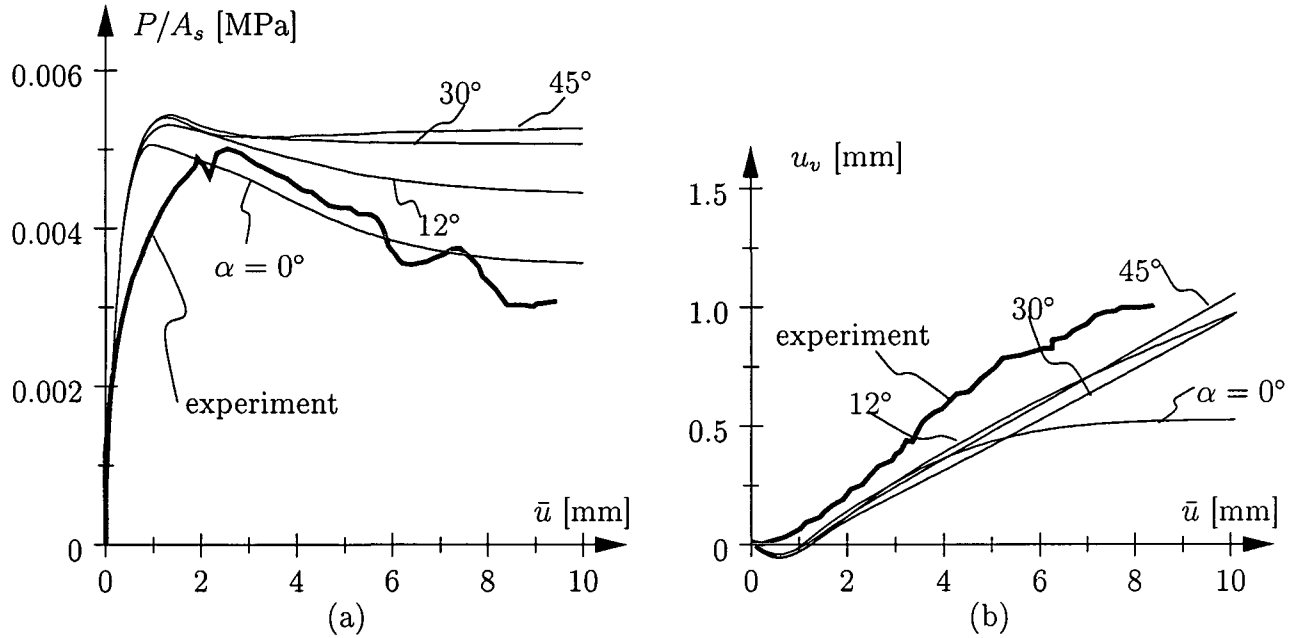
Figure 3.17: Direct shear test with $\sigma_v = 0.0088$ MPa: (a) $P/A_s - \bar{u}$ and (b) $u_v - \bar{u}$ curves obtained from variable ℓ_c on the basis of different FE meshes (A_s: area of shear plane, with $A_s = 200 \cdot 1$ mm^2)

lowing plasticity model of a Cam-Clay type.

3.4.1 Cam-Clay plasticity model

For clayey soil, the Cam-Clay model, emanating from the critical state theory, is chosen. Originally, the Cam-Clay model was developed by the "Cambridge group" [73]. Since then, several modifications have been proposed in the literature. Essentially, the Modified Cam-Clay model combines experimentally obtained yield surfaces of clays in the $p - \sqrt{3J_2}$ stress space with volume - hydrostatic pressure diagrams $V - \ln(-p)$, as can be obtained from consolidation tests. Based on these diagrams, the constitutive law, the equation of the yield surface, and the hardening/softening rule of the model are obtained.

3.4.1.1 Elastic behavior

According to experimental observations (see Figure 3.18), the compression modulus K is assumed to depend linearly on the hydrostatic pressure. In several formulations of the Cam-Clay model, the shear modulus G is kept constant. Hence, at low hydrostatic pressures, the Poisson's ratio $\nu = \nu(G, K)$ may become negative [41, 34]. A respective elastic potential $\mathcal{W}$ can be chosen as (see [73] for a similar approach)

$$\mathcal{W}^1\left(\boldsymbol{\varepsilon}^e\right) = t\,\frac{\kappa}{v_0}\,\exp\left(\frac{-v_0}{\kappa}\,\bar{I}_1^e\right) + 2\,G\bar{J}_2^e, \tag{3.127}$$
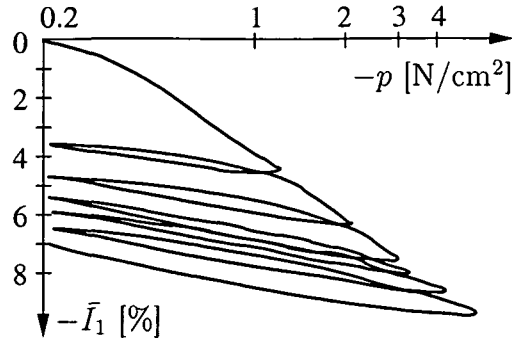
Figure 3.18: Linear relationship between volumetric strains $\bar{I}_1$ and hydrostatic pressure $(-p)$ (in log-scale) indicates linear dependence of the compression modulus on hydrostatic pressure; diagram from Namy (see [100])

where t is the hydrostatic strength of the soil and κ is the slope of the unloading-reloading parts of the $v - \ln p$ diagram. v_0 denotes the specific initial volume defined as $v_0 = v(t = 0) = V(t = 0)/V_{solidparticles}$. From the hyperelastic law, the stresses $\boldsymbol{\sigma}$ and the elasticity matrix $\mathbf{C}$ are obtained as

$$\boldsymbol{\sigma} = \underbrace{-t\left[\exp\left(\frac{-v_0}{\kappa}\bar{I}_1^e\right) - 1\right]}_{p}\mathbb{I} + 2\,G\,\boldsymbol{\varepsilon}_{dev}^e \,, \tag{3.128}$$

$$\mathbf{C} = \underbrace{-(p - t)\frac{v_0}{\kappa}}_{K}\mathbb{I}\otimes\mathbb{I} + 2\,G\,\mathbb{II}_{dev} \,, \tag{3.129}$$

where $\mathbb{I}$ is the unit diagonal matrix and $\mathbb{II}_{dev}$ is the deviatoric projection matrix[4]. Comparing Equation (3.129) with Hooke's law, the compression modulus K can be identified as $K = -(p - t)\frac{v_0}{\kappa}$. This leads to a pressure-dependent Poisson's ratio ν of the form

$$\nu = \frac{-3\,(p - t)\frac{v_0}{\kappa} - 2\,G}{-6\,(p - t)\frac{v_0}{\kappa} + 2\,G} \,. \tag{3.130}$$

As illustrated in Figure 3.19, the shortcoming of the model becomes clear: for small hydrostatic pressures inside the elastic regime Poisson's ratio becomes smaller than zero. This is physically unacceptable.

However, according to experimental observations by Houlsby [41], the shear modulus varies also with the hydrostatic pressure. To avoid negative values of the Poisson's ratio ν, Houlsby proposed a modification of the function of the stored energy in [41]. It takes coupling between volumetric and deviatoric response into account:

$$\mathcal{W}^2\left(\boldsymbol{\varepsilon}^e\right) = t\,\frac{\kappa}{v_0}\,\exp\left(\frac{-v_0}{\kappa}\bar{I}_1^e\right)\left(1 + \tilde{\alpha}\,\frac{v_0}{\kappa}\,2\bar{J}_2^e\right). \tag{3.131}$$

---

[4]The second term in the square brackets of Equation (3.128) is added in order to guarantee a stress-free state in the undeformed configuration.
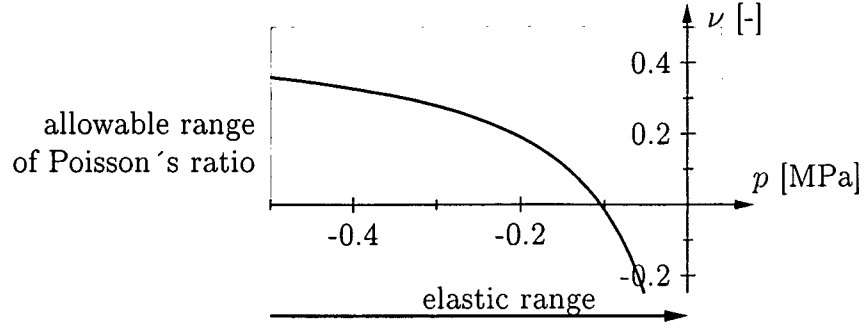
Figure 3.19: Dependence of Poisson's ratio ν on the hydrostatic pressure, based on the elastic potential $\mathcal{W}^1$ (see Equation (3.127)) $(t = 0)$

The parameter $\tilde{\alpha}$ introduced herein is a measure for the amount of the coupling between volumetric and deviatoric response. This form of the elastic potential was used in [9] and [13] within the framework of finite strain formulations based on the Cam-Clay model. As before, the stress tensor $\boldsymbol{\sigma}$ and the elasticity matrix $\mathbf{C}$ are obtained as

$$\boldsymbol{\sigma} = \underbrace{-t\left[\exp\left(\frac{-v_0}{\kappa}\bar{I}_1^e\right)\left(1 + \tilde{\alpha}\frac{v_0}{\kappa}2\bar{J}_2^e\right) - 1\right]\mathbb{1}}_{p} + \underbrace{2\,\tilde{\alpha}\,t\,\exp\left(\frac{-v_0}{\kappa}\bar{I}_1^e\right)}_{\tilde{G}}\boldsymbol{\varepsilon}_{dev}^e , \qquad (3.132)$$

$$\mathbf{C} = \underbrace{t\frac{v_0}{\kappa}\exp\left(\frac{-v_0}{\kappa}\bar{I}_1^e\right)\left(1 + \tilde{\alpha}\frac{v_0}{\kappa}2\bar{J}_2^e\right)}_{\tilde{K}}\mathbb{1}\otimes\mathbb{1} + \underbrace{2\,\tilde{\alpha}\,t\exp\left(\frac{-v_0}{\kappa}\bar{I}_1^e\right)}_{\tilde{G}}\mathbb{II}_{dev}$$

$$-2\,\tilde{\alpha}\,t\exp\left(\frac{-v_0}{\kappa}\bar{I}_1^e\right)\frac{v_0}{\kappa}\left(\boldsymbol{\varepsilon}_{dev}^e\otimes\mathbb{1} + \mathbb{1}\otimes\boldsymbol{\varepsilon}_{dev}^e\right) . \qquad (3.133)$$

Equation (3.132) illustrates the coupling between the volumetric strains and the deviatoric stresses as well as between the deviatoric strains and the hydrostatic pressure[5]. For predominantly deviatoric strains and small volumetric strains, however, this formulation leads to unreasonable stress-paths in the elastic range.

An improvement of the elastic law based on a modified form of the stored energy function $\mathcal{W}^2(\boldsymbol{\varepsilon}^e)$ can be obtained as follows: Essentially, compression and shear moduli are variable parameters like in [41, 13]. Extending the potential function by means of a similar exponential function yields a convex surface of the elastic potential in strain space. Moreover, an additional shift term delivers a state of zero energy in the undeformed configuration. Consequently, the so-obtained elastic potential reads as

$$\mathcal{W}^3\left(\boldsymbol{\varepsilon}^e\right) = t\frac{\kappa}{v_0}\left(1 + \tilde{\alpha}\frac{v_0}{\kappa}2\bar{J}_2^e\right)\left[\exp\left(\frac{-v_0}{\kappa}\bar{I}_1^e\right) + \exp\left(\frac{v_0}{\kappa}\bar{I}_1^e\right)\right] - 2\,t\frac{\kappa}{v_0} \qquad (3.134)$$

---

[5]Again, the second term in the square brackets of Equation (3.132) is added in order to guarantee a stress-free state in the undeformed configuration.

and the elastic law and the elastic tangent follow as

$$\boldsymbol{\sigma} = \underbrace{t\left(1 + \tilde{\alpha}\,\frac{v_0}{\kappa}2\bar{J}_2^e\right)\left[-\exp\left(\frac{-v_0}{\kappa}\,\bar{I}_1^e\right) + \exp\left(\frac{v_0}{\kappa}\,\bar{I}_1^e\right)\right]}_{p}\mathbb{1}$$

$$+\underbrace{2\,\tilde{\alpha}\,t\left[\exp\left(\frac{-v_0}{\kappa}\,\bar{I}_1^e\right) + \exp\left(\frac{v_0}{\kappa}\,\bar{I}_1^e\right)\right]}_{\tilde{G}}\boldsymbol{\varepsilon}_{dev}^e\,, \qquad (3.135)$$

$$\mathbf{C} = \underbrace{t\frac{v_0}{\kappa}\left(1 + \tilde{\alpha}\,\frac{v_0}{\kappa}2\bar{J}_2^e\right)\left[\exp\left(\frac{-v_0}{\kappa}\,\bar{I}_1^e\right) + \exp\left(\frac{v_0}{\kappa}\,\bar{I}_1^e\right)\right]}_{\tilde{K}}\mathbb{1}\otimes\mathbb{1}$$

$$+\underbrace{2\,\tilde{\alpha}\,t\left[\exp\left(\frac{-v_0}{\kappa}\,\bar{I}_1^e\right) + \exp\left(\frac{v_0}{\kappa}\,\bar{I}_1^e\right)\right]}_{\tilde{G}}\mathbb{II}_{dev}$$

$$-2\,\tilde{\alpha}\,t\frac{v_0}{\kappa}\left[-\exp\left(\frac{-v_0}{\kappa}\,\bar{I}_1^e\right) + \exp\left(\frac{v_0}{\kappa}\,\bar{I}_1^e\right)\right]\left(\boldsymbol{\varepsilon}_{dev}^e\otimes\mathbb{1} + \mathbb{1}\otimes\boldsymbol{\varepsilon}_{dev}^e\right). \quad (3.136)$$

This formulation for nonlinear elasticity leads to reasonable elastoplastic answers. Therefore, this formulation will be applied within this work.

In addition to this coupled non-linear elastic law, a simple, linear Hooke law shall be introduced for comparative purposes. This law and the respective elastic tangent read as

$$\boldsymbol{\sigma} = K\bar{I}_1\mathbb{1} + 2G\boldsymbol{\varepsilon}_{dev}^e\,, \qquad (3.137)$$

$$\mathbf{C} = K\mathbb{1}\otimes\mathbb{1} + 2G\mathbb{II}_{dev}\,. \qquad (3.138)$$

3.4.1.2 Yield surfaces

For the Modified Cam-Clay model, the elastic domain is bounded by a single yield surface in the $p - \sqrt{3J_2}$ stress space (see Figure 3.20), with M denoting the slope of the critical state line and q_{CC} standing for the actual size of the ellipse. This form of the yield surface agrees well with experiments on clay (see Figure 3.3(a)). It is noteworthy that the ellipsoidal yield surface in the stress space, originally emanating from $p = 0$ and stretching into the pressurized region, is shifted by an amount t into the tensile region. Thus, the stress-free state can be defined as lying inside the elastic regime. Additionally, cohesive material response without presence of hydrostatic pressure is also possible. The yield surface of the Cam-Clay model is described by the function

$$f_{CC}(\boldsymbol{\sigma}, q_{CC}) = \sqrt{3J_2 + M^2\left(p - t + \frac{q_{CC}}{2}\right)^2} - M\frac{q_{CC}}{2} \qquad (3.139)$$
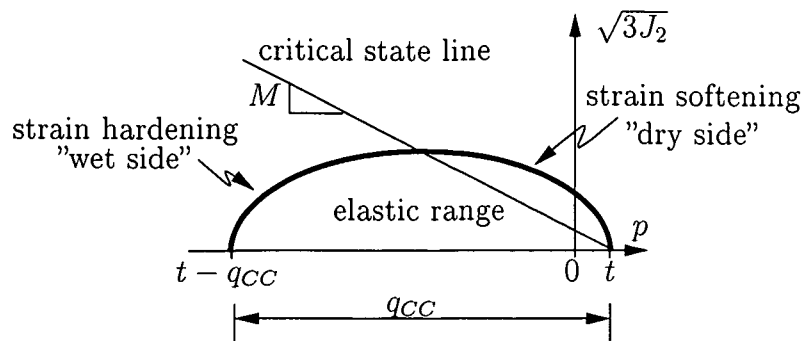
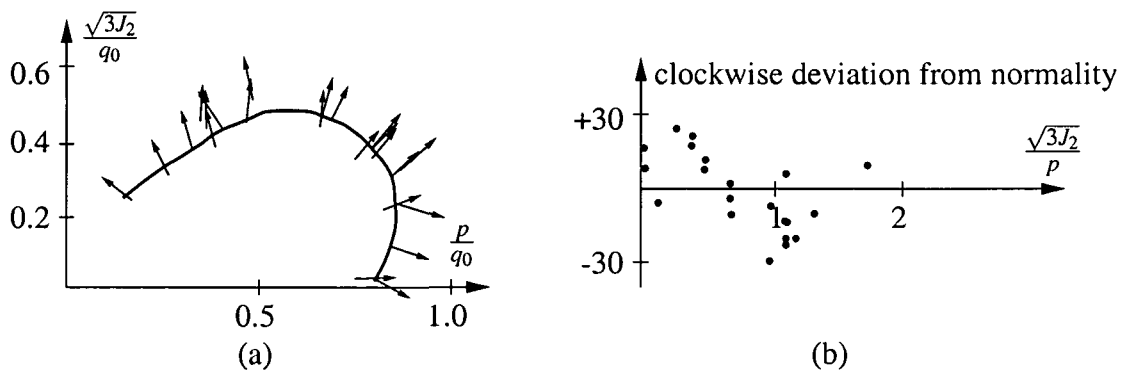Figure 3.20: Yield surface of the Cam-Clay model in stress space

Figure 3.21: Plastic strain increments derived from triaxial tests on undisturbed Winnipeg clay by Graham, Noonan and Lew (from [98])(q_0 denotes the initial size of the ellipsoidal yield surface in stress space)

3.4.1.3 Plastic flow rule

Cohesive soil can experience volume dilation as well as volume compaction under shear deformation. The type of volumetric deformation occurring depends on the actual density of the material, represented by the size of the ellipsoidal yield surface, and on the stress path in the $p - \sqrt{3J_2}$ stress space. Experiments by Graham, Noonan and Lew on undisturbed Winnipeg clay (see [98] and Figure 3.21) indicate normality of plastic strain increments with respect to the current yield surface. Therefore, the evolution of the plastic strains is assumed to be associative, reading as

$$\dot{\varepsilon}^p = \gamma_{CC} \, \partial_{\sigma} f_{CC} \, . \tag{3.140}$$

3.4.1.4 Hardening/softening rule

Depending on the loading state, strain hardening or strain softening is captured by the model. On the "dry" side of the critical state line, loading of clays exhibits softening

behavior connected with a volume increase. On the "wet" side of this line, hardening connected with compaction occurs. This behavior reflects the experimental findings made by Parry [66]. However, when the material has reached a critical state, continuation of shear does not alter the volume of the material any more.

In this work, however, the critical state concept is applied in a modified version. Based on the fact that the hardening/softening rule for the Cam-Clay model evolves from the volume - hydrostatic pressure diagram, this diagram will be modified such that a straightforward derivation of the hardening/softening rule is achieved.

First, the actual soil volume V in the volume - hydrostatic pressure diagram $V - \ln p$ is replaced by the specific volume v, defined as

$$v = \frac{V_{actual}}{V_{solid\,particles}} \, , \tag{3.141}$$

where v is not allowed to become less than 1.0, meaning $V_{actual} = V_{solid\,particles}$.

Next, the evolution of total volumetric strain can be expressed as

$$\dot{\bar{I}}_1 = \frac{\dot{v}}{v_0} \, . \tag{3.142}$$

Equation (3.142) implies that no significant volume changes occur[6]. To account for the shift of the yield surface by the amount t, the specific volume - hydrostatic pressure diagram $v - \ln p$ also has to be shifted by the same amount. This shift leads to a problem of representation, as the initial specific volume v_0 cannot be illustrated for $p = 0$ in the logarithmic scale. For this reason, the x-axis of the diagram is shifted by the amount t as depicted in Figure 3.22.

The total volumetric strains can be decomposed additively into an elastic and a plastic part. Using the information contained in Figure 3.22, this results in the following relation:

$$\bar{I}_1 = \frac{(v - v_0)}{v_0} = \bar{I}_1^e + \bar{I}_1^p = \frac{(v - v_\kappa)}{v_0} + \frac{(v_\kappa - v_0)}{v_0}, \tag{3.143}$$

with v denoting the actual specific volume and v_κ standing for the specific volume corresponding to the initial hydrostatic pressure $-(p_0 - t)$. Inserting the expression for $(v_\kappa - v_0)$ (see Figure 3.22) into $\bar{I}_1^p = (v_\kappa - v_0)/v_0$ from Equation (3.143), the nonlinear hardening law

$$q_{CC} = (q_0 - t) \exp\left(\frac{-v_0}{\lambda - \kappa} \bar{I}_1^p\right) + t \, , \tag{3.144}$$

with q_0 denoting the initial preconsolidation pressure and λ denoting the slope of the normal compression line, is obtained. This hardening law describes volumetric hardening, which is suitable for soft clays [98]. It can be seen from Equation (3.144) that the evolution of the yield surface depends on volumetric plastic strain. This volumetric plastic strain

---

[6]Wood [98] proposes a similar definition, but he refers to a large-strain formulation to account for large compressibility of soft soils.
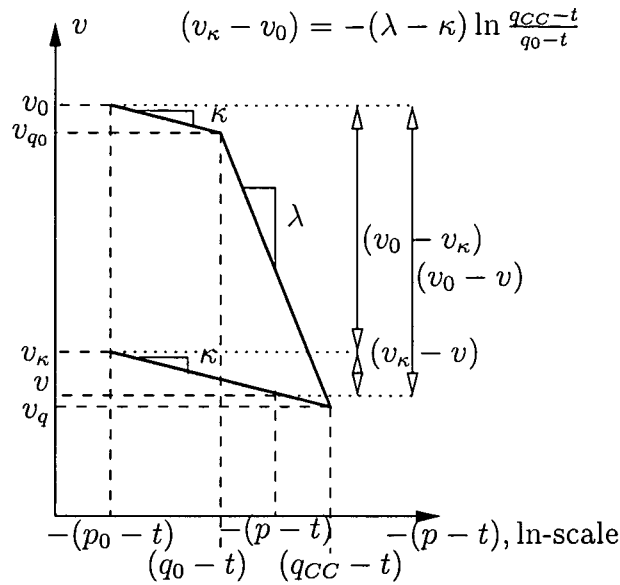
Figure 3.22: Linear relation between v and $-(p-t)$,ln-scale

describes irrecoverable changes in the packing of soil particles – a change in the specific volume or void ratio. As volumetric strain is naturally related to hydrostatic pressure, the evolution of the volumetric plastic strain is defined as

$$\dot{I}_1^p = \dot{\alpha}_{CC} = \gamma_{CC}\,\partial_p f_{CC}\ ; \tag{3.145}$$

thus, the evolution of hardening/softening is nonassociated.

Remark concerning the elastic law. Originally, the elastic volumetric law of the Cam-Clay model evolves from the volume - hydrostatic pressure diagram. However, in this work, an elastic potential was used to derive the elastic law. Obviously, the expressions for volumetric stresses derived from the elastic potential and from the specific volume - hydrostatic pressure diagram are not identical. However, a numerical simulation of a hydrostatic compression test shows that both formulations yield a very similar elastic answer, provided that t is small enough.

Remark concerning the parameters λ und κ. The slopes λ and κ of the normal compression line and the unloading-reloading lines are dimensional parameters. This results from the underlying specific volume - hydrostatic pressure diagram, where the abscissa is of a unit of pressure, and the ordinate is dimensionless. However, in the formulations of the elastic potential, the constitutive law, and the hardening/softening rule, the parameters λ and κ are considered to be dimensionless. This is in accordance with existing Cam-Clay models (see [98, 76]).

3.4.1.5   Time integration of the evolution equations

As outlined in Section 3.2.2, for the time integration of the evolution equations the Return Map Algorithm is applied [79]. For the Cam-Clay model, the implicit integration scheme yields (see Equations (3.11) and (3.12))

$$
\mathbf{R}(\boldsymbol{\varepsilon}_{n+1}^p, \alpha_{CC,n+1} | \Delta\gamma_{CC,n+1}) = \left\{ \begin{array}{c} R^{\boldsymbol{\varepsilon}^p} \\ R^{\alpha_{CC}} \\ \hline R^{f_{CC}} \end{array} \right\} \tag{3.146}
$$

$$
= \left\{ \begin{array}{c} -\boldsymbol{\varepsilon}_{n+1}^p + \boldsymbol{\varepsilon}_n^p + \Delta\gamma_{CC,n+1}\partial_{\boldsymbol{\sigma}} f_{CC,n+1} \\ -\alpha_{CC,n+1} + \alpha_{CC,n} + \Delta\gamma_{CC,n+1}\partial_p f_{CC,n+1} \\ \hline f_{CC,n+1} \end{array} \right\} = \mathbf{0} \ .
$$

Here, the matrices ∇f_{CC}, ∇g_{CC}, and $\mathbf{A}^{-1}$ are given as

$$
\nabla f_{CC} = \left\{ \begin{array}{c} \partial_{\boldsymbol{\sigma}} f_{CC} \\ \partial_{q_{CC}} f_{CC} \end{array} \right\} , \quad \nabla g_{CC} = \left\{ \begin{array}{c} \partial_{\boldsymbol{\sigma}} f_{CC} \\ \partial_p f_{CC} \end{array} \right\} , \tag{3.147}
$$

$$
\mathbf{A}^{-1} = \left\{ \begin{bmatrix} \mathbf{C}^{-1} & 0 \\ 0 & D_{CC}^{-1} \end{bmatrix} + \begin{bmatrix} \Delta\gamma_{n+1}\partial_{\boldsymbol{\sigma\sigma}}^2 f_{CC} & \Delta\gamma_{n+1}\partial_{\boldsymbol{\sigma} q_{CC}}^2 f_{CC} \\ \Delta\gamma_{n+1}\partial_{\boldsymbol{\sigma} p}^2 f_{CC} & \Delta\gamma_{n+1}\partial_{pq_{CC}}^2 f_{CC} \end{bmatrix} \right\} . \tag{3.148}
$$

For the Cam-Clay model, the stresses are obtained as

$$
\boldsymbol{\sigma}_{n+1} = p_{n+1}\mathbb{1} + 2\tilde{G}\boldsymbol{\varepsilon}_{dev,n+1}^e \quad \text{with} \quad \boldsymbol{\varepsilon}_{dev,n+1}^e = \mathbb{I}_{dev}\left(\boldsymbol{\varepsilon}_{n+1} - \boldsymbol{\varepsilon}_{n+1}^p\right) , \tag{3.149}
$$

with p_{n+1} and $\tilde{G}$ given as:

- for the Cam-Clay model using the potential $\mathcal{W}^1$:

$$
p_{n+1} = -t\left[\exp\left(\frac{-v_0}{\kappa}\left(\bar{I}_1 - \bar{I}_1^p\right)\right) - 1\right] \tag{3.150}
$$

$$
\tilde{G} = G, \tag{3.151}
$$

- for the Cam-Clay model using the potential $\mathcal{W}^2$:

$$
p_{n+1} = -t\left[\exp\left(\frac{-v_0}{\kappa}\left(\bar{I}_1 - \bar{I}_1^p\right)\right)\left(1 + \tilde{\alpha}\frac{v_0}{\kappa}2\left(\bar{J}_2 - \bar{J}_2^p\right)\right) - 1\right] \tag{3.152}
$$

$$
\tilde{G} = \tilde{\alpha}\,t\exp\left(\frac{-v_0}{\kappa}\left(\bar{I}_1 - \bar{I}_1^p\right)\right) , \tag{3.153}
$$

- for the Cam-Clay model using the potential $\mathcal{W}^3$:

$$p_{n+1} = t\left(1 + \tilde{\alpha}\frac{v_0}{\kappa}2\left(\bar{J}_2 - \bar{J}_2^p\right)\right)\left[-\exp\left(\frac{-v_0}{\kappa}\left(\bar{I}_1 - \bar{I}_1^p\right)\right)\right.$$
$$\left. + \exp\left(\frac{v_0}{\kappa}\left(\bar{I}_1 - \bar{I}_1^p\right)\right)\right] \tag{3.154}$$

$$\tilde{G} = \tilde{\alpha}\,t\left[\exp\left(\frac{-v_0}{\kappa}\left(\bar{I}_1 - \bar{I}_1^p\right)\right) + \exp\left(\frac{v_0}{\kappa}\left(\bar{I}_1 - \bar{I}_1^p\right)\right)\right], \tag{3.155}$$

- for the linear elastic Cam-Clay model:

$$p_{n+1} = K\bar{I}_1 \tag{3.156}$$
$$\tilde{G} = G. \tag{3.157}$$

3.4.1.6 Consistent elastoplastic tangent modulus

The consistent tangent modulus, $\mathbf{C}_{T,n+1} = d\boldsymbol{\sigma}_{n+1}/d\boldsymbol{\varepsilon}_{n+1}$, is given by extracting the respective submatrix of

$$\left\{\begin{array}{c} d\boldsymbol{\sigma}_{n+1} \\ dq_{CC,n+1} \end{array}\right\} = \left[\mathbf{A} - g^{inv}\mathbf{A}\nabla g_{CC}\nabla f_{CC}^T\mathbf{A}\right]\left\{\begin{array}{c} d\boldsymbol{\varepsilon}_{n+1} \\ 0 \end{array}\right\}, \tag{3.158}$$

with

$$g = \nabla f_{CC}^T\mathbf{A}\nabla g_{CC}. \tag{3.159}$$

3.4.1.7 Extension to account for viscoplastic behavior

For the nonlinear elastic Cam-Clay model, where the elastic domain is bounded by a single loading surface, the Perzyna-type of viscoplastic formulation is applied (see Section 3.2.5.2). Here, the evolution of the viscoplastic flow and the evolution of the strain-like internal variable are postulated according to Equations (3.140) and (3.145) as

$$\dot{\boldsymbol{\varepsilon}}^{vp} = \frac{\langle f_{CC}\rangle}{\eta}\partial_{\boldsymbol{\sigma}}f_{CC}, \tag{3.160}$$

$$\alpha_{\dot{C}C} = \frac{\langle f_{CC}\rangle}{\eta}\partial_p f_{CC}. \tag{3.161}$$

Hence, the residual formulation reads according to Equation (3.63)

$$\mathbf{R}(\boldsymbol{\varepsilon}_{n+1}^{vp}, \alpha_{CC,n+1}|\Delta\gamma_{CC,n+1}) = \left\{\begin{array}{c} R^{\boldsymbol{\varepsilon}^{vp}} \\ R^{\alpha cc} \\ \hline R^{\Delta\gamma cc} \end{array}\right\} \tag{3.162}$$

$$= \left\{\begin{array}{c} -\boldsymbol{\varepsilon}_{n+1}^p + \boldsymbol{\varepsilon}_n^p + \frac{\Delta t_{n+1}}{\eta}f_{n+1}\partial_{\boldsymbol{\sigma}}f_{CC,n+1} \\ -\alpha_{CC,n+1} + \alpha_{CC,n} + \frac{\Delta t_{n+1}}{\eta}f_{n+1}\partial_p f_{CC,n+1} \\ \hline -\Delta\gamma_{CC,n+1} + \frac{\Delta t_{n+1}}{\eta}f_{CC,n+1} \end{array}\right\} = \mathbf{0}.$$

Together with the matrix $\tilde{\mathbf{A}}^{-1}$ specified for the Cam-Clay model as

$$\tilde{\mathbf{A}}^{-1} = \left\{ \begin{bmatrix} \mathbf{C}^{-1} & \mathbf{0} \\ \mathbf{0} & \mathbf{D}^{-1} \end{bmatrix} \right. \tag{3.163}$$

$$\left. + \frac{\Delta t_{n+1}}{\eta} \begin{bmatrix} \partial_{\boldsymbol{\sigma}} f_{CC}\, \partial_{\boldsymbol{\sigma}} f_{CC} + f_{CC}\, \partial^2_{\boldsymbol{\sigma}\boldsymbol{\sigma}} f_{CC} & \partial_q f_{CC}\, \partial_{\boldsymbol{\sigma}} f_{CC} + f_{CC}\, \partial^2_{q\boldsymbol{\sigma}} f_{CC} \\ \partial_{\boldsymbol{\sigma}} f_{CC}\, \partial_p f_{CC} + f_{CC}\, \partial^2_{\boldsymbol{\sigma} p} f_{CC} & \partial_q f_{CC}\, \partial_p f_{CC} + f_{CC}\, \partial^2_{qp} f_{CC} \end{bmatrix} \right\} ,$$

the increments in the viscoplastic strains and in the internal variable are obtained according to Equation (3.64). As in the rate-independent solution, the stresses in the Newton scheme are obtained as

$$\boldsymbol{\sigma}_{n+1} = p_{n+1}\mathbb{1} + 2\tilde{G}\boldsymbol{\varepsilon}^e_{dev,n+1} \quad \text{with} \quad \boldsymbol{\varepsilon}^e_{dev,n+1} = \mathbb{1}_{dev}\left(\boldsymbol{\varepsilon}_{n+1} - \boldsymbol{\varepsilon}^p_{n+1}\right) . \tag{3.164}$$

3.4.1.8 Consistent elasto-viscoplastic tangent modulus

The consistent tangent modulus, $\mathbf{C}_{T,n+1} = d\boldsymbol{\sigma}_{n+1}/d\boldsymbol{\varepsilon}_{n+1}$, is given by extracting the respective submatrix of

$$\left\{ \begin{array}{c} d\boldsymbol{\sigma}_{n+1} \\ dq_{n+1} \end{array} \right\} = \left[\mathbf{A} - \tilde{g}^{inv}\mathbf{A}\boldsymbol{\nabla} f \boldsymbol{\nabla} f^T \mathbf{A}\right] \left\{ \begin{array}{c} d\boldsymbol{\varepsilon}_{n+1} \\ 0 \end{array} \right\} , \tag{3.165}$$

where

$$\tilde{g} = \frac{\eta}{\Delta t_{n+1}} + \boldsymbol{\nabla} f^T \mathbf{A} \boldsymbol{\nabla} f . \tag{3.166}$$

3.4.2 Verification: Triaxial compression test (TU Graz)

Two triaxial compression tests are used for validation of the Cam-Clay model presented in Section 3.4.1. They were conducted in the Laboratory of the Institute for Rock Mechanics and Tunneling of Graz University of Technology, using a clay marl from the Sieberg construction site near St. Valentin, Austria. Apart from the compression test results, also information from an experts' report on the clay marl were accessible thanks to the Institute for Rock Mechanics and Tunneling of Graz University of Technology. Both sources are used for calibration of the Cam-Clay model.

However, as the considered clay marl is present in form of a stone-like material, the material parameters to be determined here will lie outside the typical range of Cam-Clay parameters corresponding to compressible clays. In the following, the parameter determination is presented as well as the capability of the proposed Cam-Clay model to reproduce experimental behavior.

3.4.2.1 Determination of material parameters

From standard laboratory tests performed by a professional company in the course of the compilation of an experts' report on present soil characteristics, some material properties of the undisturbed miocene clay marl were known. As shown by the Table (see Table 3.7), the material properties are given with respect to the loading direction. The reason for this is a fine horizontal stratification of the material which will be discussed in a subsequent paragraph. However, for the Cam-Clay model, these parameters are not sufficient. Therefore,

information provided on material properties of clay marl		
[1] bulk unit weight, γ [MN/m^3]	0.0231 – 0.0240	
	vertical loading	horizontal loading
[1] uniaxial compressive strength, σ_{cu} [MPa]	3.0 – 5.0	2.0 – 4.0
[2] maximum friction angle , φ_{max}	50°	45°
[2] maximum cohesion , c_{max} [MPa]	0.60	0.40
[1] general variation	[2] design value for tunnel construction stage	

Table 3.7: Material properties of miocene marl acc. to an experts' report

two triaxial compression tests were conducted, consisting of three hydrostatic load cycles and subsequent uniaxial compression under constant confinement (see Figure 3.23(a)). For this purpose, a triaxial testing apparatus provided by the laboratory of the Institute for Rock Mechanics and Tunneling of TU Graz, Austria, was used. Unfortunately, the resulting material behavior was strongly anisotropic as can be seen by comparison of the stress and strain paths of the hydrostatic part of the experiments (see Figure 3.23(b) and (c)). However, the measurement of the axial strains shows homogeneous axial deformation during the experiment (see Figure 3.24).

The results obtained from the triaxial compression tests are depicted in Figure 3.25: Both tests yield a similar answer in both the volumetric stress-strain behavior as well as in the deviatoric stress-strain behavior.

The employed numerical model consists of a single finite element with unit dimensions (1 mm · 1 mm · 1 mm). The applied loading conditions consist of

- first, hydrostatic pressure loading and unloading cycles with
  $p \in (1.26; 0.26; 5.05; 0.20; 5.05; 0.56)$ MPa for test 1 and
  $p \in (1.14; 0.21; 4.91; 0.23; 11.99; 0.34)$ MPa for test 2; and

- second, vertical deformation $\bar{u}$ up to $\bar{u} = 0.008$ mm for test 1 and $\bar{u} = 0.010$ mm for test 2 under constant confinement of $\sigma_3 = 0.56$ MPa for test 1 and $\sigma_3 = 0.34$ MPa for test 2.

For the calibration of the Cam-Clay material model, some material properties can be determined based on the existing data from the experts' report: the cohesion c and the
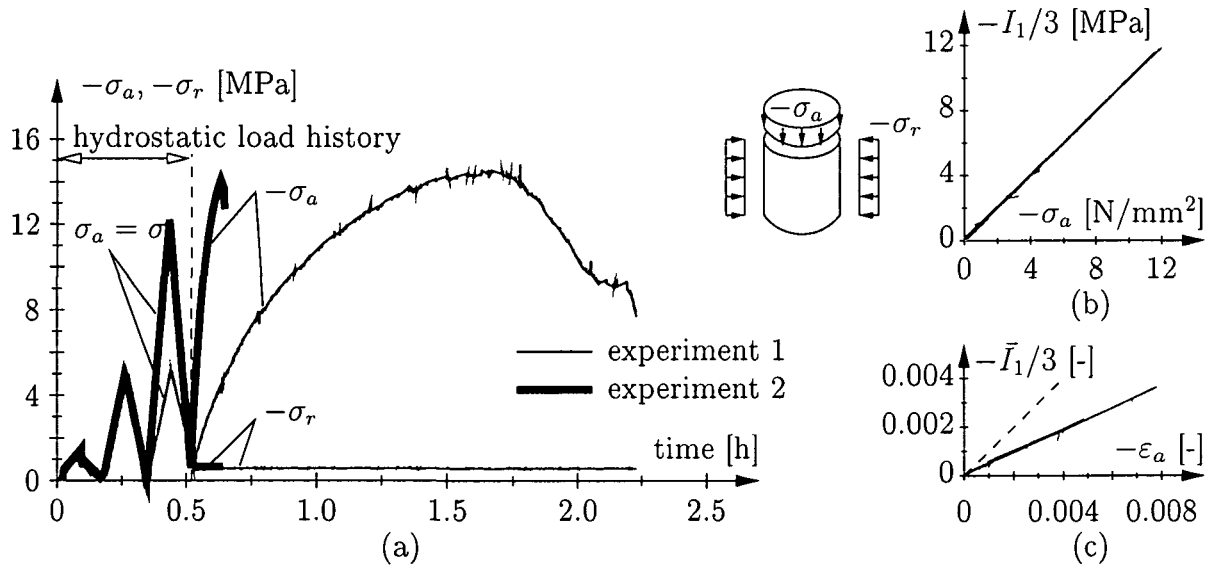
Figure 3.23: Stress and strain paths paths followed and observed in the two triaxial compression tests: (a) history of vertical and radial stress imposed upon the specimens; (b) isotropy of stress path for $t \leq 0.52$; and (c) observed anisotropy of strain path for $t \leq 0.52$
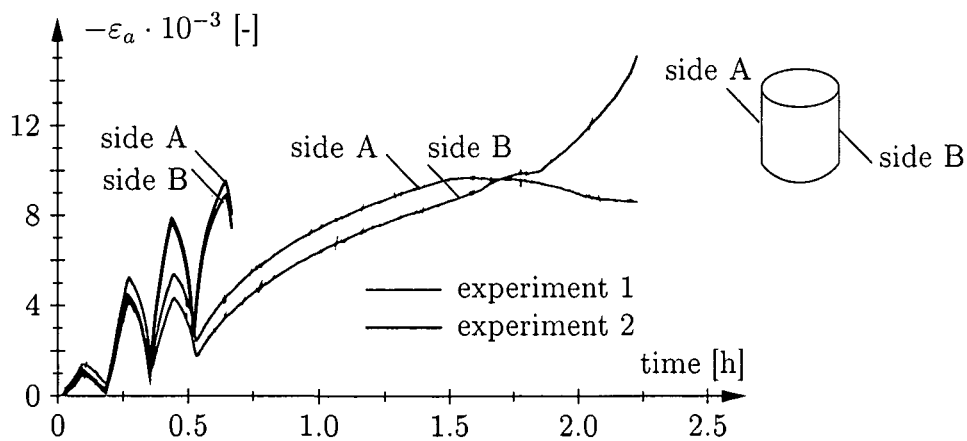

Figure 3.24: Result from triaxial compression test: Axial strains over time measured at two opposite sides of the two test specimens
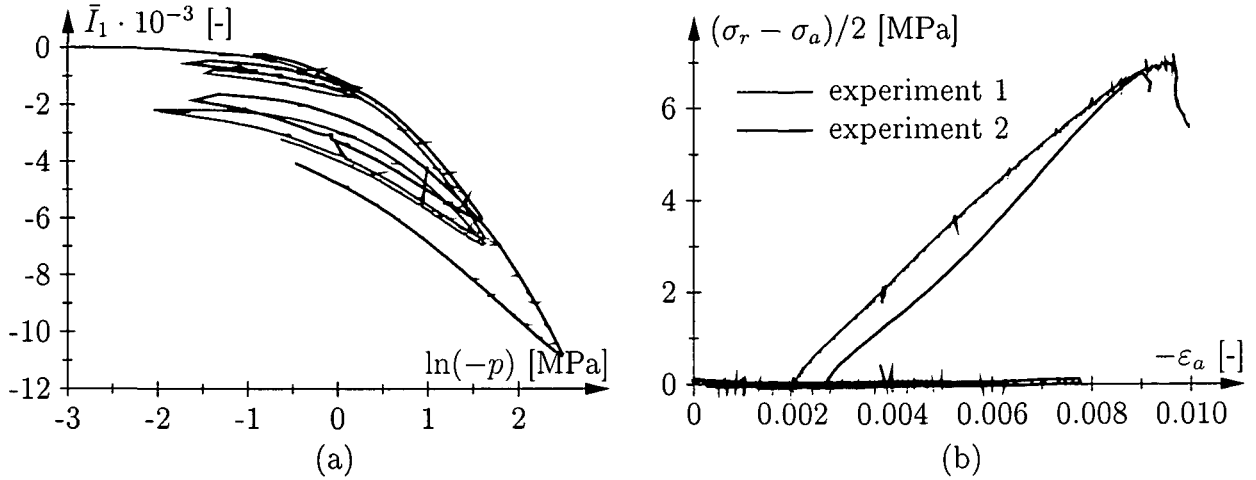
Figure 3.25: Results from triaxial compression test: (a) Volumetric strain vs. hydrostatic pressure diagram for $t \leq 0.52$ and (b) deviatoric stress vs. axial strain diagram from both experiments

friction angle φ can be related to the slope of the critical state line M and to the hydrostatic tensile resistance t as

$$M = \frac{6 \sin \varphi}{3 \pm \sin \varphi} \qquad t = \frac{c}{\tan \varphi} . \qquad (3.167)$$

As the triaxial compression test is refers to the compressive meridian in the stress space, $M = 6 \sin \varphi / (3 - \sin \varphi)$. The parameters λ, κ, and q_0 are read from the volumetric strain - hydrostatic pressure diagram depicted in Figure 3.26. The initial specific volume $v_0 = V_0 / V_{solid\,particles}$ was estimated on the basis of the following argumentation: the volume of the solid particles was assumed to be the minimum volume of the two compressed specimens obtained during the laboratory experiments. This minimum volume was obtained in the course of experiment 2 during confined uniaxial compression. Therefore, the initial specific volume was assumed as

$$v_0 = \frac{V_0}{V_{solid\,particles}} \approx \frac{V_0}{V_{min}} = \frac{\pi R^2 H}{\pi r^2 h} = 1.012 . \qquad (3.168)$$

The remaining parameter $\tilde{\alpha}$, denoting the amount of volumetric-deviatoric coupling in elasticity, was determined by means of back analysis from the confined uniaxial compression tests.

For the linear elastic model, the compression modulus K, the shear modulus G, and Young's modulus E can be determined as depicted in Figure 3.27. As only two variables are independent in Hooke's law, Young's modulus E was only used for confirmation purposes. For completeness, the resulting Poisson's ratio is in the physically reasonable range.

The material parameters obtained from the numerical analyses are summarized in Table 3.8.
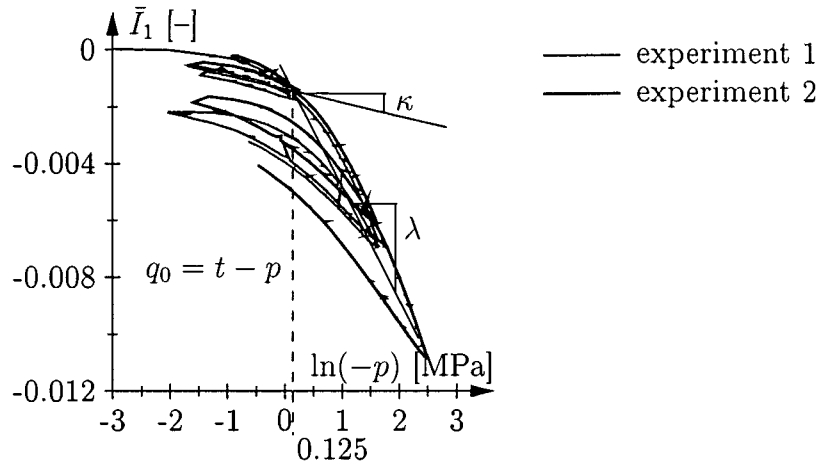
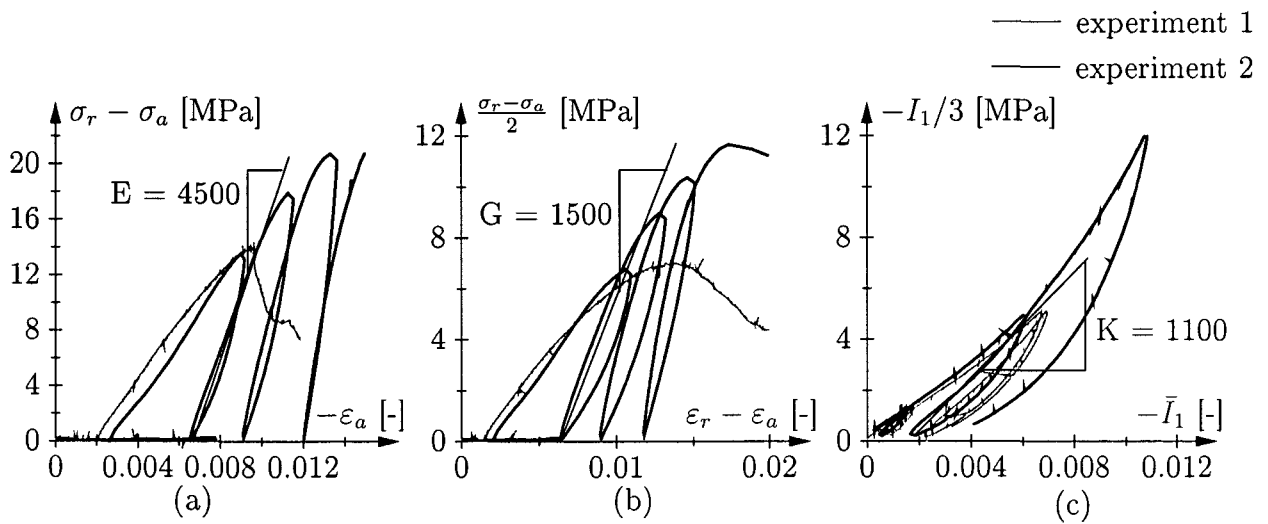Figure 3.26: Estimation of the Cam-Clay parameters q_0, λ and κ from experimental results

Figure 3.27: Determination of material parameters: (a) Young's modulus E, (b) shear modulus G, and (c) bulk modulus K of clay marl from reloading branch of the triaxial compression test

Figure 3.28: Determination of missing material parameters: (a) specific volume - hydrostatic pressure curve, (b) deviatoric stress - axial strain curve for experiment 1, obtained from the final set of parameters
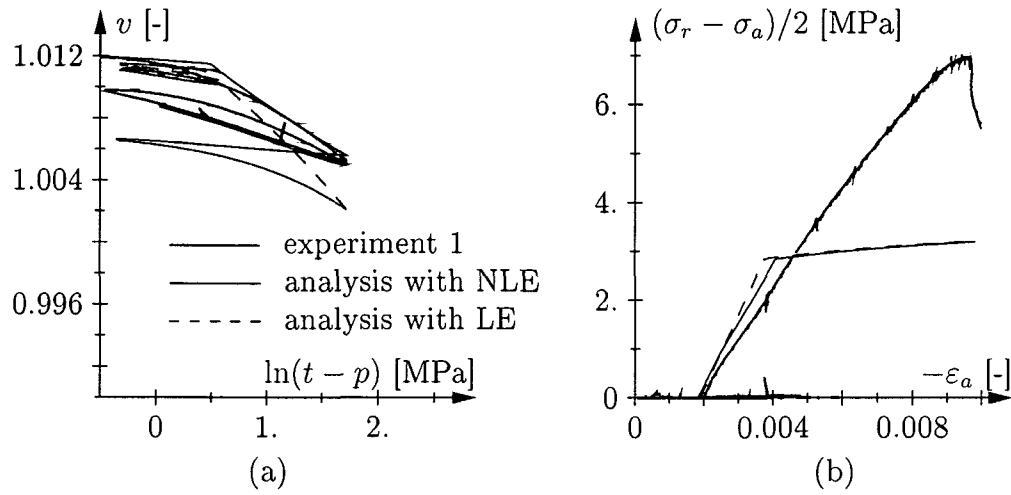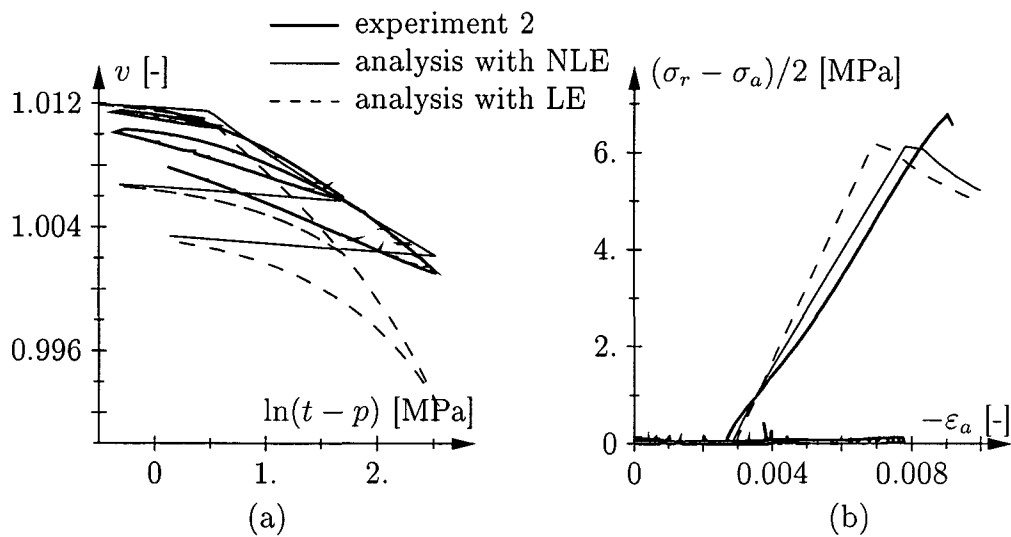

Figure 3.29: Determination of missing material parameters: (a) specific volume - hydrostatic pressure curves, (b) deviatoric stress - axial strain curves for experiment 2, obtained from the final set of parameters

final set of material parameters	
slope of the normal compression line, λ [-]	0.0040
slope of the unloading-reloading line, κ [-]	0.0005
initial size of the elastic domain, q_0 [MPa]	1.63
slope of the critical state line, M [-]	2.05
tensile strength, t [MPa]	0.50
initial specific volume, v_0 [-]	1.012
amount of coupling in elasticity, $\tilde{\alpha}$ [-]	800.0
compression modulus for linear elastic law, K [MPa]	1100.0
shear modulus for linear elastic law, G [MPa]	1500.0

Table 3.8: Determination of missing material parameters: Final set of material parameters used in the numerical simulations

The numerically obtained results shown in Figures 3.28 and 3.29 are in good agreement with the experimental results. The numerically obtained specific volume - hydrostatic pressure curves in Figures 3.28 and 3.29(a) show satisfactory agreement with the experimentally obtained curves for the nonlinear (NLE) model. Expectedly, for the linear (LE) analysis, degree of agreement is less satisfactory as regards the volumetric answer. However, the small deviations in the specific volume at high preconsolidation pressure result from the estimation of the slope of the unloading-reloading branch κ in the first part of the curves, i.e., at small preconsolidation pressures. As can be seen from the experimental curve of the clay marl, the slope of the unloading-reloading line increases with increasing preconsolidation pressure, which is not accounted for in the theory of the applied Cam-Clay model. Additionally, good agreement between the numerically obtained results and experimentally obtained results is achieved as regards the slope of the the deviatoric stress - axial strain relation for both analyses (see Figures 3.28 and 3.29(b)). However, the experimentally obtained shear resistance depicted in Figures (3.28)(b) and 3.29(b) can only be numerically reproduced with the high preconsolidation pressure from experiment 2.

The second numerical simulation refers to an unconfined uniaxial compression test (see Figure 3.30). It was used for the confirmation of the estimated material parameters. Here, the experimentally observed failure load reported in the experts' report could be reproduced: the numerically obtained uniaxial compressive strength, $\sigma_{cu} = 3.24$ MPa, corresponds to the range of observed uniaxial compressive strengths of 3 – 5 MPa and 2 – 4 MPa, respectively. Hence, this result confirms the evaluated material parameters.

3.4.2.2   Comments on the tested miocene marl

The Cam-Clay model has originally been developed for soft, compressible clays. Its application to layered, rock-like material requires some additional remarks:
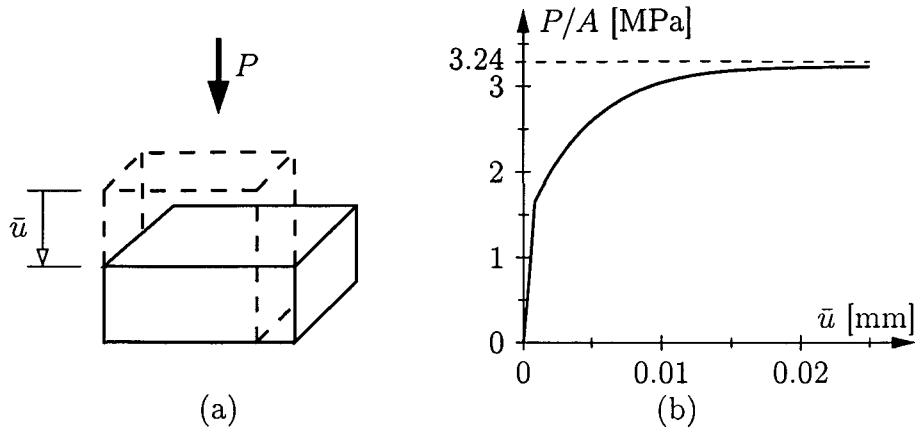
Figure 3.30: Numerical simulation of uniaxial compression test: (a) applied mode of deformation for unit cube (dimensions: $1 \cdot 1 \cdot 1$ mm^3, $\bar{u}$: prescribed displacement at top surface of finite element); and (b) $P/A - \bar{u}$ curve obtained from the final set of parameters

On the discrepancy between the experimentally determined Cam-Clay material parameters of the miocene clay marl and and the Cam-Clay material parameters estimated from soft clays from open literature. Generally, the values of λ and κ found in the open literature for the Cam-Clay model are significantly higher than the values estimated for the present clay marl. The first reason for this discrepancy lies in the kind of tested material. First, a rock-like material is tested which has much less elastic and elastoplastic compressibility than soft, compressible clays. Second, the range of hydrostatic pressures applied in the experiments of the miocene clay marl is one to two orders of magnitude higher than the range of hydrostatic pressures reported in the open literature for soft clays (see Figure 3.31). And third, the initial specific volume v_0 is estimated to be rather close to 1.0, where the slopes of λ and κ necessarily should be approximately zero. Hence, λ and κ have to decrease with increasing hydrostatic pressure, and the linear extrapolation depicted in Figure 3.31 does not hold for such high hydrostatic pressures.

Anisotropic behavior of clay material. In the performed hydrostatic compression tests, a strong degree of anisotropy of the deformation behavior under the application of an isotropic load was observed (see Figure 3.32 and Figure 3.23(c)). A close investigation of the present clay marl indicates a horizontal stratification of the material. Corresponding to this fine layering of the material, the experts' report on the soil characteristics recommends direction-dependent design-values for shear failure.

However, from a mechanical point of view, the elastic characteristics of the material primarily determine the initial deformational behavior in an experiment. Unfortunately, such elastic constants could not be determined for the compilation of the experts' report, because the application of strain gauges failed in unconfined uniaxial compression tests. Instead, one plate load test is mentioned for the undisturbed clay marl and two oedometric compres-
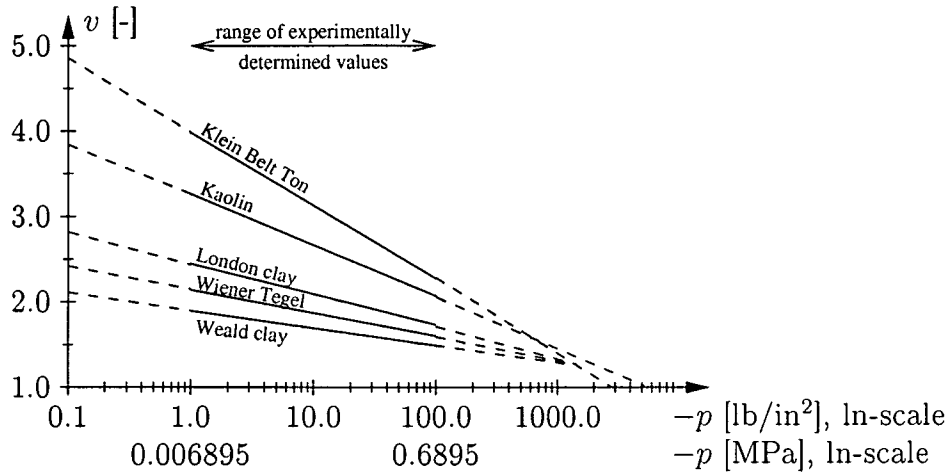
Figure 3.31: Family of experimentally determined critical state lines and their linear extrapolation as reported in [76]
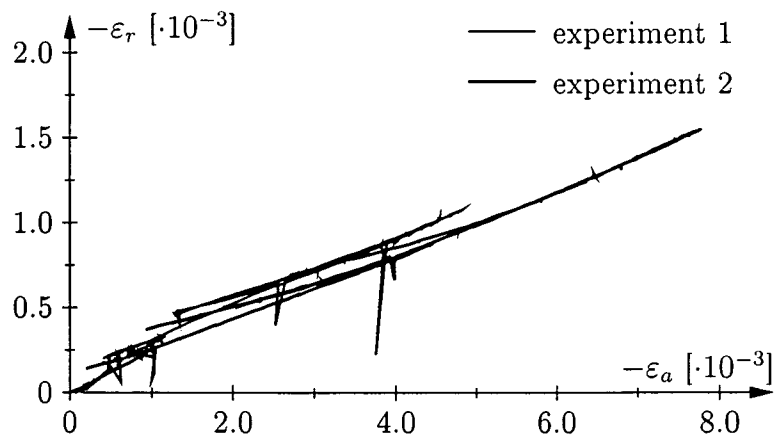

Figure 3.32: Observed anisotropy of strain path in hydrostatic compression test

sion tests with perpendicular directions of the layering are reported for the disturbed clay marl. Finally, it is recommended in the experts' report that the deformation/constrained modulus should be treated as direction-independent. Anyway, this recommendation seems to be based on oedometric compression experiments where the pressures that are usually applied are $4.0 \leq \sigma_v \leq 800(1600)$ [$\cdot 10^{-3}$ MPa] [54]. Similarly, the confinement applied in triaxial compression tests ranges between $50 \leq \sigma_c \leq 65$ [$\cdot 10^{-3}$ MPa], as is mentioned in the experts' report.

Unlike in this report, the confinement applied in the hydrostatic triaxial compression test in Graz was only $3 \leq \sigma_c \leq 10$ [$\cdot 10^{-3}$ MPa]. Thus, it was about one order of magnitude smaller than the triaxial compression tests referred to in the experts' report, and up to two orders of magnitude smaller than the pressures that are usually applied in oedometric compression. Therefore, it is most likely that the observed anisotropic deformation in the hydrostatic compression tests results from compression of the strata of the material in consequence of the low confinement.

Chapter 4

Numerical examples

The numerical examples presented in this Chapter are recomputations of experimental results obtained from small-scale laboratory experiments on tunnel failure. The aim of these tunnel failure experiments was to investigate the stability of the tunnel roof during excavation of a shallow tunnel.

These experiments are particularly suitable for the application of the material models proposed in Section 3.3, because for shallow driven tunnels, where the size of the protection zone is limited by the overburden height, the shear resistance of the material plays a fundamental role for the stability of the excavation. In cases where the shear resistance of the material is exceeded, failure zones are likely to develop at these locations of high shear strains. Usually, such zones of soil failure emanate at these highly-strained locations and propagate to the free surface and to the tunnel opening along shear bands. This may result in structural collapse of the tunnel.

The presented examples serve as validation of the material models described in Section 3.3. It is pointed out that no attempt will be made in the following examples to reproduce the experimentally obtained results by optimizing material parameters. Consequently, the arizing discrepancies between experimental and numerical results will be discussed and accepted as they are.

4.1 Tunnel excavation in artificial material

The Drucker-Prager material model proposed in Section 3.3.1 is applied to a laboratory experiment of a tunnel excavation. The aim of this experiment, which was conducted at the Rock Mechanics Laboratory of Kobe University in Japan [1], was to investigate the stability of the tunnel roof during excavation of a shallow tunnel. For this experiment, the use of the Drucker-Prager material model is considered as particularly suitable because it was developed for an artificial material, and is also applied here to an artificial material.
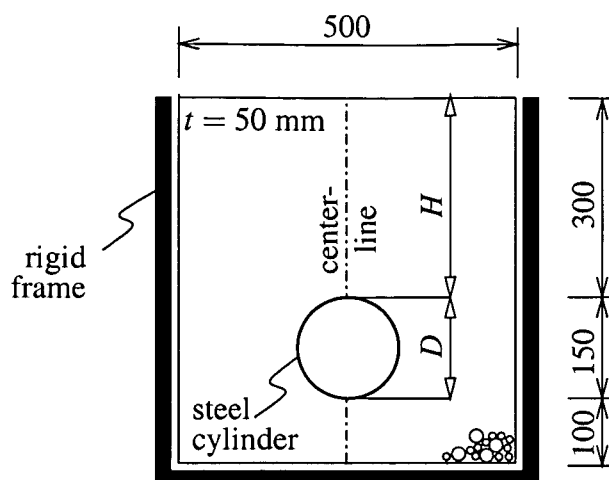
Figure 4.1: Laboratory experiment of a tunnel excavation: geometric dimensions (in [mm]) of the experimental setup [85]

4.1.1 Description of laboratory experiment

The experimental setup for the simulation of a tunnel excavation consists of a rigid frame (width·height·depth = 500 mm·550 mm·50 mm) and a hollow cylinder made of steel ($\emptyset$150 mm) located at the vertical centerline of the frame (see Figure 4.1). The overburden H of the considered experiment is 300 mm.

The material used in the experiment is artificial. It consists of an assembly of cylindrical aluminium bars representing frictional soil. Corresponding to the depth of the frame, the bars have a length of 50 mm. 85% of the bars have a diameter of 1.6 mm, the remaining 15% have a diameter of 3 mm. Refer to Table 3.1 for the material properties of the assembly of aluminium bars obtained from laboratory experiments reported in [85].

The experiment was conducted as follows:

1. First, the steel cylinder was placed as depicted in Figure 4.1.

2. Then, the material was deposited layerwise into the rigid frame. Each layer was compacted in order to obtain a uniform density of $\rho = 0.219 \cdot 10^{-4}$ kg/mm^3.

3. Four airbags, placed inside the steel cylinder, were filled with air until an internal pressure equal to the vertical stress at the tunnel crown was reached. The vertical stress at the tunnel crown was given by $\gamma \cdot H$, where γ is the dead load of the material.

4. The cylinder was removed.

5. Thereafter, the internal pressure in the airbags was reduced, simulating the excavation of the tunnel.

During the experiment, the collapse of the tunnel was characterized by sudden deformations of the tunnel surface reaching the order of few millimeters.
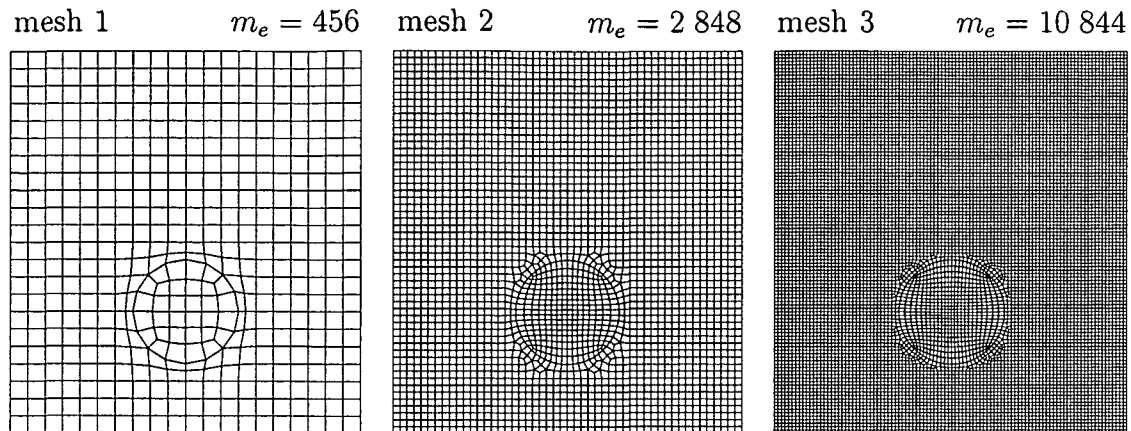
Figure 4.2: Simulation of tunnel excavation: FE meshes (m_e: number of elements)

4.1.2 Application to tunnel excavation

For the simulation of the aluminium bar assembly, the multi-surface plasticity model is employed. Hereby, the parameters given in Tables 3.1, 3.2, and 3.6 are used. The FE meshes used for the simulation are shown in Figure 4.2. As in Section 3.3.2, plane strain conditions are considered. The meshes are characterized by a decreasing element size ranging from $\ell_c = 25$ mm (mesh 1) over $\ell_c = 10$ mm (mesh 2) to $\ell_c = 5$ mm (mesh 3). The inital stress state consists of

- a vertical stress $\sigma_v = \gamma(y_0 - y)$, where γ is the dead load of the material ($\gamma = 0.219 \cdot 10^{-4}$ N/mm^3) and y_0 is the value of the vertical coordinate y of the surface.

- a horizontal stress σ_h given as $\sigma_h = K_0 \cdot \sigma_v$, where $K_0 = 1 - \sin(\varphi_p)$, with φ_p as the peak friction angle as given in Table 3.2.

At integration points at which the Drucker-Prager criterion is violated by the initial stress state, i.e., for $f_{DP}(\sigma_h, \sigma_v, \alpha_{DP} = 0) > 0$, the internal variable is adjusted such that $f_{DP}(\sigma_h, \sigma_v, \alpha_{DP} > 0) = 0$. The initial out-of-plane stress assumed here is obtained from Hooke's law under the assumption of plane strain (see also [85] and Section 3.3.2). This initial stress state leads to the initialization of the internal variable such that $\alpha_{DP} = \alpha_{DP,m}$ at every integration point.

The excavation is controlled by the previously described airbags. Their initial pressure, p_0, is set equal to the vertical stress in consequence of dead load acting on the tunnel roof, giving

$$p_0 = p(t = 0) = \gamma \cdot H = 0.219 \cdot 10^{-4} \cdot 300 \approx 0.66 \cdot 10^{-2} \text{ MPa} .\tag{4.1}$$

In the course of the simulation, the pressure in the airbags, p, is continuously reduced until the incremental-iterative solution procedure fails to converge or until the air pressure in the
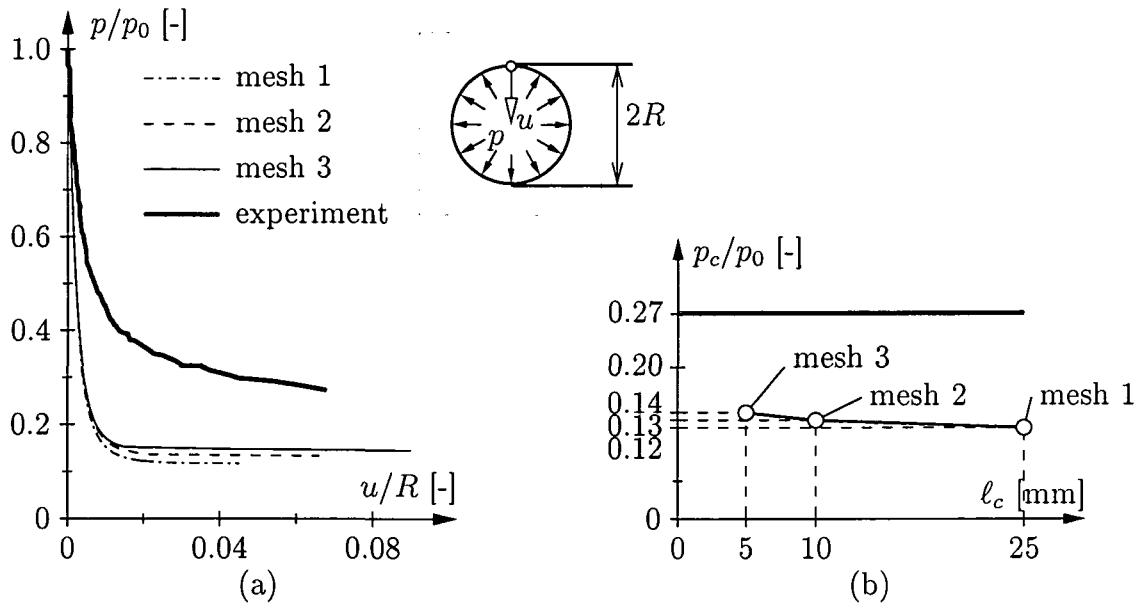
Figure 4.3: Simulation of tunnel excavation: (a) $p/p_0 - u/R$ curves and (b) normalized pressure at collapse p_c/p_0

airbag has decreased to zero. Collapse of the tunnel is assumed either when the incremental-iterative solution procedure fails to converge, or a band of elements characterized by failure of the material connecting the excavation and the surface is completed. Here, failure of the material is defined by a negative minimum eigenvalue μ^p_{min} of the acoustic tensor Q^p_{jl} (see Section 3.3.2). This value is computed for each integration point.

Figure 4.3 shows the normalized vertical displacement at the tunnel crown, u/R, as a function of the normalized pressure in the airbags, p/p_0. It is seen that the numerically obtained normalized pressure at collapse, p_c/p_0, approaches the experimentally obtained value (see Figure 4.3(b)).

However, the normalized collapse pressure obtained from the finest mesh ($p_c/p_0 = 0.19$) is still significantly lower than the respective experimental result ($p_c/p_0 = 0.27$). Deviations between numerically and experimentally obtained results are already observed at low values of p/p_0. The reason for the observed deviations is in the underlying assumption of isotropic material behavior. For the considered aluminium bar assembly, this assumption provides only an approximation to the actual transverse isotropic behavior characterized by different material responses in consequence of in-plane and out-of-plane deformations.

The distribution of the internal strain-like variable α_{DP} obtained from the analysis based on mesh 2 is depicted in Figure 4.4. It refers to loading states of $p/p_0 = 0.14$ and $p/p_0 = 0.13$, i.e., slightly before and when collapse of the tunnel is indicated by the analysis. Because of the initial stress state, requiring $\alpha_{DP} = \alpha_{DP,m}$ everywhere in the structure, only material softening is observed. This softening is most pronounced at the two sides of the tunnel. Additionally, two narrow bands of softened material directing to the surface, can be identified. The distribution of α_{DP}, however, does not indicate the collapse of the

α_{DP} [10^{-2}]

- 7.047
- 6.547
- 6.047
- 5.547
- 5.047
- 4.547= $\alpha_{DP,m}$

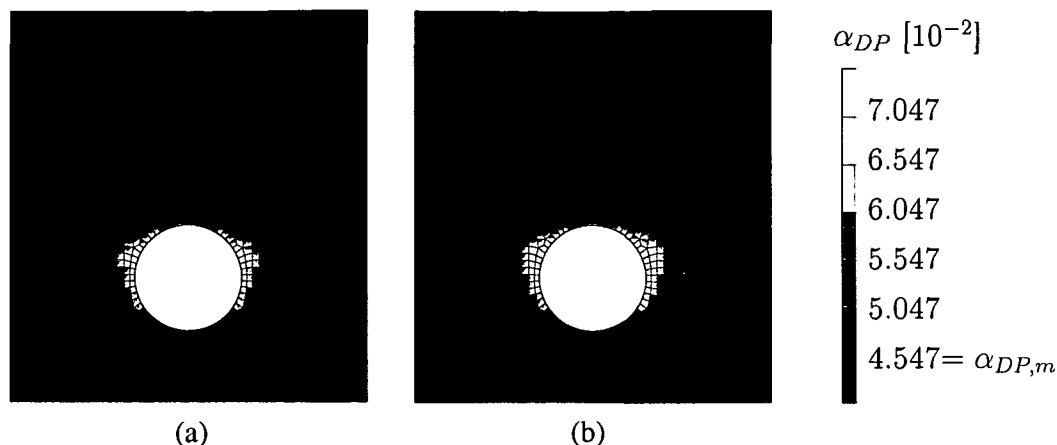(a)   (b)

Figure 4.4: Simulation of tunnel excavation: distribution of strain-like internal variable α_{DP} obtained from analysis based on mesh 2, slightly before and at collapse, i.e., at (a) $p/p_0 = 0.14$ and (b) $p/p_0 = 0.13$

tunnel.

An appropriate indicator for tunnel collapse is the minimum eigenvalue of the acoustic tensor, μ^p_{min}. This value is computed for each integration point. The distribution of the normalized minimum eigenvalue, μ^p_{min}/μ^e, with μ^e representing the eigenvalue of the acoustic tensor computed from $Q^e_{jl} = C^e_{ijkl}n_i n_k$ ($\mathbf{C}^e$: elastic material tensor), is shown in Figures 4.5(a) and 4.6(a). The two plots refer to loading states of $p/p_0 = 0.14$ and 0.13. The reduction of the normalized pressure p/p_0 from 0.14 to 0.13 resulted in the extension of shear planes to the surface. The shear planes are characterized by a negative value of the normalized minimum eigenvalue, i.e., by $\mu^p_{min}/\mu^e < 0$. The corresponding direction of the shear band is given by $\vartheta + \pi/2$ (see Figures 4.5(b) and 4.6(b)). The direction of the shear band indicates shear failure starting from the tunnel springlines extending towards the surface. At $p/p_0 = 0.14$ (Figure 4.5(b)), however, the respective failure line is not closed. In some areas, the direction of the shear bands is still deviating from the final direction of failure, i.e., $80° \le \vartheta + \pi/2 \le 90°$ for the right and $90° \le \vartheta + \pi/2 \le 100°$ for the left shear failure zone. At $p/p_0 = 0.13$ (Figure 4.6(b)), the aforementioned gaps in the shear failure zone are closed indicating the collapse of the tunnel. It is observed that the shear failure planes develop in a rather straight line upwards, as would be expected for a cohesionless material and as was experimentally confirmed for the assembly of aluminium bars.

4.2   Tunnel excavation in granular material

The Mohr-Coulomb material model proposed in Section 3.3.1 is applied to a laboratory experiment of a tunnel excavation. The aim of this experiment, which was conducted at the Institute for Soil and Rock Mechanics of University of Karlsruhe [59], Germany, was

(a)

(b)

Figure 4.5: Simulation of tunnel excavation: distribution of (a) normalized minimum eigenvalue of the acoustic tensor, μ^p_{min}/μ^e, and (b) corresponding direction of shear planes, given by $\vartheta + \pi/2$, obtained from the analysis based on mesh 2 right before collapse, i.e., at $p/p_0 = 0.14$
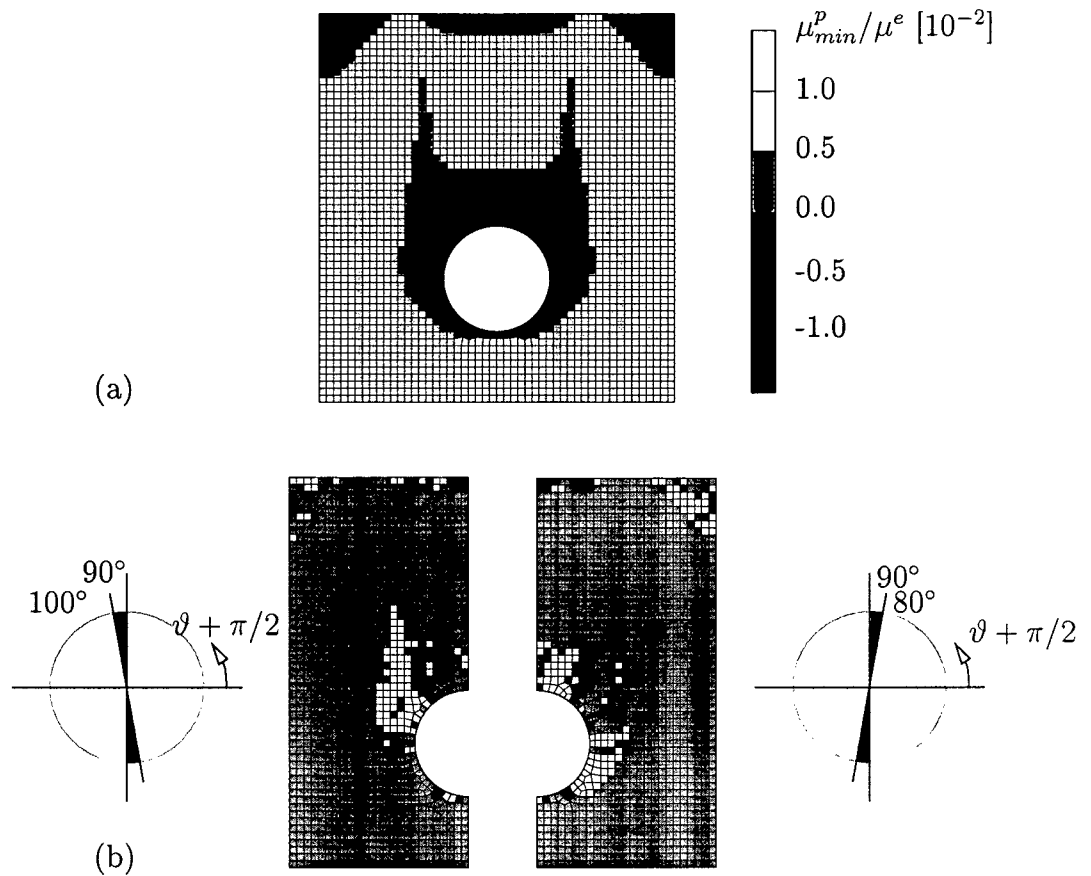
(a)

(b)

Figure 4.6: Simulation of tunnel excavation: distribution of (a) normalized minimum eigenvalue of the acoustic tensor, μ^p_{min}/μ^e, and (b) corresponding direction of shear planes, given by $\vartheta + \pi/2$, obtained from the analysis based on mesh 2 at collapse, i.e., at $p/p_0 = 0.13$
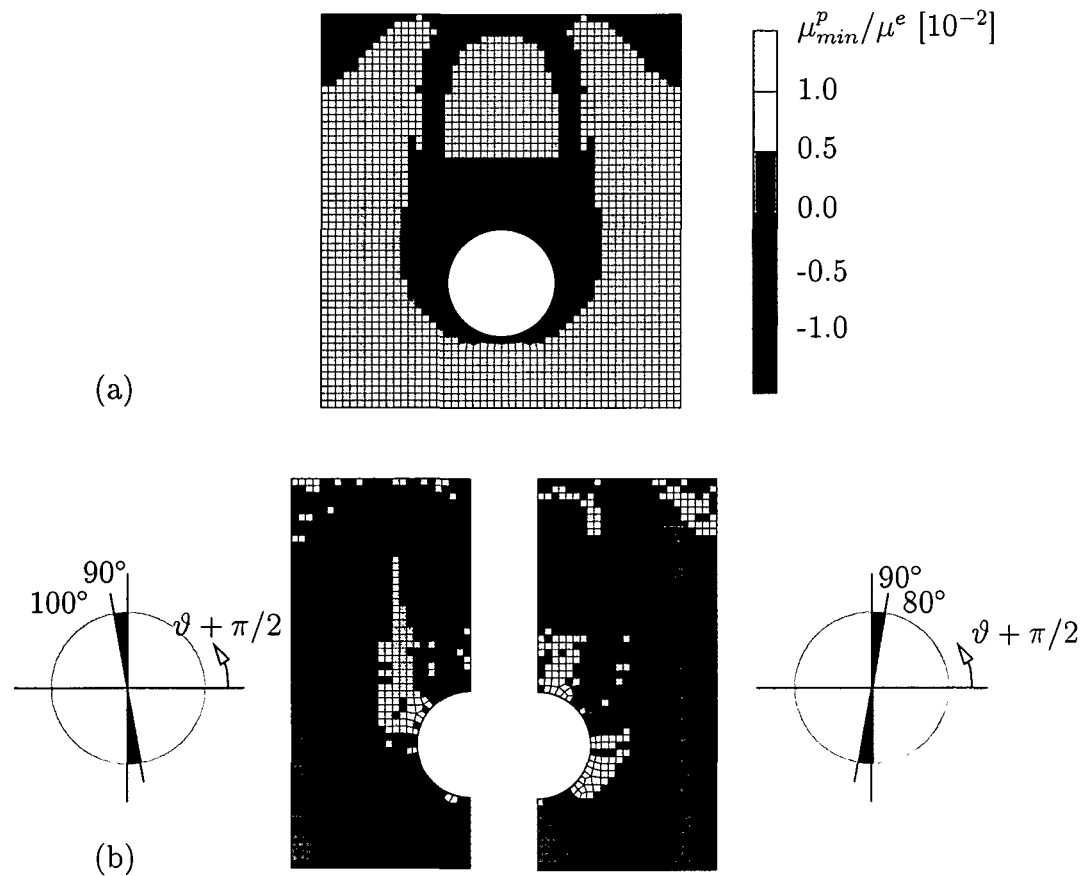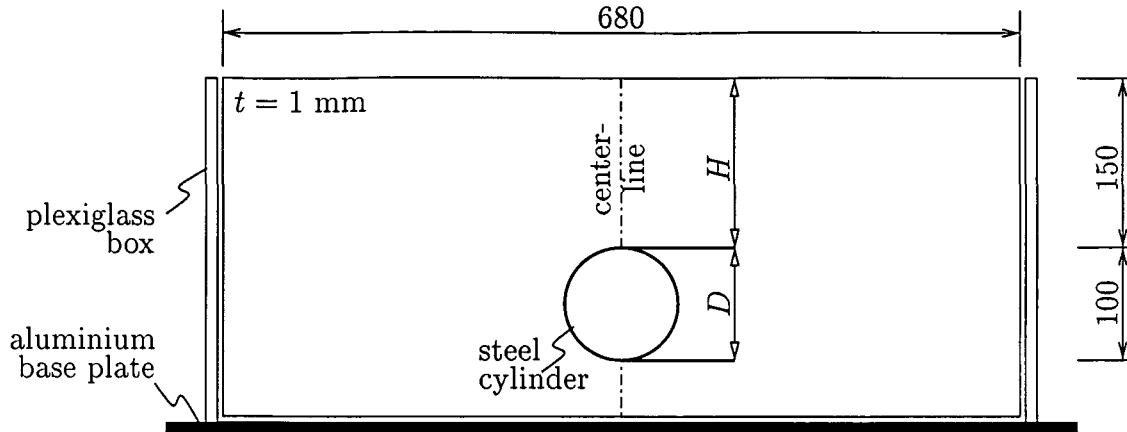
Figure 4.7: Laboratory experiment of a tunnel excavation: geometric dimensions (in [mm]) of the experimental setup [59]

to investigate the stability of the tunnel roof during excavation of a shallow tunnel.

For this experiment, the Mohr-Coulomb model, developed for natural soils, is considered as particularly suitable and, hence, chosen, as the material used in the experiment consisted mainly of sand, a natural and granular soil.

4.2.1 Description of laboratory experiment

The experimental setup for the simulation of a tunnel excavation consists of an aluminium base plate, on which a plexiglass box of 3 cm thickness (width·depth = 680 mm·560 mm) is mounted. A rigid frame attached to the aluminium base plate supports the plexiglass box. A hollow steel cylinder (ϕ100 mm) is located at the vertical centerline of the box (see Figure 4.7). The overburden H of the considered experiment is 150 mm.

The material used in the experiment is described in Section 3.3.3. and in [59]. It consists of a silica sand and a 1% clay fraction. The entire mixture has a water content of 1,2%. Table 4.1 contains failure properties of the used mixture obtained from torsional direct shear tests reported in [59].

material parameters of the sand mixture	
unit weight, γ [N/mm^3]	$14.16 \cdot 10^{-6}$
friction angle, φ [°]	29.0
cohesion, c [MPa]	$0.55 \cdot 10^{-3}$

Table 4.1: Laboratory experiment of a tunnel excavation: material parameters of the sand mixture from torsional direct shear tests valid for vertical confinement in the range of $\sigma_v \in (0.000, 0.006)$ [MPa] [59]

The chosen experiment was conducted as described in the following:

1. First, the material is deposited layerwise into the plexiglass box. Each layer is compacted with a constant surface load of $\sigma_v = 1.0 \cdot 10^{-3}$ MPa in order to obtain a uniform density. The resulting unit weight of the mixture was measured as $\gamma = 14.16 \cdot 10^{-6}$ MPa.

2. Then, the steel cylinder is pressed piecewise into the soil and the soil material is removed from inside the cylinder with a cutting edge device until the cylinder has reached the far side of the plexiglass box.

3. An airbag, placed inside the steel cylinder, is filled with air until an internal pressure which is equal to the vertical stress at the tunnel crown, is reached. The vertical stress at the tunnel crown is given by $\gamma \cdot H$, where γ is the bulk unit weight of the material.

4. The steel cylinder is removed.

5. Thereafter, the internal pressure in the airbag is reduced, simulating the excavation of the tunnel.

During the experiment, collapse of the tunnel was characterized by a sudden increase of the pressure in the airbag, indicating that lumped soil fell from the tunnel roof onto the airbag. After collapse of the tunnel, the plexiglass box was flooded to increase the material stability. Because of the increased artificial cohesion, the box could be opened and the soil block could be cut to make the shear failure zones visible.

4.2.2 Simulation of tunnel excavation

The Mohr-Coulomb material model proposed in Section 3.3.1 is applied to the simulation of the tunnel excavation experiment as described in Section 4.2.1. For the simulation of the sand mixture, the multi-surface plasticity model consisting of the Mohr-Coulomb failure envelope and the tension-cut-off criterion is employed. Hereby, the parameters given in Table 4.2 are used. The choice of the listed parameters is based on the following argumentation: the Mohr-Coulomb failure parameter φ_p and the unit weight γ are taken from [59] (see Table 4.1), as they are derived from laboratory experiments and from measurement of the original material used in the tunnel failure experiment. The cohesion c is modified from the value given in Table 4.1, as the results from the torsional direct shear test reveal a strong dependence of the cohesion on the confining pressure especially at low stress levels. It is reported in [59], that the cohesion c estimated for high confinement was observed to decrease for lower confinement intervals up to $c_{low\,stress\,level} = 0.20 c_{high\,stress\,level}$ in single cases. Therefore, the cohesion is assumed to be 40% of the given value, as the stress level in the considered tunnel excavation experiment is expected to be less than 0.004 MPa. However, there was also an increase of the friction angle observed for decreasing confining pressure, but this increase was found to be about 1° for all experiments. Therefore, a modification of the peak friction angle is not considered here.

material parameters of the sand mixture	
bulk unit weight, γ [N/mm^3]	$14.16 \cdot 10^{-6}$
Young's modulus, E [MPa]	42.5
Poisson's ratio, ν [–]	0.42
initial friction angle, φ_i [°]	0.0
peak friction angle, φ_p [°]	29.0
residual friction angle, φ_r [°]	28.8
cohesion, c [MPa]	$0.22 \cdot 10^{-3}$
peak dilatancy angle, ψ_p [°]	4.0
softening material parameter, G_f [mm]	$1.0 \cdot 10^{-2}$
internal variable α_{MC} at $\varphi = \varphi_p$, $\alpha_{MC,m}$ [–]	0.03

Table 4.2: Numerical simulation of a tunnel excavation: material parameters used for the sand mixture
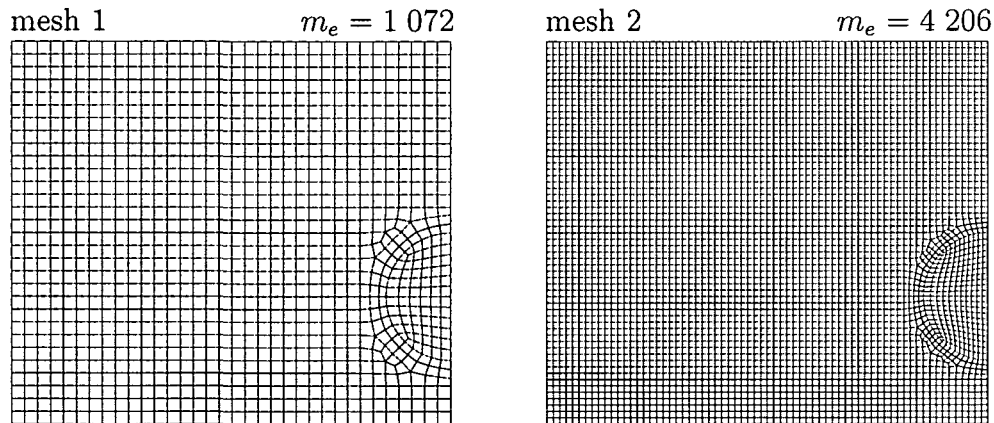

Figure 4.8: Simulation of tunnel excavation: FE meshes (m_e: number of elements)

The elastic parameters E, ν and the Mohr-Coulomb hardening/softening parameters G_f, $\alpha_{MC,m}$ as well as the dilatancy parameter ψ_p are taken from the triaxial compession test of the remixed material as described in Section 3.3.3. The residual friction angle φ_r is chosen according to the peak friction angle, such that only marginal softening is observed. The remaining parameter, the initial friction angle, φ_i was chosen such that the initial state was already elastoplastic. The reason for this choice is that the layerwise consolidation of the material filled in the plexiglass box was undertaken to obtain permanent, i. e., plastic densification. Because of lack of experimental evidence, φ_i was chosen to be $\varphi_i = 0°$. This choice resulted in a plastic response located in the hardening regime after application of the initial stress state.

The FE meshes used for the simulation are shown in Figure 4.8. For symmetry reasons, only half of the cross-section is discretized. Plane strain conditions are considered for the

simulation of a cross-section of the experimental setup, as boundary and loading conditions are uniform over the length of the plexiglass box, which is 5.6 times the tunnel diameter. The meshes are characterized by a decreasing element size ranging from $\ell_c = 10$ mm (mesh 1) to $\ell_c = 5$ mm (mesh 2). The inital stress state consists of

- a vertical stress $\sigma_v = \gamma(y_0 - y)$, where γ is the dead load of the material ($\gamma = 0.1416 \cdot 10^{-4}$ N/mm^3) and y_0 is the value of the vertical coordinate y for the surface.

- a horizontal stress σ_h given as $\sigma_h = K_0 \cdot \sigma_v$, where $K_0 = 1 - \sin(\varphi_p)$, with φ_p as the peak friction angle as given in Table 4.2.

Like in the previous example, this initial stress state results in a violation of the Mohr-Coulomb criterion at all integration points, i.e., $f_{MC}(\sigma_h, \sigma_v, \alpha_{MC} = 0) > 0$. Hence, the internal variable is adapted such that $f_{MC}(\sigma_h, \sigma_v, \alpha_{MC} > 0) = 0$.

The excavation is controlled by the earlier described airbag. Its initial pressure, p_0, is set equal to the vertical stress in consequence of dead load acting on the tunnel roof, giving

$$p_0 = p(t = 0) = \gamma \cdot H = 0.1416 \cdot 10^{-4} \cdot 150 \approx 0.2124 \cdot 10^{-2} \text{ MPa} . \qquad (4.2)$$

In the course of the simulation, the pressure in the airbag, p, is continuously reduced until the incremental-iterative solution procedure fails to converge. At this stage of loading, collapse of the tunnel is assumed.

Figure 4.9 shows the normalized vertical displacement at the tunnel crown, u/R, as a function of the normalized pressure in the airbag, p/p_0. It is seen that the numerically obtained normalized pressure at collapse, p_c/p_0, approaches the experimentally obtained value (see Figure 4.9(b)).

However, some difference between the numerically and the experimentally obtained normalized collapse pressure is observed. One reason for the deviation from the experimentally obtained normalized collapse pressure is the lack of material parameters from the original material used in the experiment.[1]

The distribution of the internal strain-like variable α_{MC} obtained from the analysis based on the two meshes is depicted in Figure 4.10. It refers to a loading state of $p/p_0 = 0.04$ for mesh 1 and $p/p_0 = 0.08$ for mesh 2, respectively, i.e., when collapse of the tunnel is indicated by the analysis. Most of the area characterized by plastic material response, i.e., $\alpha_{MC} > 0$, is still in the hardening regime characterized by $\alpha_{MC} < \alpha_{MC,m}$. Peak values of α_{MC} are observed at the tunnel springlines. In this area the material has already entered the softening regime with $\alpha_{MC} > \alpha_{MC,m}$. However, it is worth noting that a rather wide band of increased values of the strain-like internal variable α_{MC} evolves from the tunnel springlines and develops in a curved manner directing to the surface. This indicates that the structural failure mode is somewhat indistinct.

---

[1]As can be seen from comparison of Table 3.3 with Table 3.4, the remixing of the original material using similar sand and clay yields quite different results.
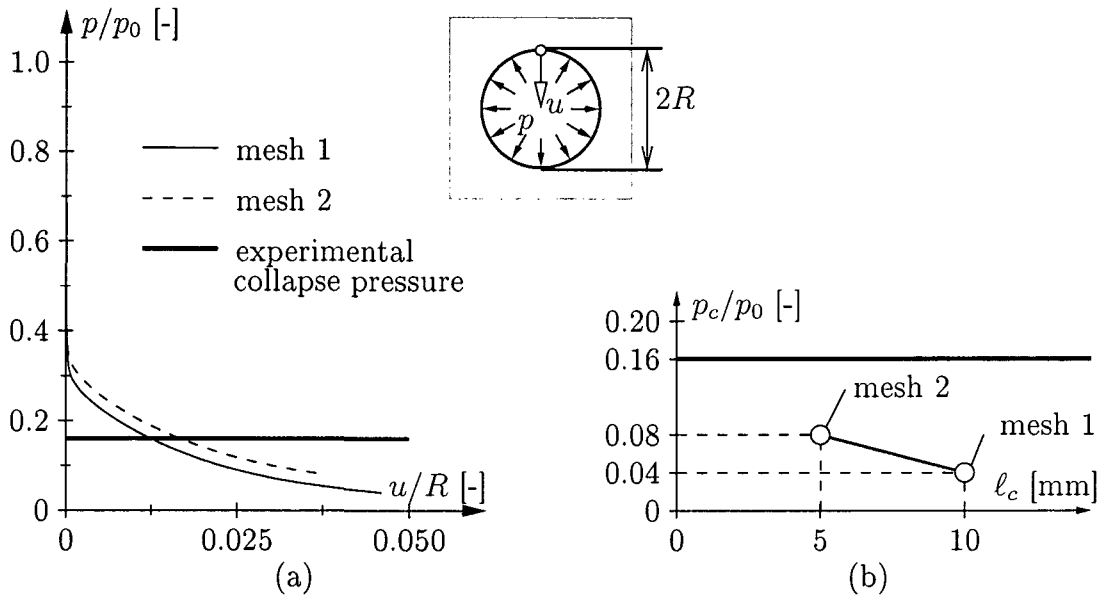
Figure 4.9: Simulation of tunnel excavation: (a) $p/p_0 - u/R$ curves and (b) normalized pressure at collapse p_c/p_0

Figure 4.10: Simulation of tunnel excavation: distribution of strain-like internal variable α_{MC} obtained from analysis based on the two meshes, at collapse, i.e., at $p/p_0 = 0.04$ for mesh 1, respectively at $p/p_0 = 0.08$ for mesh 2
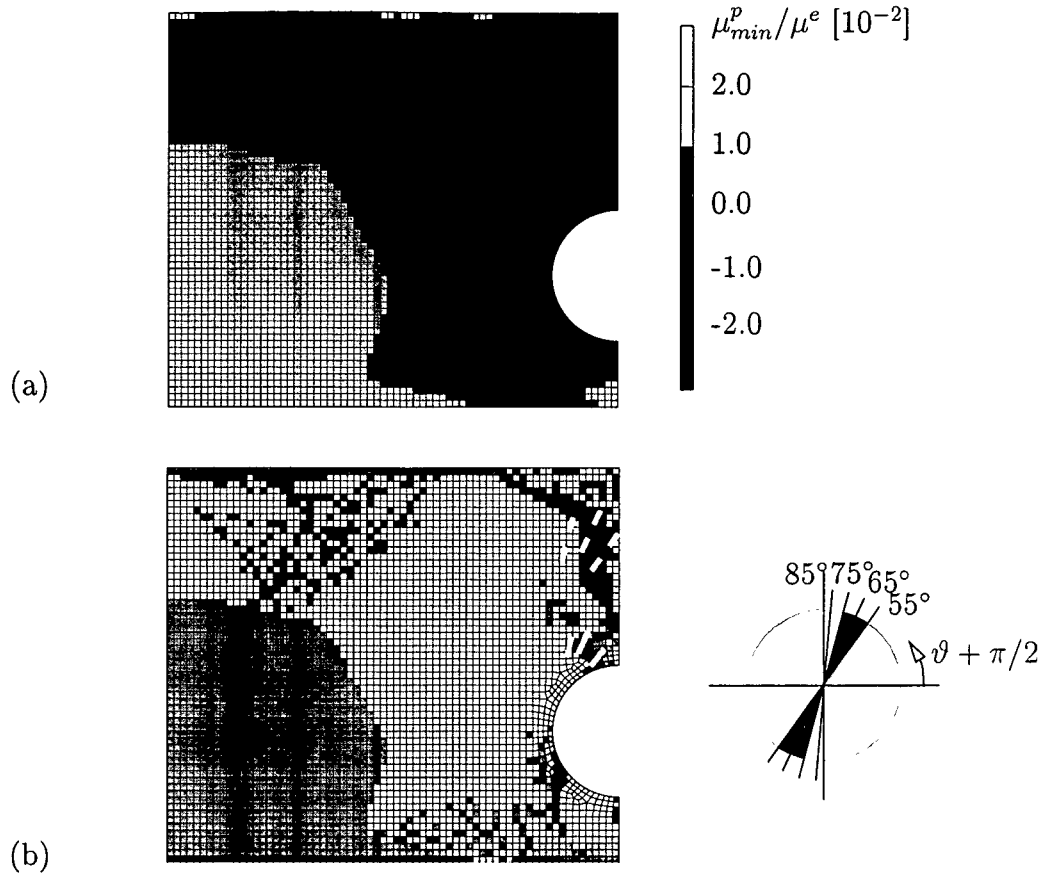
Figure 4.11: Simulation of tunnel excavation: Distribution of (a) normalized minimum eigenvalue of the acoustic tensor, μ^p_{min}/μ^e, and (b) corresponding directions of shear planes, given by $\vartheta + \pi/2$, obtained from the analysis based on mesh 2 at collapse, i. e., at $p/p_0 = 0.08$

The failure mode is again revealed by the analysis from the acoustic tensor. First, the distribution of the minimum eigenvalue of the acoustic tensor reveals that the majority of the material surrounding the tunnel has already failed. Hence, for the case of a material with moderate cohesion, a large area of soil surrounding the tunnel is in a failed state. Consequently, from the distribution of the minimum eigenvalue of the acoustic tensor, no conclusion can be drawn concerning the failure mode, apart from the suggestion of a somewhat diffuse failure. However, the angles of the failure planes indicate failure at the tunnel roof, where several adjacent shear planes have developed in the course of the internal pressure reduction (see Figure 4.11). This observation agrees well with the observation made in the experiment where adjoined shear planes initiating from the tunnel directing to the surface are obtained (see Figure 4.12). In Figure 4.11, it can be observed that the adjoined shear failure planes start from near the tunnel springlines, develop in a curved fashion, and would meet a corresponding shear failure plane somewhere above the tunnel roof. This observation corresponds well with the experimental result depicted in Figure 4.12, where
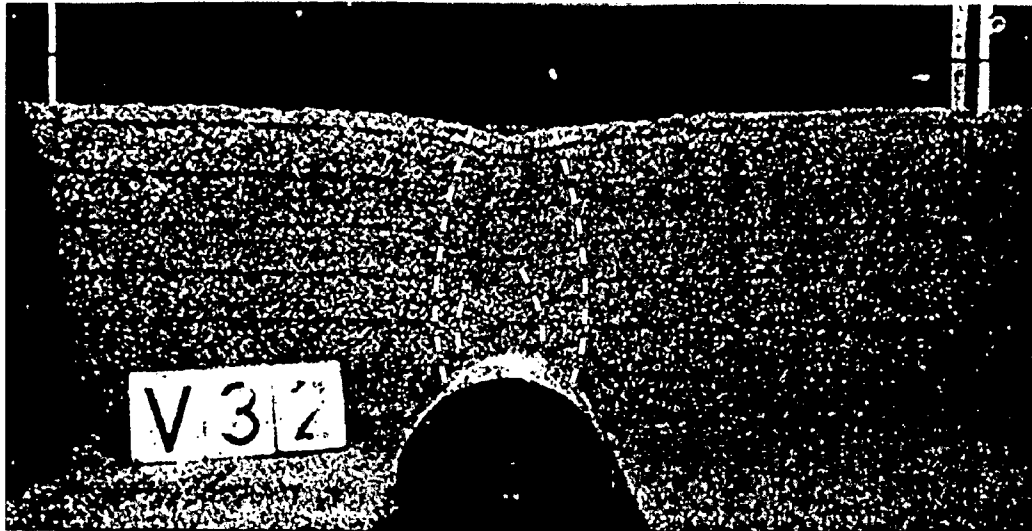
Figure 4.12: Simulation of tunnel excavation: Final deformation pattern after the end of the experiment and after laying open of the cross-section

also the presence of nested shear planes was observed after the opening of the tunnel cross-section. Hence, both the numerical and the experimental result corroborate the theory of nested protection zones developing around an excavation in a cohesive material.

Additionally, a parameter sensitivity study gives some insight into the structural influence of some single material parameters for the collapse simulations: the result of the simulations is depicted in Figure 4.13. The depicted curves indicate clearly that the most relevant parameters for the structural deformation behavior and for the occurrence of collapse are the classical Mohr-Coulomb failure parameters c and φ_p. Hence, the accurate determination of these two parameters is essential for the structural response in a numerical simulation.
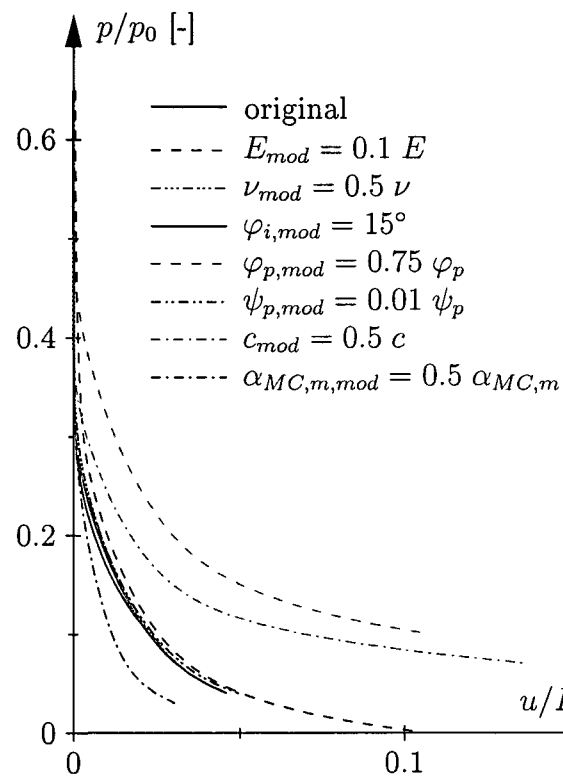
Figure 4.13: Simulation of tunnel excavation: Sensitivity of material parameters on the structural response: $p/p_0 - u/R$ curves

Chapter 5

Application of material models

5.1 Performance of jet grouting in granular and cohesive material

The driving of tunnels often requires pre-excavation means for improving the stability of the surrounding soil. Additionally, concerning tunneling in urban areas with low overburden, the reduction of settlements in order to avoid damage of buildings and infrastructure is also frequently the reason for ground improvement prior to excavation. One of several methods for achieving an increase of the load-carrying capacity of the surrounding soil formation is horizontal jet grouting (HJG). This method uses horizontal cement injections into the soil, ahead of the tunnel face, in order to obtain a cone-shaped support ring consisting of cemented soil in front of the tunnel face. Applications of HJG are reported in [31, 24, 56, 26, 96].

However, the performance and efficiency of the application of HJG in different geological conditions is essential for its economic applicability. In order to increase the insight into the structural behavior of ground-support interaction, sophisticated material models for jet grouted soil mass and shotcrete are employed together with the material models for soil proposed in Chapter 3 in the context of plane strain FE analysis. Similar analyses for only granular material focussing on the effect of HJG on the surface settlements have already been reported in [70, 11, 69].

For the present analyses, the process of ground improvement, the excavation of the tunnel, and the installation of the shotcrete lining are considered. The obtained results provide insight into the different load-carrying behavior of the compound structure consisting of jet grouted soil mass, the shotcrete lining, and the surrounding soil consisting of granular, respectively cohesive soil.

The performance of HJG for different soil conditions is shown by comparison of the settlements obtained from numerical analyses considering HJG with numerical analyses without consideration of HJG. Hence, the efficiency of HJG depending on the apparent ground conditions can be estimated.

5.1.1 Thermochemomechanical approach

A strong interaction of the hardening/creeping shotcrete shell and the viscous soil, which exerts pressure on the lining, can be observed in NATM tunneling. The creep properties of the shotcrete are the source of the deformations required for the activation of load-carrying capacity of the surrounding soil formation. Both the jet grouted support ring and the shotcrete lining are loaded during the hydration process.

In order to account for this chemomechanical coupling as well as for the change of temperature in consequence of hydration, a thermochemomechanical approach [90] was chosen in [70] for the description of jet grouted soil and shotcrete. This approach is used in this work in form of simplified isothermal chemomechanical analysis. Such simplified analysis is justified by the findings in [35], where the structural influence of the temperature on the axial forces in the lining was found to be rather small.

A short summary of the models is contained in the following sections. For a more detailed description, the reader is referred to [35, 70].

5.1.1.1 Material model for shotcrete

A thermochemomechanical material model for shotcrete has been developed at Vienna University of Technology [38] and continuously improved as regards the description of creep [77, 36] and of microcracking [49]. In this material model, dissipative phenomena at the microlevel of the material are accounted for by means of (internal) state variables and energetically conjugate thermodynamic forces related to the state variables via state equations. The rates of the internal state variables are related to the conjugate thermodynamic forces by means of evolution equations.

As is typical for cement-based materials, four dissipative phenomena govern the material behavior:

1. Hydration, resulting in chemical shrinkage strains, aging elasticity, and strength growth. The extent of the chemical reaction, i. e., of the hydration process, is described by the degree of hydration ξ, with $0 \leq \xi \leq 1$.

2. Microcracking of hydrates which are the result of the hydration process yields plastic strains ε^p. The state of microstructural changes resulting from microcracking is described by hardening variables χ.

3. Stress-induced dislocation-like processes within the hydrates result in flow (or long-term) creep strains ε^f [97]. The state of respective microstructural changes is described by the viscous flow γ [88].

4. Stress-induced microdiffusion of water in the capillary pores between the hydrates result in viscous (or short-term) creep strains ε^v [74, 97, 88].

Table 5.1 contains the underlying field equations and constitutive relations of the developed material model. So-called intrinsic material functions, i. e., functions which do not depend on field or boundary conditions, serve as input for the material model. Intrinsic material functions for shotcrete have been computed from slightly extended standard laboratory tests (see, e.g., [38, 77]). It is pointed out here that such intrinsic functions need to be determined for each shotcrete mixture, as they depend on the properties of the used constituents and their ratios.

5.1.1.2 Material model for jet grouted soil mass

Similar to the thermochemomechanical model for shotcrete, a thermochemomechanical model for cemented soil, such as jet grouted soil mass, has been developed at Vienna University of Technology [70]. Just like for the material model for shotcrete, intrinsic material functions describing the

1. hydration kinetics,

2. evolution of strength and stiffness,

3. short-term creep behavior, and

4. long-term creep behavior,

need to be determined. Here, hydration kinetics are described by means of adiabatic test results on cement CEM I 32.5 with 485 kg cement/(m^3 mortar) reported in [15]. This cement is commonly used in jet grouting applications.

As regards the evolution of strength and stiffness, an experimental program was initiated at the Institute for Strength of Materials at Vienna University of Technology. In the framework of this program, the evolution of strength and stiffness was evaluated for soilcrete in granular soil. The respective results are contained in [10].

As data on the experimental investigation of creep of soilcrete are not reported in the open literature, the creep characteristics were determined by means of the B3-model described in [3].

Table 5.1 summarizes the underlying field equations and constitutive relations of the developed material model for soilcrete. Like in the material model for shotcrete, intrinsic material functions serve as input. It is pointed out here again that these intrinsic functions need to be determined for each considered soilcrete, as they depend on the properties of the used constituents and their ratios.

FIELD EQUATIONS
first law of thermodynamics (see e. g.[89]): $\quad (\rho c)\dot{T} - \ell_\xi\dot{\xi} = -\mathrm{div}\mathbf{q}$
equilibrium condition: $\qquad\qquad\qquad\qquad\qquad \mathrm{div}\boldsymbol{\sigma} + \mathbf{k} = \mathbf{0}$

CONSTITUTIVE EQUATIONS
heat conduction: Fourier's law $\qquad\qquad\qquad \mathbf{q} = -k\mathrm{grad}T$
incremental stress-strain law [77]: $d\boldsymbol{\sigma} = \mathbf{C}(\xi) : (d\boldsymbol{\varepsilon} - d\boldsymbol{\varepsilon}^p - d\boldsymbol{\varepsilon}^f - \alpha_T \mathbf{1}dT - \beta\,(\xi)\,\mathbf{1}d\xi - d\boldsymbol{\varepsilon}^v)$
hydration kinetics [90]: Arrhenius' law $\qquad \dot{\xi} = \tilde{A}(\xi)\exp\left[-\frac{E_a}{RT}\right]$
microcracking [37, 49]: multisurface chemoplasticity   admissible stress space: $\quad \boldsymbol{\sigma} \in C_E \Leftrightarrow f_\alpha \leq 0 \quad \forall \quad \alpha \in [DP, R1, R2, R3]$ loading surfaces: $\qquad\quad f_{DP} = \sqrt{J_2} + \alpha I_1 - \zeta_{DP}(\chi_{DP},\xi)/\beta = 0$ $\qquad\qquad\qquad\qquad\quad f_{RA} = \sigma_A - \zeta_R(\xi) = 0, \quad A = 1,2,3$ evolution equations: $\quad \dot{\boldsymbol{\varepsilon}}^p = \sum_{\alpha \in J_{act}} \dot{\gamma}_\alpha \partial_{\boldsymbol{\sigma}} f_\alpha, \quad \dot{\chi}_{DP} = \dot{\gamma}_{DP}\partial_{\zeta_{DP}} f_{DP}$ Kuhn-Tucker conditions: $\quad f_\alpha \leq 0, \quad \dot{\gamma}_\alpha \geq 0, \quad f_\alpha\dot{\gamma}_\alpha = 0$
short-term creep [36]: aging viscoelastic law $\dot{\boldsymbol{\varepsilon}}^v(t) = \frac{1}{\tau_w[\xi(t)]}\left[\int_{t'=0}^t J_\infty^v[\xi(t')]\mathbf{G} : d\boldsymbol{\sigma}(t') - \boldsymbol{\varepsilon}^v(t)\right] \quad$ with $\quad \mathbf{G} = \mathbf{C}^{-1}E$
long-term creep [5, 88, 77]:   creep flow rule $\qquad\qquad\qquad\qquad \dot{\boldsymbol{\varepsilon}}^f = \frac{1}{\eta_f}\mathbf{G} : \boldsymbol{\sigma}$ flow creep viscosity $\qquad\qquad\quad \frac{1}{\eta_f} = cS\exp\left[-\frac{2U}{R}\left(\frac{1}{T} - \frac{1}{T}\right)\right]$ microprestress force $\qquad\qquad\quad \dot{S} = -H\dot{\gamma}$ viscous slip rule $\qquad\qquad\qquad\quad \dot{\gamma} = cS^2\exp\left[-\frac{U}{R}\left(\frac{1}{T} - \frac{1}{T}\right)\right]$

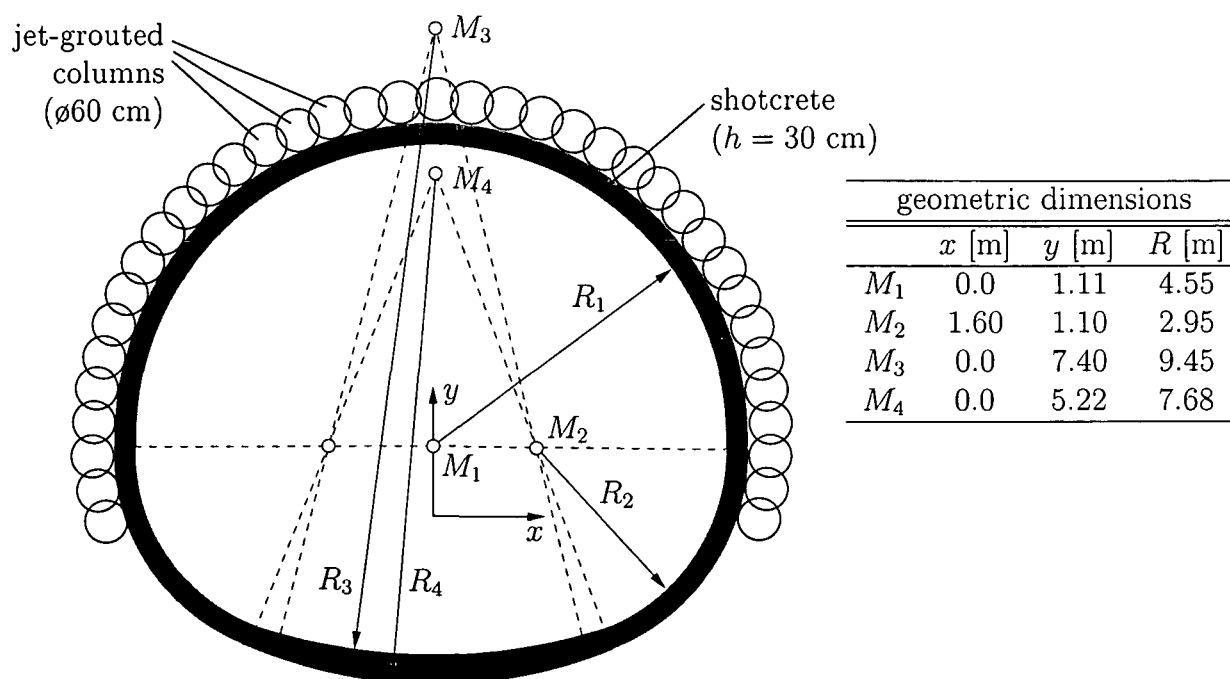Table 5.1: Governing equations for material model for shotcrete and soilcrete

geometric dimensions			
	x [m]	y [m]	R [m]
M_1	0.0	1.11	4.55
M_2	1.60	1.10	2.95
M_3	0.0	7.40	9.45
M_4	0.0	5.22	7.68

Figure 5.1: Numerical simulation of the tunnel excavation with HJG: Adopted geometry of the tunnel cross-section

5.1.2   Numerical simulations of tunnel excavations with jet grouting

In order to assess the performance of jet grouting in different geological conditions, the example of a tunnel excavation with low overburden is chosen. Here, minimization of settlements is an important issue in urban tunneling situations. Therefore, the application of jet grouting is a reasonable choice for the purpose of ground improvement. The excavation situation is chosen such that it resembles existing tunnel cross-sections for underground railroads. The geometry of the excavation is assumed as depicted in Figures 5.1 and 5.2, with an assumed overburden of about one tunnel diameter.   The applied construction scheme for the jet grouting of the columns prior to excavation is depicted in Figure 5.3. As can be seen in Figure 5.3, the construction scheme of the jet grouted columns has to follow a certain pattern in order to avoid interference with or destruction of adjacent "fresh" columns. The subsequent excavation is chosen as a staggered excavation (see Figure 5.4), starting 26 hours after completion of the last jet grouted column. A certain time span between completion of the last jet grouted column and the beginning of excavation is required in order to achieve a specific strength and stiffness of the jet grouted support ring.

For the numerical simulation, the structural model is chosen as depicted in Figure 5.5, where plane strain conditions are applied, based on the cone-shaped support ring of improved soil which leads to dominant load transfer in the circumferential direction because
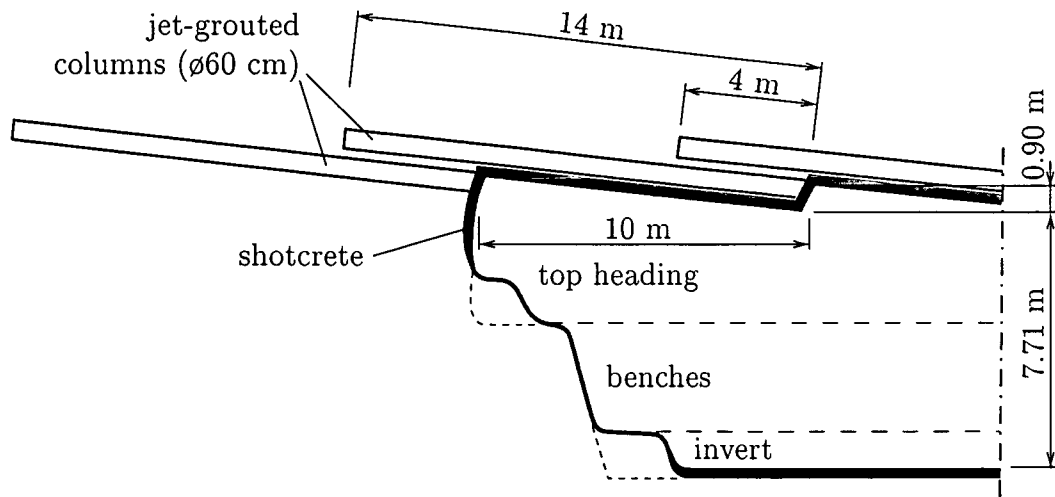
Figure 5.2: Numerical simulation of the tunnel excavation with HJG: longitudinal section

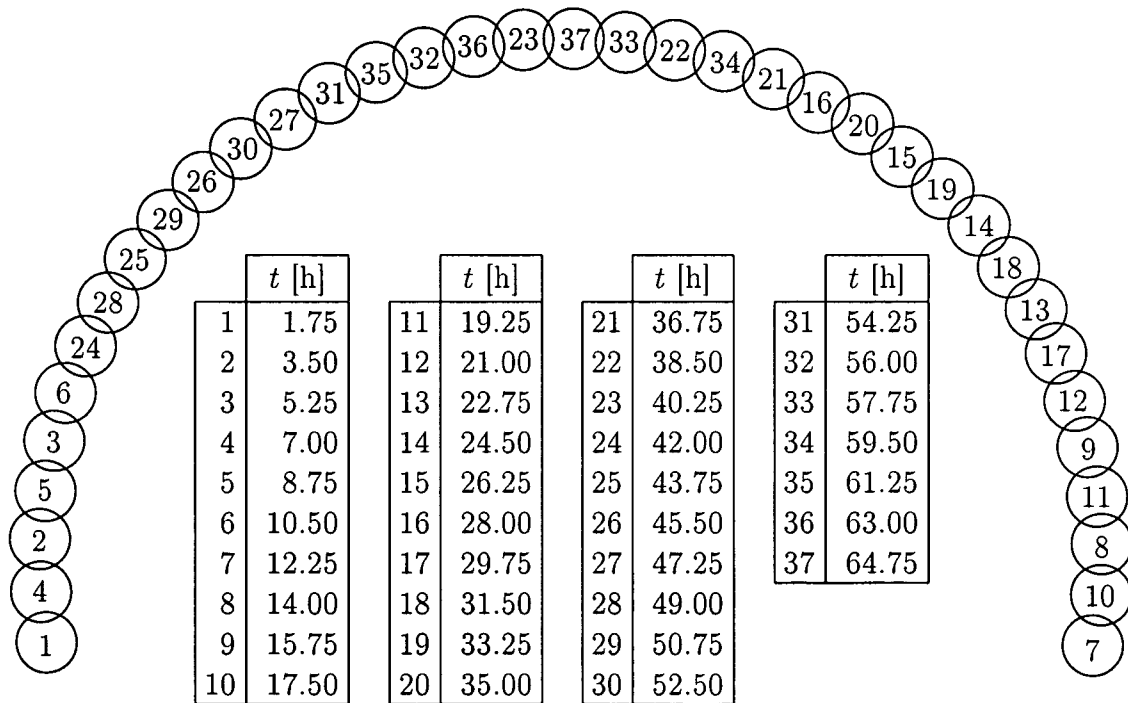|	t [h]		t [h]		t [h]		t [h]
1	1.75	11	19.25	21	36.75	31	54.25
2	3.50	12	21.00	22	38.50	32	56.00
3	5.25	13	22.75	23	40.25	33	57.75
4	7.00	14	24.50	24	42.00	34	59.50
5	8.75	15	26.25	25	43.75	35	61.25
6	10.50	16	28.00	26	45.50	36	63.00
7	12.25	17	29.75	27	47.25	37	64.75
8	14.00	18	31.50	28	49.00		
9	15.75	19	33.25	29	50.75		
10	17.50	20	35.00	30	52.50		

Figure 5.3: Numerical simulation of the tunnel excavation with HJG: jet grouting scheme for construction of support ring consisting of 37 jet grouted columns
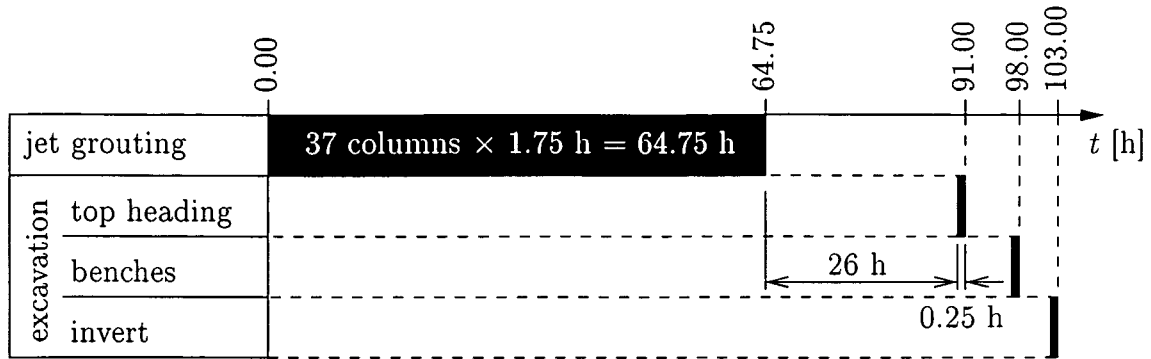
Figure 5.4: Numerical simulation of the tunnel excavation with HJG: time table for construction of jet grouted support ring and excavation
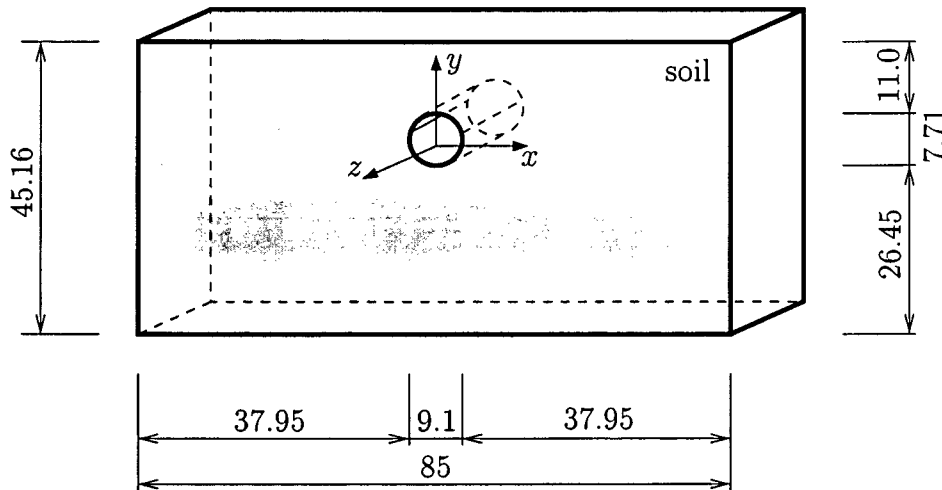

Figure 5.5: Numerical simulation of the tunnel excavation with HJG: geometric dimensions (in [m]) of the structural model

of the stiffness of the ring. The respective FE mesh, consisting of 5227 finite elements, is shown in Figure 5.5. The ground surrounding the excavation is assumed to be homogeneous and consists either of granular or cohesive soil. While the granular soil is assumed as medium dense sand [2], the cohesive soil is assumed as soft clay, similar to London clay (see also [76]). As regards the viscous response of the soil, the fluidity parameter τ of the granular soil is chosen such that interaction between creeping soil and hardening tunnel support is observed. In order to obtain a similar time-dependence for the cohesive soil, the viscosity η is chosen as $\eta = \tau_{granular\,soil} \cdot \tilde{E}_{cohesive\,soil}$ [h·MPa], with $\tilde{E}_{cohesive\,soil}$ being determined from the elastic modulus for the *in-situ* stress at 20 m depth. Both geological materials are characterized by the material parameters given in Tables 5.2 and 5.3.

Obviously, application of jet grouting in different geological conditions yields different properties of the cemented soil, and, hence, different structural performance. First, the kind and the grain size of the aggregate has a major influence on the final stiffness and
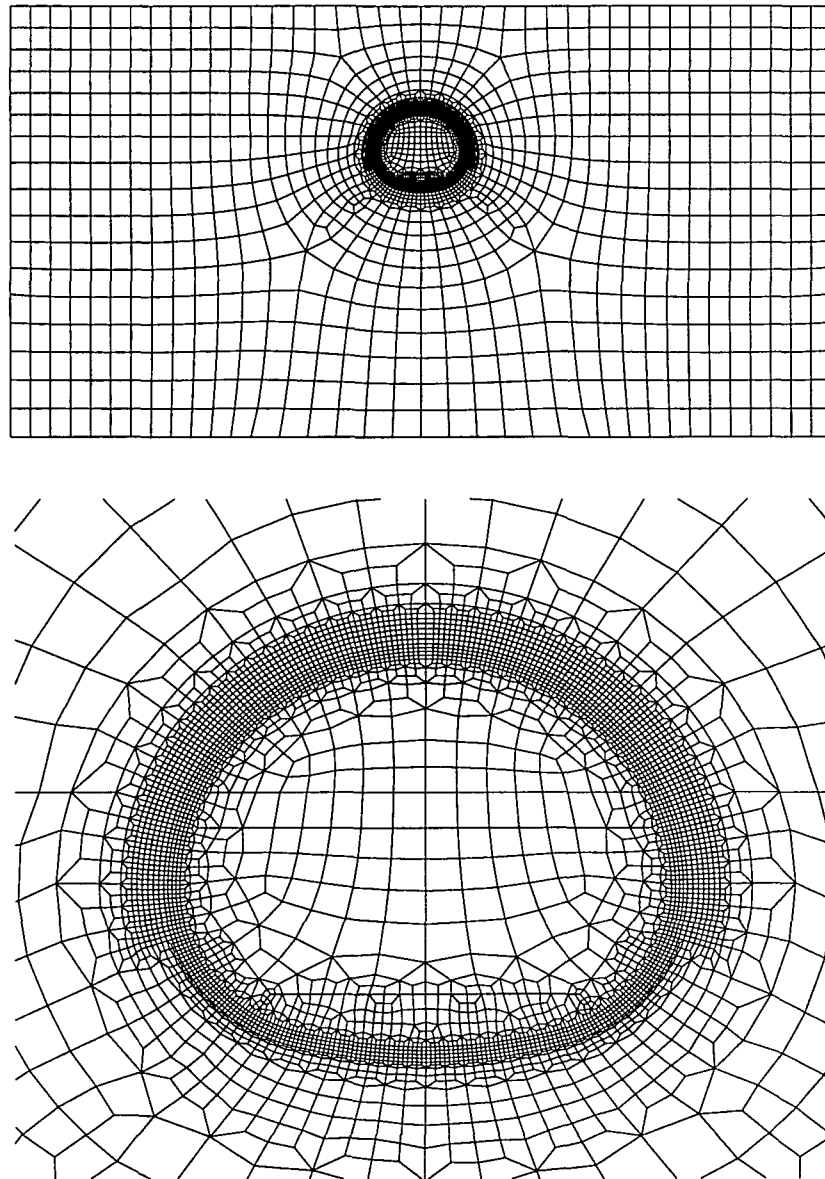
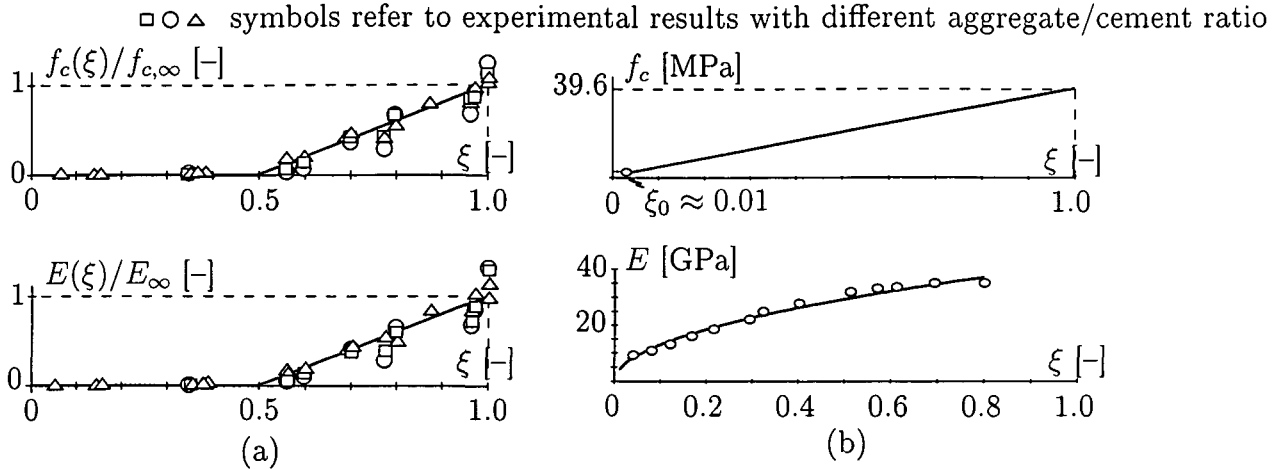Figure 5.6: Numerical simulation of the tunnel excavation with HJG: FE mesh consisting of 5227 finite elements

□ ○ △ symbols refer to experimental results with different aggregate/cement ratio

(a)   (b)

Figure 5.7: Numerical simulation of the tunnel excavation with HJG: Adopted
(qualitative) evolutions of compressive strength f_c and of Young's modulus
E for (a) soilcrete [11] and (b) shotcrete [35]

strength of the cemented soil. And second, the specific erodibility and penetrability of
the considered soil, together with the applied process parameters for jet grouting, like the
rate of withdrawal, the grout flow and pressure, the rotation, and possibly also the air or
water pressure and flow, influence the finally obtained aggregate/cement ratio, which also
effects stiffness and strength of the cemented soil[1]. Consequently, jet-grouted cohesive soil
has a lower stiffness and strength than jet-grouted granular soil. Accordingly, the final
compressive strength of jet grouted soil ranges from $\sigma_{cu} \leq 5$ MPa for jet grouted silts up to
$\sigma_{cu} \leq 25$ MPa for jet grouted gravels [28]. As regards the present example, the qualitative
evolution of the compressive strength and of Young's modulus are assumed as depicted in
Figure 5.7(a) [11] for both types of soils.

For the sake of completeness, not only the final compressive strength depends on the consid-
ered aggregate, but also the time-dependence of the evolution in consequence of hydration
is reported to be faster for jet grouted granular soil compared to jet grouted cohesive soil
[28]. Therefore, the considered aggregate has a major influence on the evolution of the
chemical affinity. However, in view of lack of experimental data on respective intrinsic ma-
terial functions of soilcrete in cohesive soil, the evolution of the hydration is assumed to be
the same for both soil types and is depicted in Figure 5.8(a). The underlying experimental
data in Figure 5.8(a) refer to mortar with granular aggregate. Figures 5.7(b) and 5.8(b)
show the respective evolutions of the considered shotcrete mixture.

As regards chemical shrinkage, the adopted intrinsic material function depicted in Fig-
ure 5.9 refers to a shotcrete mixture [35], but is also applied here to soilcrete.

---

[1]This is corroborated by experience, as the main component of soilcrete in granular soil – being an easily
erodible material – is the aggregate, whereas the main component of soilcrete in cohesive soil – being a
hardly erodible material – is the cement suspension. The latter is additionally confirmed by practical
experience from 2-3 fold reflux of slurry in cohesive soil.
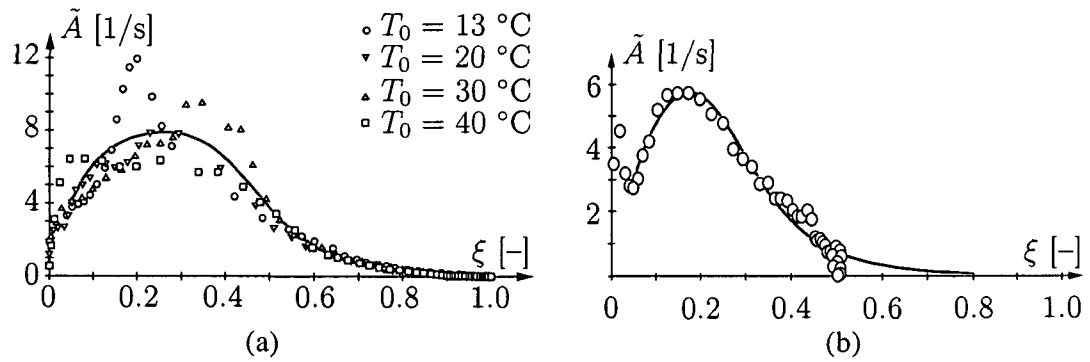
Figure 5.8: Numerical simulation of the tunnel excavation with HJG: Adopted evolutions of chemical affinity $\tilde{A}(\xi)$ for (a) soilcrete [11] and (b) shotcrete [35]
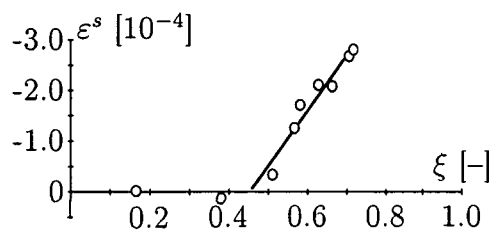

Figure 5.9: Numerical simulation of the tunnel excavation with HJG: Adopted evolution of shrinkage strains for soilcrete and shotcrete [35]
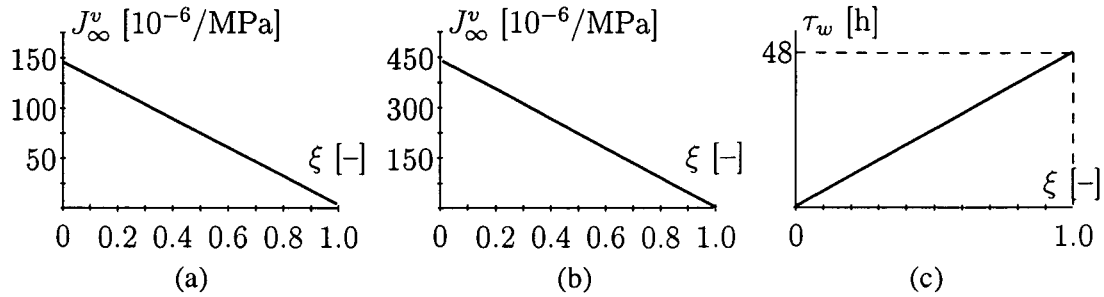
Figure 5.10:   Numerical simulation of the tunnel excavation with HJG:
Adopted evolutions of asymptotic viscous compliance for (a) soilcrete and
(b) shotcrete; and (c) evolution of characteristic time for short-term creep
for soilcrete and shotcrete [11]

Creep characteristics are employed as depicted in Figure 5.10 [11].

Tables 5.2 and 5.3 contain a summary of the adopted chemomechanical material parameters
for shotcrete and soilcrete in granular and cohesive soil, respectively. Here, the chosen
Young's modulus and compressive strength for soilcrete in cohesive soil refer to pure cement
suspension, based on the observation that cement suspension is the main compound of jet
grouted cohesive soil.

chosen set of material parameters for sand, soilcrete, and shotcrete			
	sand	soilcrete	shotcrete
unit weight of material, γ [MN/m^3]	0.017	0.021	0.025
(final) Young's modulus, E [MPa]	45	1 500	40 800
Poisson's ratio, ν [–]	0.35	0.2	0.2
initial friction angle, φ_i [°]	20	–	–
peak friction angle, φ_p [°]	30	–	–
cohesion, c [MPa]	0.001	–	–
peak dilation angle, ψ_p [°]	4	–	–
internal variable α_{MC} at $\varphi = \varphi_p$, $\alpha_{MC,m}$ [–]	0.03	–	–
fluidity parameter, τ [h]	0.15	–	–
final compressive strength, $f_{c,\infty}$ [MPa]	–	8.0	39.6
initial compressive strength, $f_{c,0}$ [MPa]	–	$f_c/4$	$f_c/4$
tensile strength, f_t [MPa]	–	$f_c/10$	$f_c/10$
f_b/f_c [–]		1.16	1.16
relaxation modulus H [MPa]	–	$1 \cdot 10^6$	$1/7 \cdot 10^6$
total strain at peak load, ε_m [–]	–	-0.0022	-0.0022
shrinkage parameter $\beta = a_s + b_s\xi$			
a_s [–]	–	$-4.05 \cdot 10^{-4}$	$-4.05 \cdot 10^{-4}$
b_s [–]	–	$9.43 \cdot 10^{-4}$	$9.43 \cdot 10^{-4}$
asymptotic viscous compliance $J^v_\infty = a_v(1 - \xi)$			
a_v [μm/(m MPa)]	–	148.5	445
characteristic time for short-term creep τ_w [h]	–	48	48
activation term U/R [K]	–	2 700	2 700
reference temperature $\bar{T}$ [°C]	–	20	20
activation term E_a/R [K]	–	4 000	4 000
chemical affinity $\tilde{A} = a_A \frac{1-\exp(-b_A\xi)}{1+c_A\xi^{d_A}}$			
a_A [1/s]	–	8.24	7.31
b_A [–]	–	13.3	10.5
c_A [–]	–	117.0	169.0
d_A [–]	–	6.63	4.37
temperature T_0 [°C]	10	20	20

Table 5.2: Chemomechanical analyses: employed material parameters and assumed temperatures for shotcrete [77, 36], jet grouted soil mass [70, 11], and sand [2]

chosen set of material parameters for clay, shotcrete, and soilcrete			
	clay	soilcrete	shotcrete
unit weight of material, γ [MN/m^3]	0.0235	0.017	0.02428
(final) Young's modulus, E [MPa]	–	550	40 800
Poisson's ratio, ν [–]	–	0.2	0.2
slope of the normal compression line, λ [–]	0.161	–	–
slope of the unloading-reloading line, κ [–]	0.062	–	–
slope of the critical state line, M [–]	0.88	–	–
initial specific volume, v_0 [–]	2	–	–
initial size of the elastic domain, q_0 [MPa]	0.80	–	–
tensile strength, t [MPa]	0.23	–	–
amount of coupling in elasticity, $\bar{\alpha}$ [–]	15	–	–
viscosity of the soil, η [MPa· h]	3	–	–
final compressive strength, $f_{c,\infty}$ [MPa]	–	2.5	39.6
initial compressive strength, $f_{c,0}$ [MPa]	–	$f_c/4$	$f_c/4$
tensile strength, f_t [MPa]	–	$f_c/10$	$f_c/10$
f_b/f_c [–]	–	1.16	1.16
relaxation modulus H [MPa]	–	$1 \cdot 10^6$	$1/7 \cdot 10^6$
total strain at peak load, ε_m [–]	–	-0.0022	-0.0022
shrinkage parameter $\beta = a_s + b_s\xi$			
a_s [–]	–	$-4.05 \cdot 10^{-4}$	$-4.05 \cdot 10^{-4}$
b_s [–]	–	$9.43 \cdot 10^{-4}$	$9.43 \cdot 10^{-4}$
asymptotic viscous compliance $J^v_\infty = a_v(1 - \xi)$			
a_v [μm/(m MPa)]	–	148.5	445
characteristic time for short-term creep τ_w [h]	–	48	48
activation term U/R [K]	–	2 700	2 700
reference temperature $\bar{T}$ [°C]	–	20	20
activation term E_a/R [K]	–	4 000	4 000
chemical affinity $\tilde{A} = a_A\frac{1-\exp(-b_A\xi)}{1+c_A\xi^{d_A}}$			
a_A [1/s]	–	8.24	7.31
b_A [–]	–	13.3	10.5
c_A [–]	–	117.0	169.0
d_A [–]	–	6.63	4.37
temperature T_0 [°C]	10	20	20

Table 5.3: Chemomechanical analyses: employed material parameters and assumed temperatures for shotcrete [77, 36], jet grouted soil mass [28, 11], and clay [76]
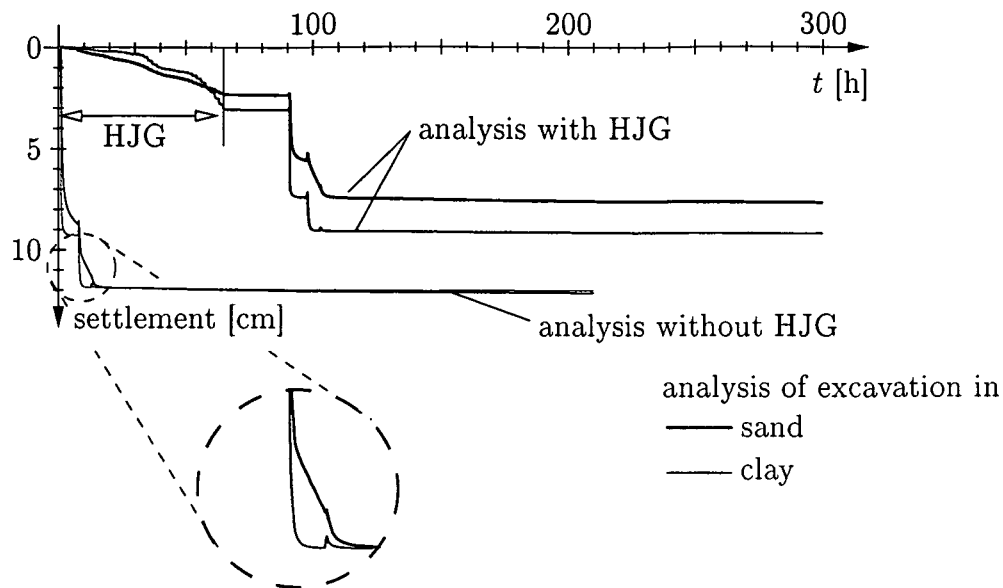
Figure 5.11: Numerical simulation of the tunnel excavation with HJG: surface settlements above crown

The numerically obtained results depicted in Figure 5.11 clearly show that ground improvement by means of HJG prior to the excavation leads to a considerable reduction of the surface settlements, even though ground improvement already yields settlements of about one third of the final ones. The most considerable settlements are obtained during excavation of the heading, subsequent excavation steps give less settlements. However, application of HJG in granular soil is more efficient, resulting in a reduction of about 33% compared to a reduction of about 25% for HJG in clay. This higher effect of HJG in granular soil is explained by the higher stiffness of the soilcrete support ring in granular soil (see Tables 5.2 and 5.3). Hence, also the settlements prior to excavation, obtained for the simulation with HJG in granular soil, are lower than the respective settlements for cohesive soil. However, it can be observed that the structural creep process is comparably slower in granular soil. One reason for this longer lasting structural creep process in granular soil is the larger deviation of the direction of plastic flow from the direction of loading in the Mohr-Coulomb criterion, as depicted in Figure 5.12.

Figures 5.13 and 5.14 elucidate the plastic response of the granular and cohesive soil, respectively, by means of the internal hardening variable α_{MC} and α_{CC}, respectively. Both soils undergo solely hardening during the numerical simulation. As regards the Cam-Clay model, hardening results from the applied lateral earth pressure coefficient $K_0 = 1 - \sin\varphi = 0.5$, yielding stress states located below the critical state line and, hence, directed to the strain hardening side. It can be observed for both soils that application of HJG leads to a reduction of the plastic zones outside the upper part of the soilcrete support ring. This reduction of plastic zones follows from restrained soil deformation because of the increased stiffness of the cemented soil surrounding the excavation. As regards granular soil, plastic
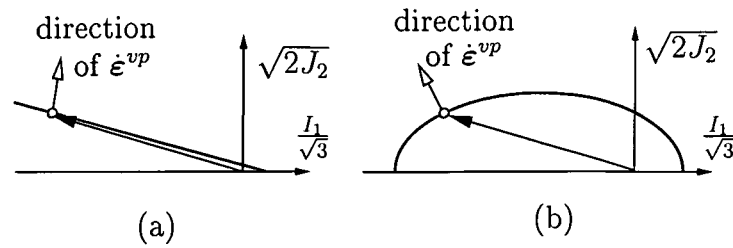
(a)   (b)

Figure 5.12: Numerical simulation of the tunnel excavation with HJG: illustration of direction of plastic flow and direction of loading for (a) Mohr-Coulomb model and (b) Cam-Clay model
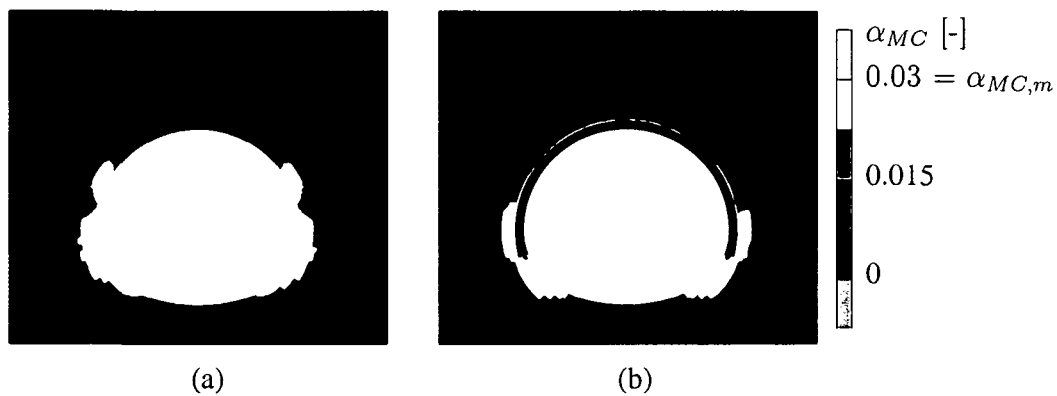

(a)   (b)

Figure 5.13: Numerical simulation of the tunnel excavation with HJG: distribution of internal hardening variable α_{MC} for granular soil, seven days after installation of the invert for the analysis (a) disregarding HJG and (b) considering HJG
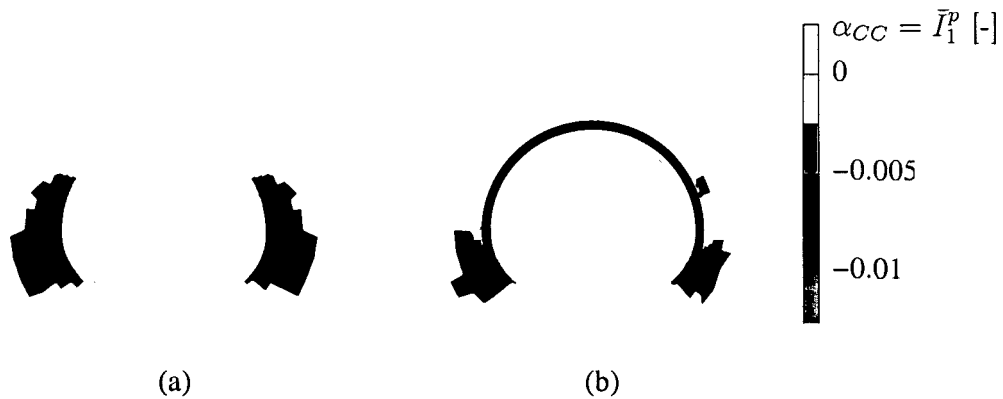

(a)   (b)

Figure 5.14: Numerical simulation of the tunnel excavation with HJG: distribution of internal hardening variable α_{CC} for cohesive soil, seven days after installation of the invert for the analysis (a) disregarding HJG and (b) considering HJG

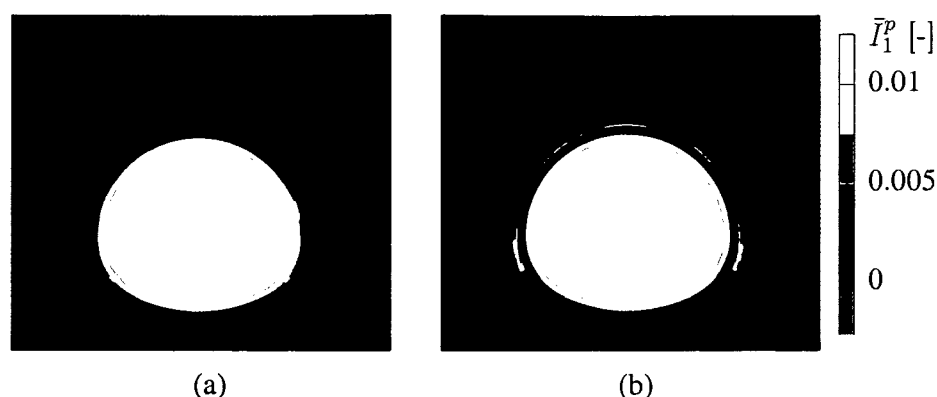(a)   (b)

Figure 5.15: Numerical simulation of the tunnel excavation with HJG: distribution of volumetric plastic strain $\bar{I}_1^p$ in granular soil, seven days after installation of the invert for the analysis (a) disregarding HJG and (b) considering HJG

response is encountered at the wo sides of the tunnel. For the case of disregard of HJG, the plastified area extends directly from the tunnel springlines upwards. In the plastic zones, the shear resistance of the granular soil is activated, as is implied by the employed Mohr-Coulomb model. In contrast to this, the plastic zones in cohesive ground are concentrated at the benches, in case of disregard of HJG, and at the bottom part of the support ring, in case of consideration of HJG. As implied by the Cam-Clay model, the increase of the material resistance is associated with plastic compaction.

Additionally, the distribution of plastic volumetric strain $\bar{I}_1^p$ is illustrated in Figure 5.15 for the analysis for granular soil. As regards the analysis for cohesive soil, volumetric plastic strain is identical to the internal state variable (see Figure 5.14), resulting from the adopted (volumetric) hardening law. As assigned by the underlying models, granular soil exhibits plastic dilation, whereas cohesive soil – as a consequence of predominantly hydrostatic loading – undergoes plastic compaction. As regards granular soil, the area of plastic dilation is limited to the vicinity of the tunnel benches, where the shear resistance is activated. Opposed to the observed limited dilation in granular soil, plastic compaction in cohesive soil is more distributed (see Figure 5.14), resulting from the employed value of λ in the (volumetric) hardening law. Additionally, as regards the analysis considering HJG, the soil acts as support of the soilcrete ring at its footings, because of its low stiffness.

In Figure 5.16, the effect of HJG on the horizontal tunnel convergence is shown. Whereas the simulation disregarding HJG results in overall horizontal convergence, the simulation considering HJG yields overall divergence for HJG in cohesive soil, and little overall convergence for HJG in granular soil. It can be observed that the excavation of the benches in granular soil results in a considerable inward displacement. This displacement is not observed for the analysis of HJG in cohesive soil, resulting from plastic compaction at the tunnel benches. Comparison of the horizontal convergence from the analysis considering HJG in granular and cohesive soil with the one from the analysis characterized by disre-
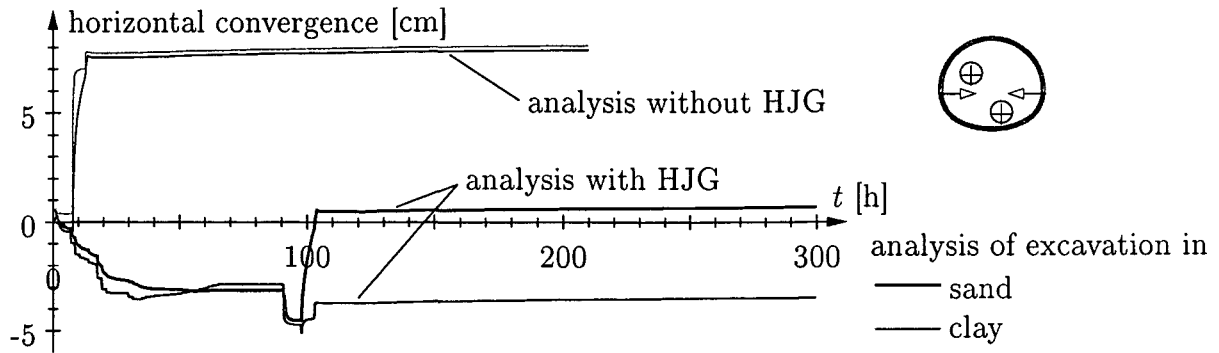
Figure 5.16: Numerical simulation of the tunnel excavation with HJG: horizontal
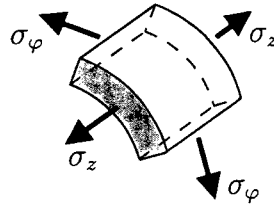convergence

Figure 5.17: Numerical simulation of the tunnel excavation with HJG: illustra-
tion of axial stress σ_φ and out-of-plane stress σ_z in the lining

gard of HJG yields a "higher" effect of application of HJG in cohesive soil. However, the
resulting divergence can be judged as unfavorable as it leads to distortion of the soilcrete
support ring and of the shotcrete lining. This is confirmed by the axial forces in the support
ring, determined as

$$n_\varphi = \int_h \sigma_\varphi dr \ , \tag{5.1}$$

with the direction φ of the stresses defined as depicted in Figure 5.17. The evolution of
axial forces in the soilcrete support ring is illustrated in Figure 5.18 for sections located
at the crown, and the shoulder and the bench, respectively. Figure 5.18 shows that small
compressive forces develop already during the jet grouting process, resulting from stress-
redistributions in consequence of the disturbance of the initial ground conditions. However,
the most significant increase of n_φ occurs during the excavation of the heading. While
subsequent excavation steps do not change n_φ at the crown considerably, there are some
changes in the shoulder and significant changes in the bench for the case of excavation in
granular soil. The observed changes of compressive forces in the bench are explained by
the inward displacement of the benches after bench excavation (see Figure 5.16). A similar
horizontal convergence was not observed for cohesive soil. Hence, there is singnificantly
less reduction of compressive forces in this case. Additionally, Figure 5.18 shows similar
final amounts of n_φ for HJG in granular soil, but values increasing from the crown to the
benches for HJG in cohesive soil, indicating uniform axial loading of soilcrete in granular
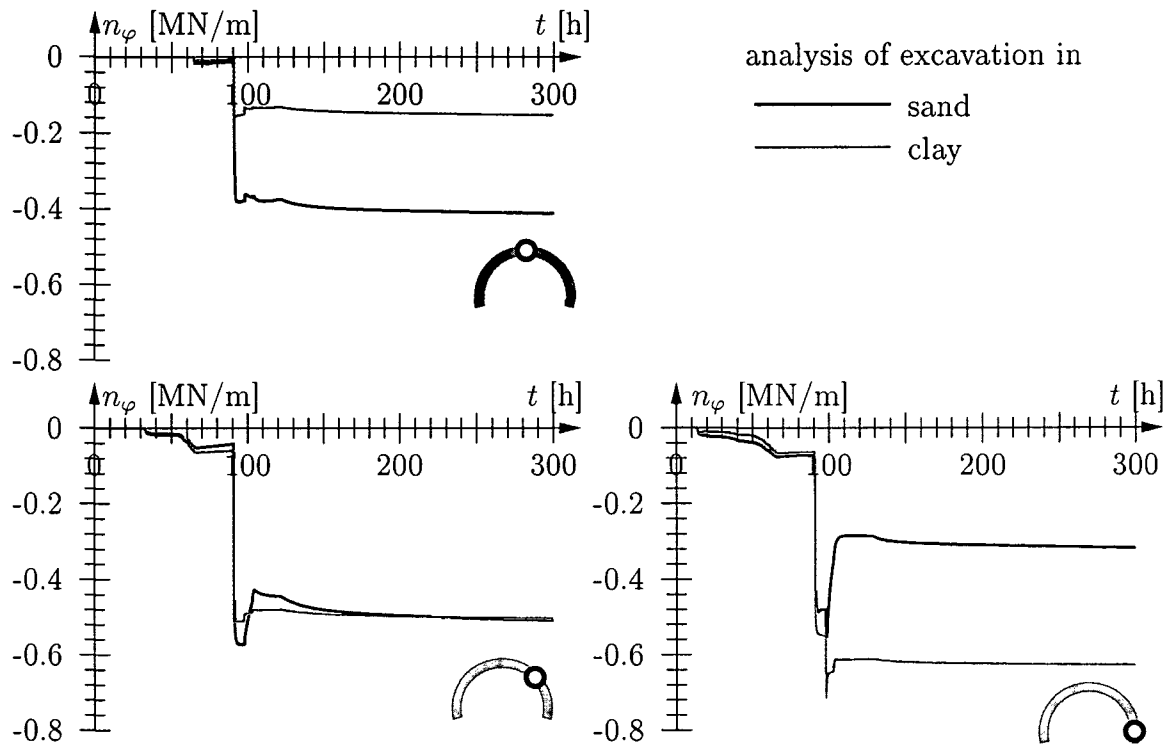soil, and non-uniform loading of soilcrete in cohesive soil.

Figure 5.18: Numerical simulation of the tunnel excavation with HJG: evolution of axial force n_φ in sections located at the crown, the shoulder, and the bench of the soilcrete support ring
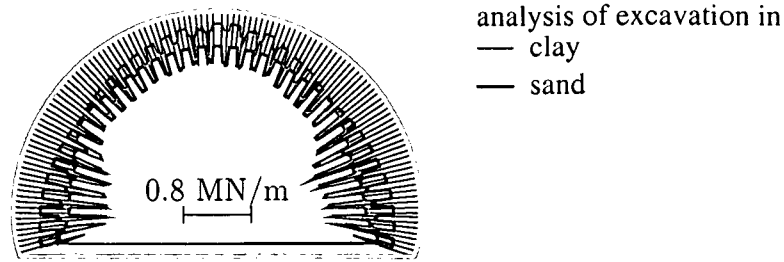
Figure 5.19: Numerical simulation of the tunnel excavation with HJG: distribution of axial force n_φ in the soilcrete lining for excavation with HJG seven days after installation of the invert

This observation is confirmed by the distribution of the axial forces seven days after completion of the invert in the soilcrete support ring, as depicted in Figure 5.19. Here, a rather uniform loading for HJG in granular soil can be observed, while the nonuniform loading for HJG in cohesive soil is greater at the benches and smaller at the crown. Hence, as is shown by Figures 5.11 and 5.16, there is more distortion of the soilcrete support ring in cohesive soil than in granular soil. The increased distortion of the soilcrete support ring in cohesive soil can be explained by the smaller stiffness of soilcrete in cohesive soil as compared to soilcrete in granular soil (see Tables 5.2 and 5.3). Additionally, the degree of loading is higher for soilcrete in cohesive soil because of the smaller compressive strength. The maximum loading of the support ring in cohesive soil(granular soil) amounts to $n_\varphi \approx 0.7(0.6)$ MPa, corresponding to 70(40)% of the load-carrying capacity of the soilcrete, estimated for an intermediate thickness of the support ring as $f_{c,\infty} \cdot h = 2.5$ MPa $\cdot 0.40$ m $= 1.0$ MN/m for soilcrete in cohesive soil, and $f_{c,\infty} \cdot h = 8.0$ MPa $\cdot 0.40$ m $= 3.2$ MN/m for soilcrete in granular soil, respectively.

The evolution of the axial forces in the shotcrete lining is illustrated in Figure 5.20. Generally, an increase of compressive forces is observed in consequence of the excavation process. After installation of the benches, the compressive forces reach a peak value and decrease in the course of time because of creep. This decrease of compressive forces is more pronounced for the analyses considering HJG, resulting from an additional stress-redistribution between the soilcrete support and the shotcrete lining (see also Figure 5.18). However, application of HJG yields a considerable overall reduction of time-dependent compressive forces compared to the analysis disregarding HJG. This reduction results from the support ring, which restricts the deformations and, hence, the loading of the shotcrete lining (see also Figures 5.11 and 5.16). According to the distortion of the shotcrete lining, which is deduced from the Figures 5.11 and 5.16, this reduction is more significant at the crown for the excavation in granular soil, and more pronounced at the benches for the excavation in cohesive soil. But, even though the relative reductions obtained from HJG are considerable, the loading of the lining is hardly exceeding 4% of the final load-carrying capacity, given by $f_{c,\infty} \cdot h = 39.6$ MPa $\cdot 0.30$ m $= 11.88$ MN/m.

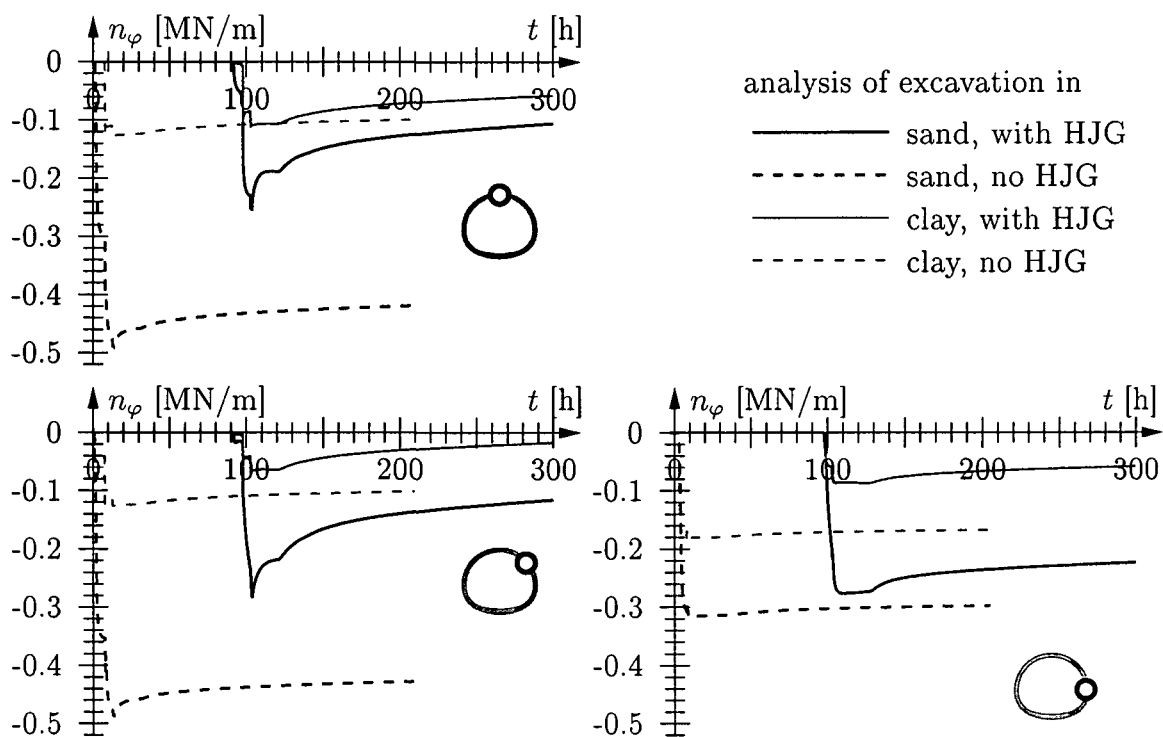The distribution of the axial forces is shown in Figure 5.21 for the shotcrete lining, seven

Figure 5.20: Numerical simulation of the tunnel excavation with HJG: evolution of axial force n_φ in sections located at the crown, the shoulder, and the bench of the shotcrete lining
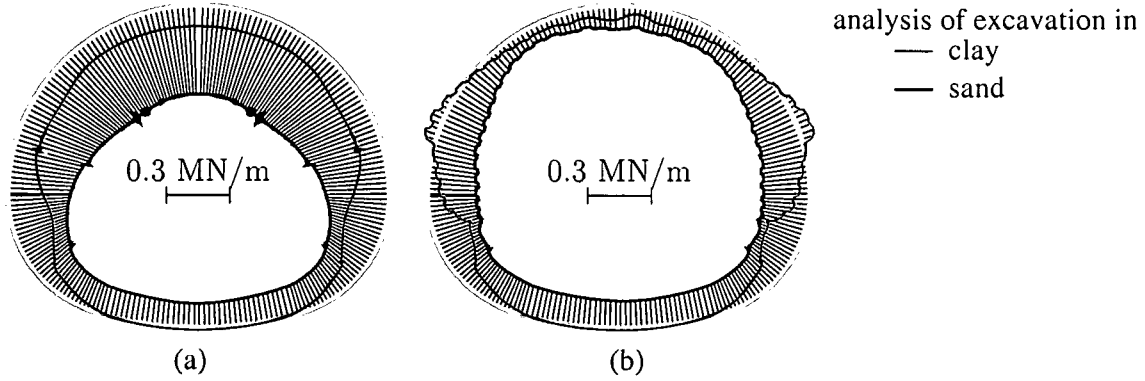
Figure 5.21: Numerical simulation of the tunnel excavation with HJG: distribution of axial force n_φ in the shotcrete lining seven days after installation of the invert for excavation (a) without HJG and (b) with HJG

days after installation of the invert. It can be observed that the compressive forces are higher and more uniform for the excavation in granular soil and that application of HJG results in lower compressive forces. As regards HJG in cohesive soil, bending effects in the soilcrete/shotcrete compound structure occur, resulting from the relatively low stiffness of the soilcrete support ring in cohesive soil.

For information on the structural effects of the chemomechanical material models for shotcrete and soilcrete, the evolution of the axial stretches $\epsilon^p, \epsilon^{shr}, \epsilon^v$, and ϵ^f is evaluated in a section located at the shoulder. The axial stretches are determined as

$$\epsilon_\varphi = \frac{1}{h} \int_h \varepsilon_\varphi dr \ . \tag{5.2}$$

As regards the soilcrete support ring, the evolution of the axial stretches from the chemomechanical model is illustrated in Figure 5.22. In the considered situation, the shrinkage stretches dominate the chemomechanical response. Because of the simplified isothermal computation, thermal stretches are zero, and, as shrinkage exclusively depends on hydration, the depicted shrinkage stretches are identical for the computations in granular and cohesive soil, respectively. Plasticity is negligible, as the major loading of the soilcrete starts when a certain strength and stiffness is already obtained. Short-term creep, depending on the degree of hydration and on the loading, is present, but it is also very small, again resulting from the delayed loading of the soilcrete support. As implied by the model (see Table 5.1 and Figure 5.10), loading after some hydration results in a rapidly decreasing influence of $(1/\tau_w)J_\infty^v$, and, hence, in small viscous or short-term stretches. As regards long-term creep under isothermal conditions with equal material and reference temperature, $T = T_0 = \bar{T}$ (see Tables 5.2 and 5.3 and [35]), the flow creep viscosity can be reduced to $1/\eta_f = 1/\eta_{f,0} = 1/(Ht)$ (see [35]), and, hence, only the load and the time influence the long-term creep rate $\varepsilon^f = (1/\eta_f)\mathbf{G} : \boldsymbol{\sigma}$. Once more, the delay of the application of the load is responsible for almost zero creep stretches, as the factor $1/Ht$ leads to a rapid decrease of the influence of the long-term creep rate $\dot{\varepsilon}^f$.
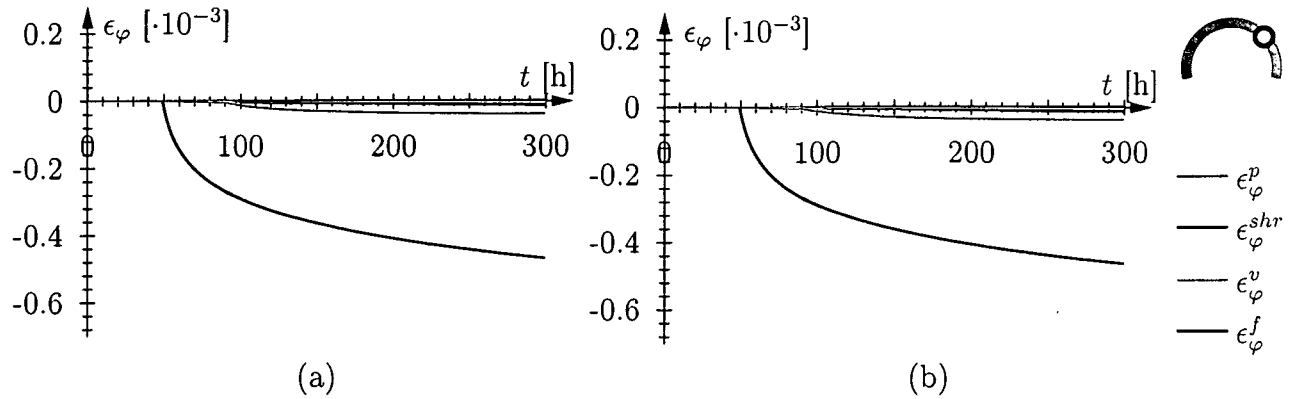
Figure 5.22: Numerical simulation of the tunnel excavation with HJG: evolution of axial stretches ϵ_φ at the shoulder in the soilcrete support ring for the analysis in (a) granular soil and (b) cohesive soil
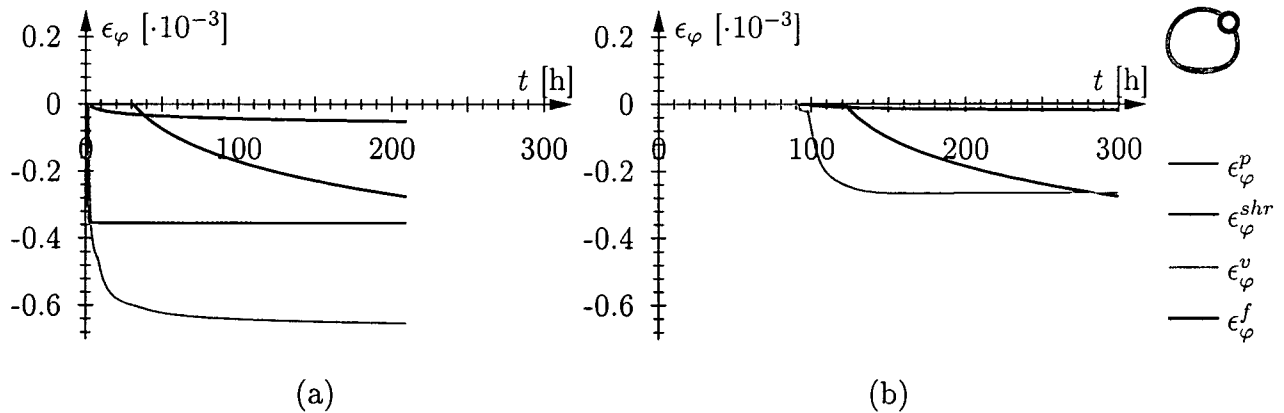

Figure 5.23: Numerical simulation of the tunnel excavation with HJG: evolution of the axial stretches ϵ_φ at the shoulder of the shotcrete lining for the analysis in granular soil (a) disregarding HJG and (b) considering HJG

Considering the shotcrete lining, the respective stretches at the shoulder are depicted in Figures 5.23 and 5.24 for the analyses considering granular and cohesive soil, respectively. Here, the results are quite different from the previous ones: all considered chemomechanical phenomena contribute to the structural response. For the simulations disregarding HJG, plastification occurs when the early loaded shotcrete is still rather young and the compressive strength is small. This plastification is more pronounced for the analysis in granular soil, caused by the slower creep process. Plastification in cohesive soil is associated with tensile stretches, occurring during bench excavation. For the simulations considering HJG, there is no plastification, because the loading of the shotcrete lining is considerably smaller.

For the aforementioned reason of isothermal conditions, shrinkage is the same in all simulations. Comparing the shrinkage stretches obtained for soilcrete with the ones obtained for
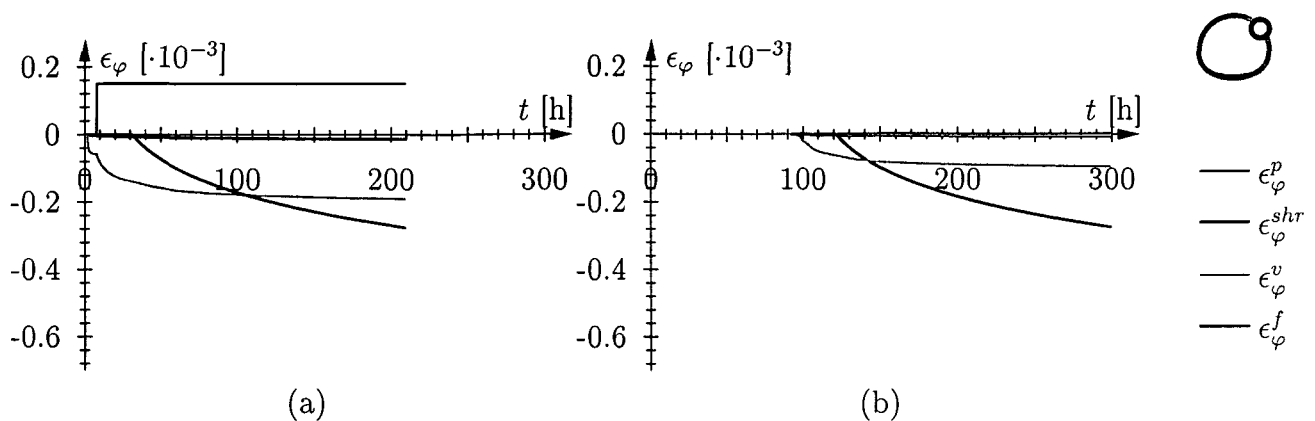
Figure 5.24: Numerical simulation of the tunnel excavation with HJG: evolution of the axial stretches ϵ_φ at the shoulder of the shotcrete lining for the analysis in cohesive soil (a) disregarding HJG and (b) considering HJG

shotcrete, the evolution of the stretches is slower in shotcrete, resulting from the adopted evolutions of the chemical affinity (see Figure 5.8). As can be seen in Figure 5.8, the hydration process is faster for soilcrete, yielding higher shrinkage stretches.

Short-term creep provides a major contribution to the structural response in all considered simulations resulting from the rather early loading with respect to the hydration process. As the loading is higher for the analyses disregarding HJG, the short-term creep stretches are also higher. And, because of the slower creep of the granular soil, loading is higher in granular soil and, hence, short-term creep stretches play a superior role in granular soil.

Long-term creep stretches are only worth mention for the case of disregard of HJG in granular soil, also because of the higher loading of the shotcrete shell in granular soil.

5.1.3 Concluding remarks

The analyses concerning the application of HJG in granular and cohesive soil clearly show basic differences as regards tunneling with and without ground improvement in cohesive, respectively granular soil. Such differences address surface settlements, plastic dilatancy and compaction, horizontal divergence and convergence, and the load-carrying behavior of the tunnel support.

As regards minimization of settlements, which is often the reason for HJG in urban areas, HJG in granular soil was found to be highly efficient, yielding 33% settlement reduction. The settlement reduction obtained from the analyses considering cohesive soil was still 25%. Additionally, unfavorable horizontal divergence and bending effects were observed in the simulations for cohesive soil. This was not the case for the analyses in granular soil. This bending was attributed to the small stiffness of the soilcrete support ring in cohesive soil. Here, numerical studies on the form of the soilcrete support could yield a generally more favorable form of soilcrete support in cohesive soil.

Concerning the employed chemomechanical material models for soilcrete and shotcrete, the presented results from simulations show that, generally, all considered phenomena occur during the tunneling process. However, for HJG applications, where a certain degree of hydration is obtained before the excavation starts (in the present example, $\xi > 0.5$), only shrinkage seems to have a considerable influence. But still, numerical studies where the time instant of excavation is varied, can be useful for the optimization of the progress of the construction work and of tolerable surface settlements. For such computations, also short-term creep and possibly plasticity could be relevant. The numerical results obtained for the shotcrete lining show that all considered chemomechanical phenomena occur in the presented example. As regards plasticity, shrinkage, and short-term creep, the significance of these phenomena depends on the creep properties of the soil and on the applied means of tunnel support. Hence, consideration of all three of these phenomena is relevant. However, long-term creep seems to be negligible in comparison with the other effects. Hence, based on the presented example, omitting long-term creep in numerical simulation of soilcrete/shotcrete applications in tunneling can be justified.

It needs to be pointed out here that, as regards the analyses for cohesive soil, the presented numerical simulations are based on partly improper assumptions concerning intrinsic material functions for soilcrete. The reason for this deficiency is lack of respective experimental data. Estimation of such data would render more realistic numerical results concerning the evolution of hydration, and the phenomena coupled to hydration.

5.2 Investigation of the influence of the description of the elastic law on the structural response in tunnel excavation simulations

According to experimental observations (see Section 3.1), soil behaves non-linearly elastic during unloading and subsequent reloading. Accordingly, elasto-plastic material models for soil often account for non-linear elastic behavior [98, 13, 9, 62]. However, the formulations of nonlinear elastic behavior of soil differ, and none of them seems to be generally accepted. Furthermore, there is still a variety of elasto-(visco)plastic models proposed in the open literature comprising linear elastic behavior for soil [22, 94, 30, 53]. Hence, the question arises, how relevant the elastic law in elasto-viscoplastic computations is.

As a numerical investigation of the structural effect of the adopted elastic law could not be found in the open literature, a pertinent study considering the application to tunnel excavations is documented in the following section. In this numerical study, the Cam-Clay model from Section 3.4 is applied, first, together with the proposed non-linear elastic law derived from $\mathcal{W}^3$ (see Equation (3.134)) and, second, together with the linear elastic law, i.e., Hooke's law (see Equation (3.137)). On the basis of this study, the influence of the elastic law on the displacements, the development of plastic zones in the soil and in the shotcrete lining, and on the axial forces in the lining will be discussed.

Additionally, the question on the impact of the elastic law with respect to general uncertainties concerning the soil characteristics will be posed. Such uncertainties may exist in the form of considerable changes of soil properties within short distances. Generally, uncertainties concerning ground properties are reduced by means of dense extraction of specimens from the ground and increased laboratory testing. However, unlike soil properties, primary conditions, e.g., in the form of the lateral earth pressure, the overconsolidation ratio, or the viscosity of the soil, are generally not determined experimentally, but by assumptions based on information concerning the geologic history or on the experience from former construction works under similar ground conditions[2]. Also numerical back-computation is used for determination of primary conditions or soil properties [75, 27, 67].

However, the structural effect of the elastic law in numerical elasto-viscoplastic excavation analysis with respect to the impact of variations of the primary state is another interesting question.

Accordingly, the effect of the elastic law under different primary ground conditions will be studied in a subsequent section.

5.2.1 Primary example

The chosen tunnel is assumed to be located about one tunnel diameter below the surface in cohesive soil. The tunnel geometry is illustrated in Figure 5.25. The construction scheme is chosen as depicted in Figure 5.26. The excavation scheme is characterized by subsequent excavation of the heading, of the benches, and of the invert. The time interval between two subsequent excavation steps is assumed as $t = 120$ h. Such relatively long time intervals are linked with the distances encountered for separate driving processes of the individual sections. These conditions are usually met for tunneling processes in the country side, where large surface settlements are admitted and, hence, fast closure of the support ring is not essential. Each excavation step is assumed to take $t = 0.50$ h, and the installation of the respective lining is assumed with some delay after $t = 0.50$ h upon completion of the excavation.

For this numerical study, the material parameters for cohesive soil estimated in Section 3.4.2 are modified in order to obtain elasto-plastic behavior during the simulation of the excavation process. Hence, the modified parameters might resemble a hard clay characterized by Mohr-Coulomb failure parameters $c = 0.08$ MPa and $\varphi = 20°$ (see [2]). The employed material properties for cohesive soil are summarized in Table 5.4. No attempt was made to use Cam-Clay material parameters for the compressive behavior (λ, κ, and v_0) from the literature, as they are generally estimated from clays which are too soft for use of NATM tunneling without additional support means (e.g., anchoring, steel arches, jet grouting, and/or soil freezing). However, as regards the linear elastic model, the values of the compression modulus K and of the shear modulus G were determined from averaged values

---

[2]It shall be noted here that there exist experimental tools for determination of the lateral earth pressure [7]. But still, the result is a pointwise information which is highly subjected to local variations. Hence, the determination of meaningful profiles seems to be rather tedious [45].
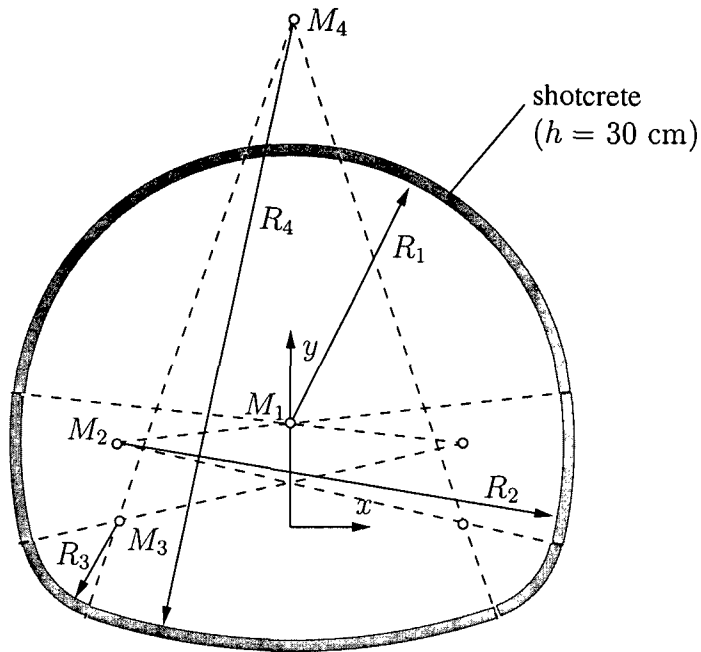
geometric dimensions			
	x [m]	y [m]	R [m]
M_1	0.0	2.30	6.05
M_2	-3.93	1.86	10.00
M_3	-3.88	0.10	2.00
M_4	0.0	11.50	14.05

Figure 5.25: Numerical simulation of the tunnel excavation in cohesive soil: geometry of the tunnel cross-section
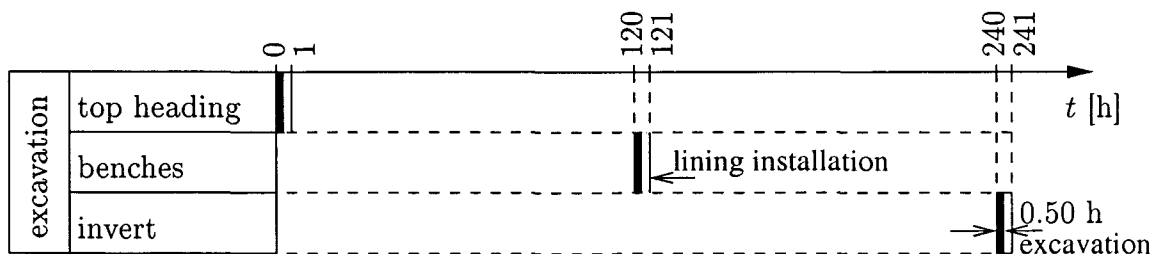

Figure 5.26: Numerical simulation of the tunnel excavation in cohesive soil: time table for construction of the excavation and installation of the shotcrete lining

material parameters employed for cohesive soil	
unit weight of material, γ [MN/m^3]	0.0235
slope of the normal compression line, λ [-]	0.040
slope of the unloading-reloading line, κ [-]	0.008
initial size of the elastic domain, q_0 [MPa]	0.80
slope of the critical state line, M [-]	0.61
tensile strength, t [MPa]	0.22
initial specific volume, v_0 [-]	1.30
amount of coupling in elasticity, $\tilde{\alpha}$ [-]	100.0
compression modulus for linear elastic law, K [MPa]	94
shear modulus for linear elastic law, G [MPa]	57
viscosity η [MPa·h]	200

Table 5.4: Numerical simulation of tunnel excavation in cohesive soil: material parameters employed for cohesive soil

of the elastic stiffness matrix obtained from the non-linear elastic model for an assumed primary stress state in a depth of 20 m (and, hence, Young's modulus E and Poisson's ratio ν can be computed using the dependence of elastic constants).

The primary stress state of the soil is applied according to Jaky's theory of the ratio of horizontal to vertical stresses $K_0 = \sigma_h/\sigma_v = 1 - \sin\varphi$ for normally consolidated soil.

This primary stress state causes a violation of the yield criterion at integration points below a certain depth in the soil. At these points, the internal variables are adapted accordingly.

The time-dependent behavior of the soil, characterized by the viscosity η, is chosen such that an interaction between the soil and the hydrating shotcrete lining can be observed in the course of the numerical simulation.

The material properties employed for the shotcrete are the same as were used in the previous example (see Section 5.1). They are given, e.g., in Table 5.3.

The structural model chosen for the numerical simulations is shown in Figure 5.27, where symmetry conditions are exploited. For this academic example, plane strain conditions are applied in order to obtain numerical results for which the effects of the two elastic laws on the structural response are clearly distinguishable. Accordingly, the plane mesh consisting of 1766 finite elements is depicted in Figure 5.28. However, in consequence of the plane strain assumption, the support effect of the tunnel face is not accounted for. Therefore, the computed displacements are expected to be greater than for a 3D computation. For more realistic numerical results, a 3D analysis has to be performed.

The excavation of the soil is modelled using a technique already applied in [70] and in Section 5.1, where the thickness of the excavated elements, and, hence, their dead load, is continuously reduced in the course of the excavation process, until a remaining thickness of 0.1% of the initial thickness is reached. The subsequent installation of the shotcrete lining is modelled by changing the material properties of the respective elements from
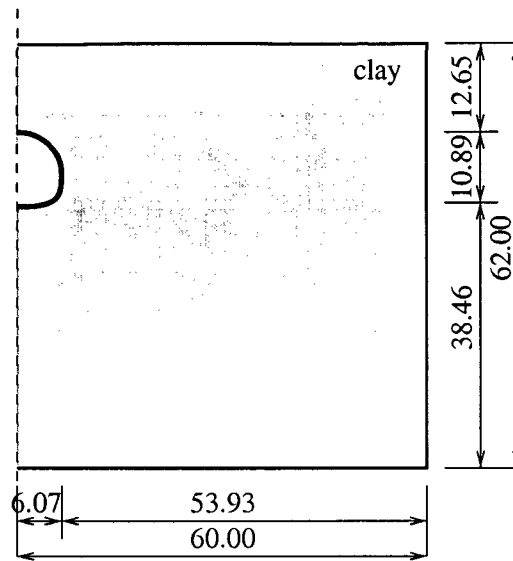
Figure 5.27: Numerical simulation of the tunnel excavation in cohesive soil: geometric dimensions (in [m]) of the structural model
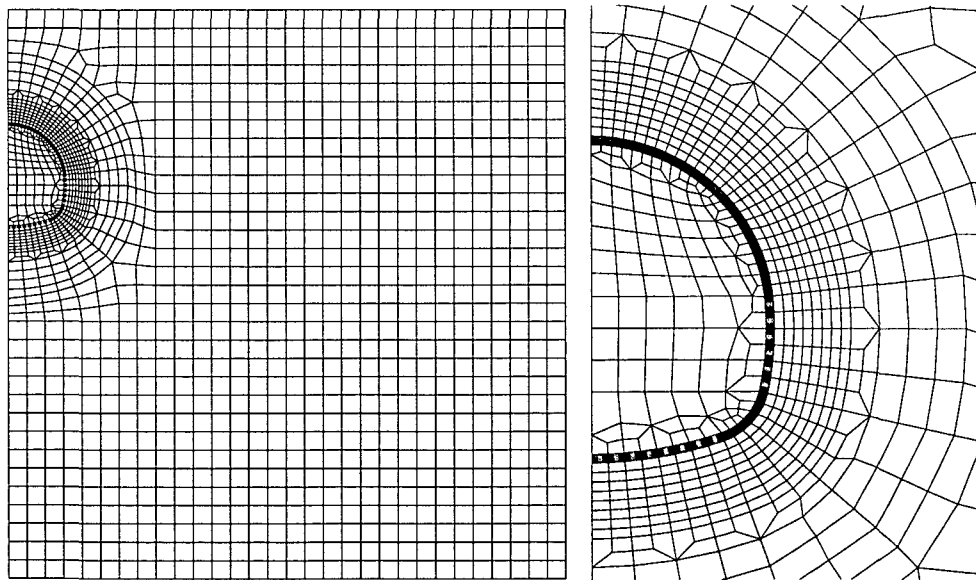

Figure 5.28: Numerical simulation of the tunnel excavation in cohesive soil: FE mesh consisting of 1766 finite elements

soil to shotcrete at the time instant of this installation. First of all, the numerically obtained displacements depicted in Figure 5.29 show that for the analysis using the elastic law (LE) the inward displacements of the soil surrounding the tunnel are slightly smaller compared to the displacements resulting from the analysis using the nonlinear linear elastic law (NLE). The reason for the smaller displacements from the LE analysis is the constant
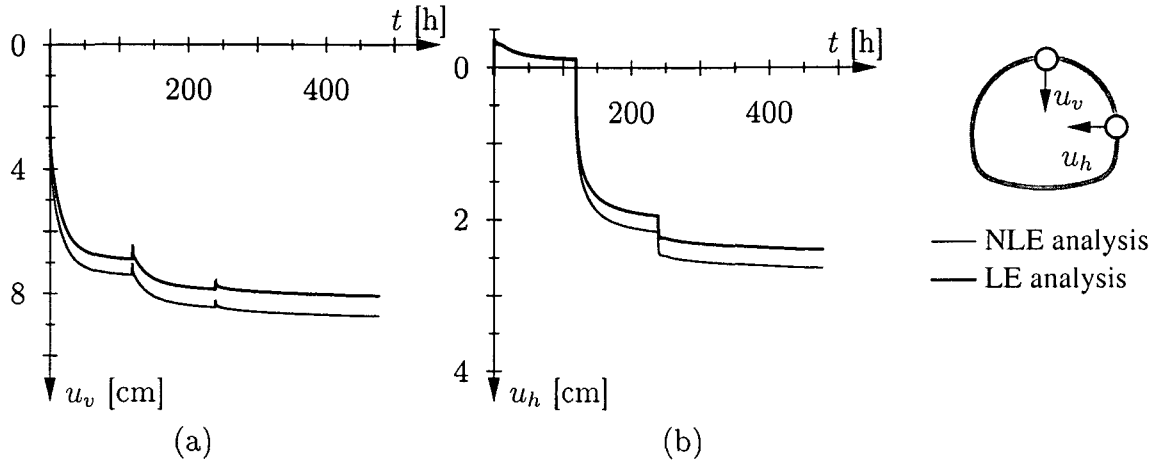

Figure 5.29: Numerical results from the simulation of the tunnel excavation in cohesive soil: evolution of (a) vertical and (b) horizontal displacements of excavation for NLE and LE analysis

stiffness of the soil. Estimation of the LE stiffness from the NLE stiffness at a depth of 20 m naturally overestimates the structural stiffness fow lower depths. Hence, this results in a stiffer structural response around the tunnel compared to the analysis using a variable soil stiffness. However, the rather soft soil is responsible for the relatively large amount of displacements. Here, the heading excavation, the lining installation, and the following waiting period are responsible for about 75% of the final crown settlements. Bench and invert excavation yield first a heave of the crown, because of rapid inward displacement of the bench, which leads to a change of the shape of the hardening shotcrete lining. Concerning the horizontal displacement of the future location of the bench, the initially observed outward bench displacement results from the delayed lining installation. The lining installation of the heading stabilizes the excavated cross-section, and, in the following, creep of soil leads to inward bench displacement. The subsequent excavation steps yield an inward bench displacement because of the applied lateral earth pressure coefficient. However, the difference of the displacements obtained from NLE and LE analysis is less than 10%. Such relative differences are generally less important in soil mechanics.

Figure 5.30 displays the overall final deformation of the shotcrete lining as well as the relative deformation of the three parts of the shotcrete lining between the individual lining installation and the next excavation step. As can be seen from Figure 5.30(a) and (b), the deformation behavior according to the NLE and the LE analysis is very similar. Overall convergence of displacements can be observed, a large settlement of the heading and also
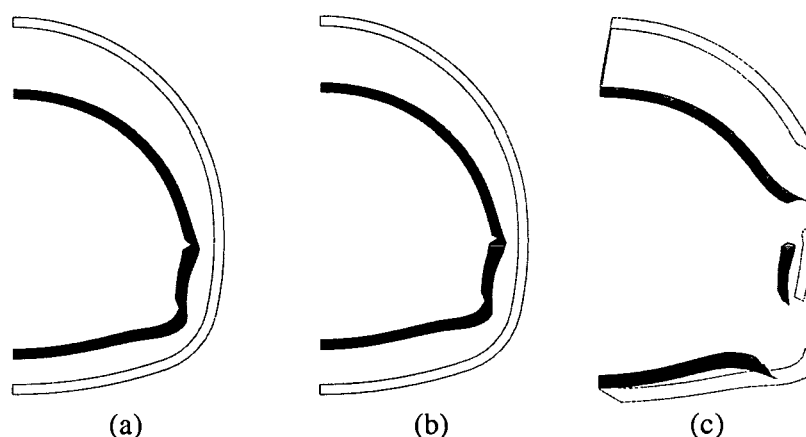
Figure 5.30: Numerical results from the simulation of the tunnel excavation in cohesive soil: final deformation of the entire shotcrete lining for (a) NLE and (b) LE analysis (25-fold magnification), and (c) relative displacement of the heading, the bench, and the invert between the lining installation and the start of next excavation step (heading, invert: 50-fold magnification, bench: 25-fold magnification)

a considerable heave of the invert. The inward displacement at the bench is comparably small. Figure 5.30(c) shows the relative deformation of the three parts of the shotcrete lining between their installation and the next excavation step. As is cleary observable from the magnified deformation plots, there is a change of curvature at the footing of the heading, in the bench and in the outer part of the invert. The curvature change at the footing of the heading indicates a weak heading footing, bearing little resistance to the inward moving soil. Additionally, the downward movement of the entire heading during the creep process shows that the complete support subsides gradually into the soft soil[3].

Subsequently, the excavation of the benches leads to a vertical shortening, resulting from overall soil settlements. The inward movement of the shotcreted bench is accompanied by an overall change of curvature of the lining, assigning more or less uniform inward soil movement. After excavation and installation of the invert lining, another change of curvature, now in the outer part of the invert, is observed, resulting from the initially small stiffness of the invert lining[4].

---

[3]In practical applications, broadening of the footings is an adequate means to restrict unfavorable subsidence and curvature. However, such practical remedies are not the scope of the present numerical study, and, hence, they are not considered here.

[4]The overall deformation behavior suggests that the region at the footing of the heading and the outer invert require observation concerning their soundness (see also [92]). However, the applied simulation suffers from major shortcomings as regards structural stability: it neither accounts for nonlinear geometric formulation, nor for localized failure. Hence, an overestimation of the structural integrity of the tunnel is possible (see [86]). Especially, when considering the low overburden in this example, with $H/D \approx 1.0$, the development of a sufficiently strong protection zone may not be guaranteed (see also [92]). Nevertheless, structural stability shall be assumed herein.

The regions of the considerable lining deformation are identical to the regions where plastification of the lining occurs, as is illustrated in Figure 5.31. It was observed that the
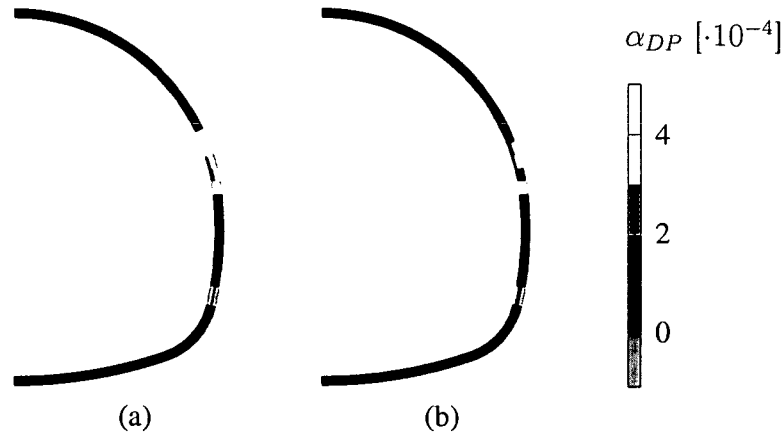

$$\alpha_{DP} \ [\cdot 10^{-4}]$$

Figure 5.31: Numerical results from the simulation of the tunnel excavation in cohesive soil: distribution of internal hardening variable α_{DP} in shotcrete lining for (a) NLE and (b) LE analysis

plastification of the lining occurs only during the first 2.25 hours after lining installation. Afterwards the lining behaves elastic because of increasing stiffness and material resistance in consequence of hydration. The amount of plastification in form of hardening is generally small, as $\alpha_{DP} < \alpha_{DP,m} \approx 1 \cdot 10^{-3}$ in the major part of the structure. Only at the footing of the heading and partly at the footing of the bench, $\alpha \geq \alpha_{DP,m}$, and, hence, ideally plastic material bahavior is obtained. However, the distribution of the internal variable α_{DP} for shotcrete corroborates the above presumption that the effect of the elastic law of the soil on the structural response is small.

According to similar deformation results obtained from NLE and LE analysis, the computed axial forces in the lining are almost identical for both analyses (see Figure 5.32). However, in agreement with the larger crown displacements obtained from NLE analysis (see Figure 5.29(a)), the axial forces in the crown of the lining resulting from the NLE analysis are slightly greater. The general trend of the evolution of the axial forces is a steep increase from the time of installation for about 24 hours. Then, there is a smooth reversal of the loading, which decreases with time. This initial loading and the subsequent unloading of the lining with the smooth transition in between is the result of two counteracting processes: First, the increase in the compressive forces is a result from the inward creep deformations of the soil. This creep process fades out with time. The counteracting process is creep and shrinkage of shotcrete, with creep starting about 0.50 hours after shotcreting and shrinkage starting about 13 hours after shotcreting. Creep and shrinkage strains increase with time. However, the unloading effects of shotcrete creep and shrinkage are not visible until the large soil deformation rate towards the opening decreases. Then they lead to a visible reduction of the compressive forces in the lining. Anyway, the largest compressive force of $n_\varphi \approx 0.9$ MPa is obtained at the shoulder at $t = 240$ h, i. e.,
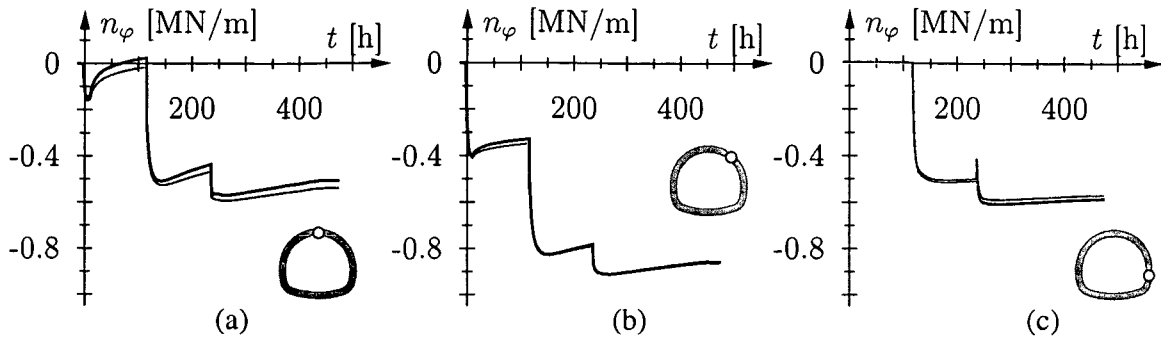
Figure 5.32: Numerical results of simulation of the tunnel excavation in cohesive
soil: evolution of axial forces in the shotcrete lining at (a) the crown, (b) the
shoulder, and (c) the bench, for NLE and LE analysis

after installation of the invert. The load-carrying capacity of the shotcrete at that time is
$f_{c,t=240} \cdot h = 31.2$ MPa $\cdot 0.3$ m $= 9.36$ MPa, resulting in a loading degree of 10% of the
load-carrying capacity of the lining.

Finally, the evolution of plastic zones in the soil in consequence of the excavation is shown
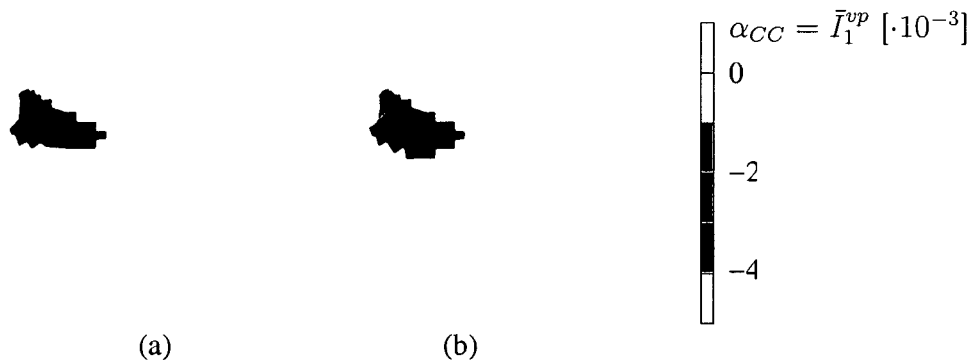in Figure 5.33. In this example, the soil compacts during the excavation process, and soil

Figure 5.33: Numerical results from the simulation of the tunnel excavation in
cohesive soil: distribution of internal hardening variable α_{CC} in the soil for
(a) NLE and (b) LE analysis

hardening is observed at the bench of the tunnel. Also some minor softenina,g accompanied
by dilation, occurs at the crown region of the tunnel. As follows from comparison of
Figure 5.33(a) and (b), the LE analysis predicts more plastic response with respect to the
magnitude of the hardening variable, i.e., the volumetric viscoplastic strains, as well as
with respect to the size of the plastic zones. For a depth larger than 20 m, the LE analysis
gives more plastification, as the elastic soil stiffness is smaller than the respective NLE
stiffness. The plastic zones become slightly bent downward, and with increasing distance
from the opening, they tend to be horizontal. Here, the downward direction results from
subsidence of the footing of the heading.

To sum up, the numerical results presented indicate that the influence of the elastic law in elasto-viscoplastic analysis of tunnel excavation processes is very small. The difference in the displacements is about 10%. There were also minor differences in the evolution of the plastic zones and the amount of plastification in the soil. As regards the shotcrete lining, the axial lining forces and, hence, the plastic behavior, are hardly effected by the choice of the elastic law for the soil.

5.2.2 Study of the effect of the elastic law with respect to variations of the primary soil conditions

It is well known that the initial geological conditions, such as the initial stress state in the soil or the degree of overconsolidation of the soil, have an essential influence on the structural response in the excavation process. E.g., a large lateral earth pressure coefficient, K_0, is likely to ensure a more stable protection zone around the excavation. Also, the degree of overconsolidation effects the soil plastification resulting from the excavation. Another important soil characteristics is the viscosity, because it controls the amount of interaction between the hardening shotcrete and the creeping soil.

The following sections contain numerical studies of tunnel excavations under different primary soil conditions and with application of a non-linear and linear elastic law for the elasto-viscoplastic behavior of the cohesive soil.

5.2.2.1 Effect of coefficient of lateral earth pressure, K_0

The coefficient of lateral earth pressure, K_0, expresses a qualitative assumption about the magnitude of the horizontal earth pressure in the soil in relation to the vertical pressure. For practical purposes, this coefficient is commonly assumed as $K_0 = 1 - \sin \varphi$ according to Jaky [43] for normally consolidated soil. In order to account for a specific geologic history of the soil under consideration, K_0 is chosen in a different manner. Especially for tunnel construction processes near the surface, the horizontal stress state in the soil is essential for the stability of the tunnel construction. Obviously, for a small value of K_0, the protection zone which develops after the excavation in the soil surrounding the opening is weaker as compared to the one that develops for a larger value of K_0.

However, in view of the examined Cam-Clay model, consideration of different lateral earth pressure coefficients results in different locations of the initial stress state in the stress space (see Figure 5.34). Therefore, further stress redistributions in consequence of the excavation are expected to yield different elasto-viscoplastic behavior as the initial direction of the plastic strain rate $\dot{\varepsilon}^p = \dot{\gamma} \, \partial_\sigma f_{CC}$ will be different. In this example, three different values of K_0, $K_0 \in (0.1; 0.5; 0.9)$, are investigated.

Depending on the assumed lateral earth pressure coefficient, the values of the elastic constants for the linear elastic model were determined according to the elastic tangent modulus obtained from the nonlinear elastic model for the respective primary stress state in 20 m
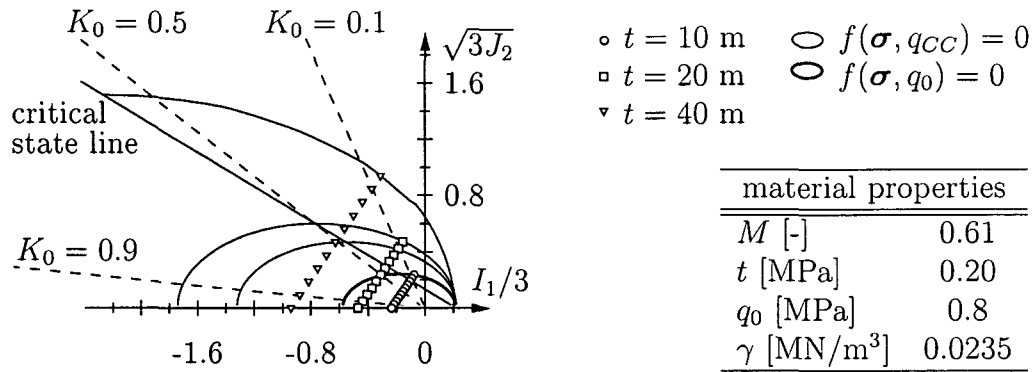
Figure 5.34: Numerical study on the effect of the elastic law for varying K_0: lines of initial stress states in the soil for different values of K_0; exemplary stress states for selected depths t depending on K_0; selected inital yield loci $f_{CC} = 0$

linear elastic material parameters employed for cohesive soil			
	coefficient of lateral earth pressure K_0		
	0.1	0.5	0.9
compression modulus, K [MPa]	93	91	101
shear modulus, G [MPa]	47	53	62
Young's modulus, E [MPa]	120	133	155
Poisson's ratio, ν [-]	0.28	0.26	0.25

Table 5.5: Numerical study on the effect of the elastic law for varying K_0: linear elastic material parameters employed for cohesive soil, depending on the lateral earth pressure coefficient K_0

depth. The obtained elastic parameters are listed in Table 5.5. It is worth noting that a lateral earth pressure deviating from the normally consolidated state may also result in changes of the values of other material parameters, e.g., of the ones describing the compressive behavior. However, for this numerical study, changes of other material properties are disregarded for the sake of compararability of the obtained numerical results.

The numerically obtained crown and bench displacements are illustrated in Figure 5.35. As suggested by intuition, and confirmed by Figure 5.35(b), the coefficient of lateral earth pressure, K_0, determines the amount of inward bench displacement of the soil surrounding the excavation, i.e., the greater the value of K_0, the larger the amount of the inward bench displacement (see also Figure 5.36). For small K_0, divergence is observed. As regards
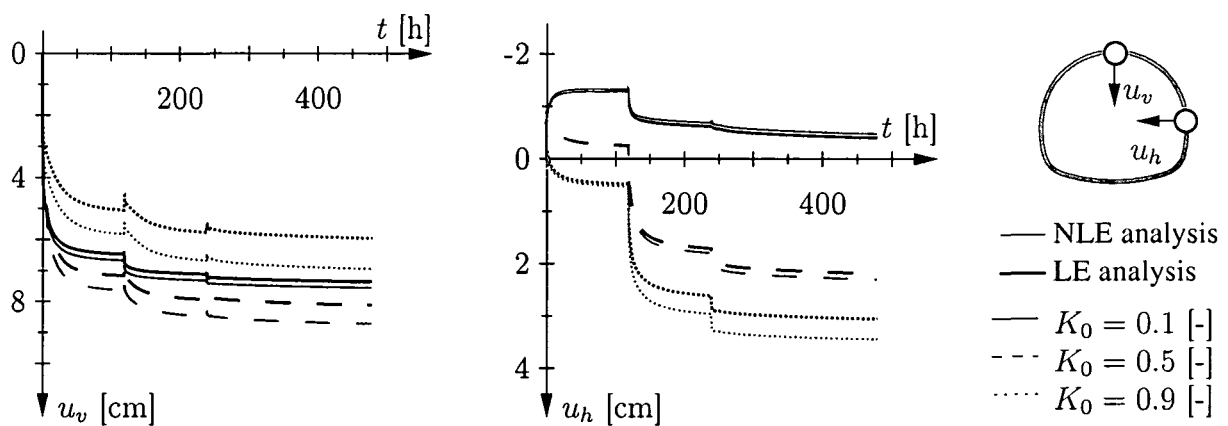

Figure 5.35: Numerical study on the effect of the elastic law for varying K_0: evolution of (a) vertical and (b) horizontal displacements of the excavation for different K_0 and NLE and LE analyses
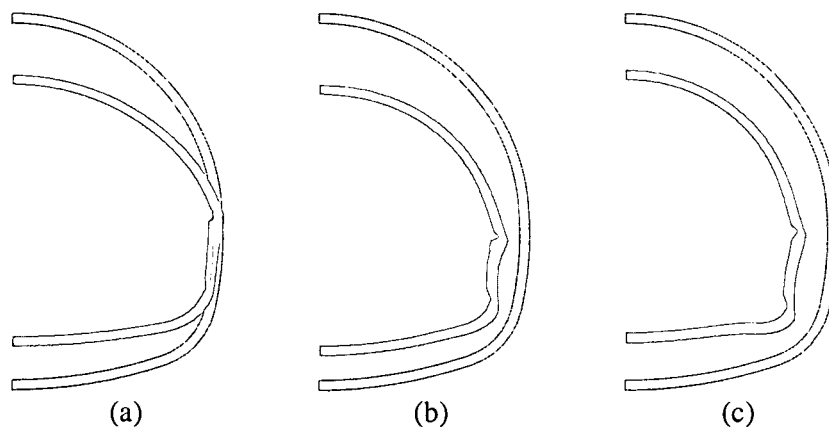

Figure 5.36: Numerical study on the effect of the elastic law for varying K_0: final deformation of the shotcrete lining for NLE analysis and (a) $K_0 = 0.1$, (b) $K_0 = 0.5$, and (c) $K_0 = 0.9$

the crown settlements (see Figure 5.35(a)), first, globally larger settlements, followed by smaller settlements, can be observed for increasing K_0. This change of trend results from the change of global viscoplastic behavior of the soil (see Figure 5.37): whereas a small
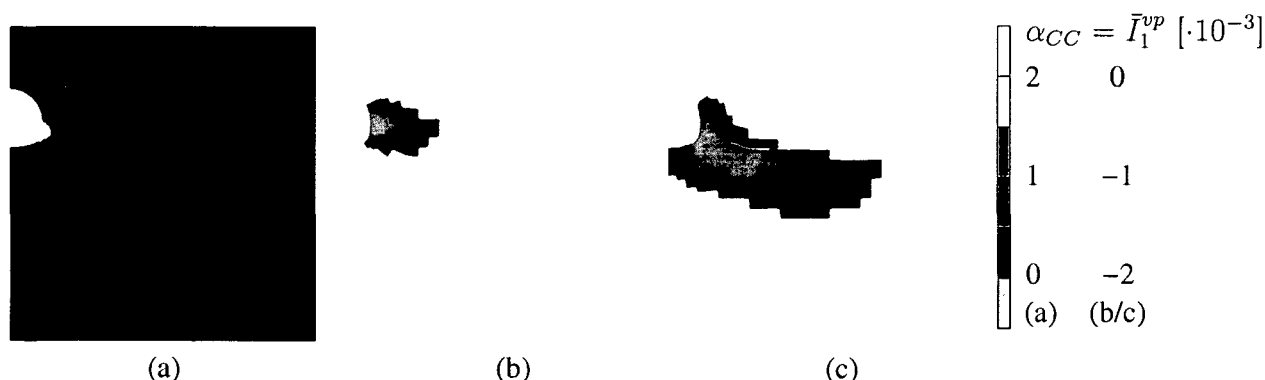

Figure 5.37: Numerical study on the effect of the elastic law for varying K_0: distribution of internal hardening variable α_{CC} in soil for NLE analysis and (a) $K_0 = 0.1$, (b) $K_0 = 0.5$, and (c) $K_0 = 0.9$

value of K_0 leads to soil softening accompanied by plastic dilation, a large value of K_0 yields soil hardening accompanied by plastic compaction. This results from the locations of the initial stress states with respect to the location of the *critical state line* of the Cam-Clay model (see Figure 5.34). Small values of K_0 correspond to stress states located above the *critical state line*, whereas large values of K_0 are associated with stress states located below the *critical state line*. Hence, stress-redistribution in consequence of the excavation most likely results in strain-softening for small values values of K_0 and in strain-hardening for large values of K_0.

Additionally, the magnitude of K_0 effects the direction of propagation of the plastic zone in the soil: in all cases the plastic zone initiates at the tunnel bench; for small values of K_0 the evolution is directed downwards, whereas its orientation is rather horizontal for larger values of K_0, because of the increasing resistance of the soil against the heading subsidence (see Section 5.2.1). Furthermore, with increasing value of K_0 the respective initial stress states are characterized by increasing proximity to the hydrostatic axis. Thus, the plastic response from the redistribution of stress is also characterized by greater proximity to the hydrostatic axis. Consequently, as regards the present example, $\dot{\varepsilon}^p = \dot{\gamma} \, \partial_\sigma f_{CC} \rightarrow \dot{\gamma} \partial_p f_{CC} = \dot{\alpha}_{CC}$ for increasing K_0.

As regards the compressive forces in the lining, illustrated in Figure 5.38, they increase with increasing K_0, resulting from the increased inward soil movement. As the heading support to a large extent withdraws from the loading for $K_0 = 0.1$, the forces are dwismall low in the entire lining. For $K_0 = 0.5$ and $K_0 = 0.9$, the largest forces occur at the shoulder because of the encountered deformation of the heading.

Resulting from the larger lining forces obtained for increasing values of K_0, there is also more plastification of the lining (see Figure 5.39). Again, during the first rapid increase of
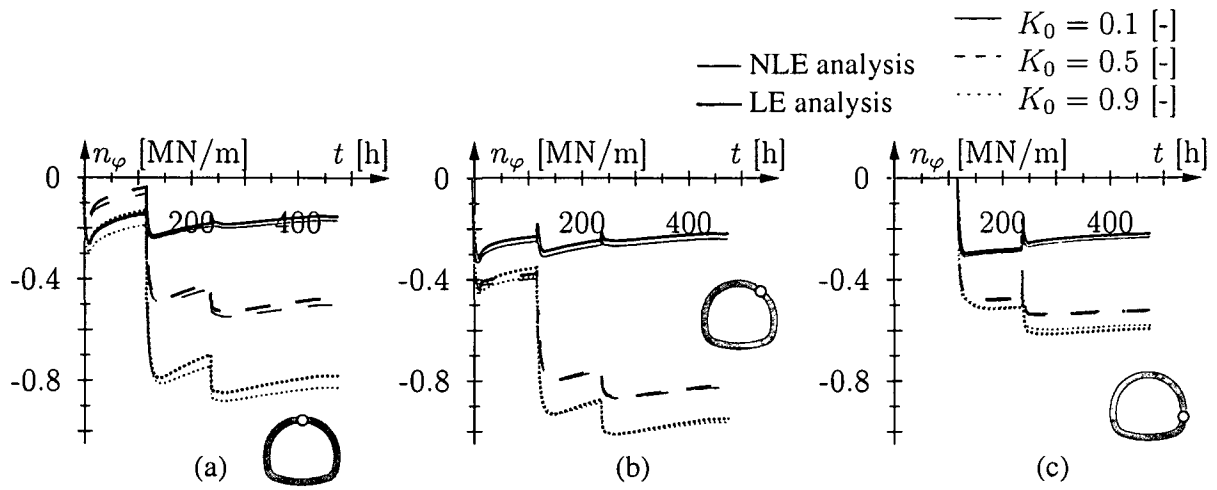
Figure 5.38: Numerical study on the effect of the elastic law for varying K_0: evolution of axial forces in the shotcrete lining at (a) the crown, (b) the shoulder, and (c) the bench for different values of K_0 and NLE and LE analysis
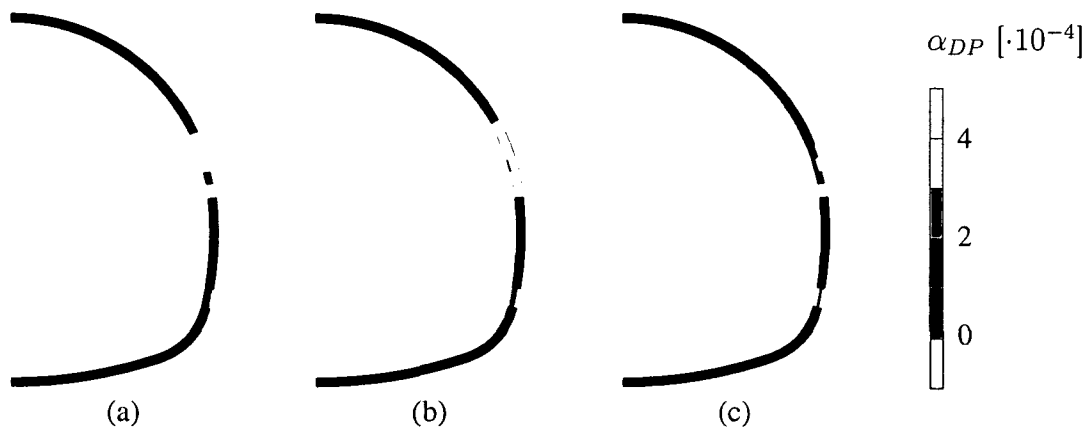

Figure 5.39: Numerical study on the effect of the elastic law for varying K_0: distribution of the internal hardening variable α_{DP} in the shotcrete lining for NLE analysis and (a) $K_0 = 0.1$, (b) $K_0 = 0.5$, and (c) $K_0 = 0.9$

the lining forces, plastic deformation of the lining occurs (see Figure 5.39) in the regions with the largest lining distortion. But again, plastification is generally small and remains in the major parts of the structure in the hardening regime.

However, comparing the numerical results obtained from NLE and LE analysis, a clear trend for an increasing influence of the elastic law with increasing K_0 can be observed for the displacements (see Figure 5.35). For $K_0 = 0.9$, the difference between the results from NLE and LE analysis is 15%. As regards the crown displacements, this difference is even greater than the difference between the NLE analyses for $K_0 = 0.1$ and $K_0 = 0.9$. Hence, as regards the crown settlements, the elastic law gains importance with increasing lateral earth pressure coefficients.

However, the lining forces, and, hence, the plastic zones in the shotcrete lining are hardly influenced by the choice of the elastic law (see Figure 5.38).

5.2.2.2 Effect of overconsolidation ratio OCR

For fine-grained soil like clay, some former compaction of particles in consequence of pre-consolidation, e. g., from additional soil layers or glaciers, remains. This compaction is accompanied by an increase of strength. Hence, subsequent loading – unless it is close to hydrostatic loading – is most likely to result in dilation of the soil accompanied by a loss of strength. In critical state soil mechanics, such a soil is called *overconsolidated.* Consequently, a *normally consolidated* soil refers to soil with no former preconsolidation, tending to compaction and strength increase during loading. Interpretation of the described soil behavior in terms of elastoplasticity means that *overconsolidated* soil shows

1. an initial elastic response for subsequent loading, and

2. plastic dilatant behavior for continued loading.

Accordingly, *normally consolidated* soil shows initial plastic response and plastic compaction under loading.

Essentially, the employed Cam-Clay model is able to model both – plastic compaction associated with hardening and plastic dilation associated with softening. However, the predicted material response depends on

- the location of the initial stress state in the stress space with respect to the location of the *critical state line* (see Section 5.2.2.1),

- the stress path followed in consequence of loading, and

- the size and the location of the initial yield surface.

So far, the primary state of the soil was assumed such that the initial stress state of each integration point was located either inside the elastic domain, with $f_{CC}(\sigma, q_0) < 0$, or, in case of violation of the yield criterion, on the yield surface, with $f_{CC}(\sigma, q_{CC} > q_0) = 0$.

This assumption corresponds to preconsolidated soil for a depth smaller than the limiting depth, characterized by $f_{CC}(\boldsymbol{\sigma}, q_0) = 0$, and to non preconsolidated soil below this limiting depth (see Figure 5.40(a)).
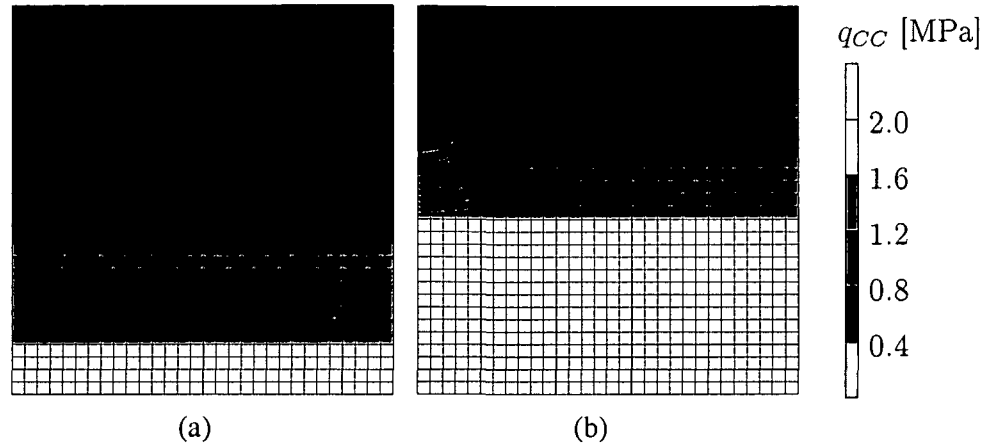

Figure 5.40: Numerical study on the effect of the elastic law for varying OCR: primary state of the internal variable q_{CC} for (a) normally consolidated soil and (b) overconsolidated soil with $OCR = 1.5$ (for $q_0 = 0.8$ MPa)

Now, an *overconsolidation ratio* OCR shall be introduced, referring to the distance between the initial stress state and the initial yield surface of each integration point, such that $f_{CC}(\boldsymbol{\sigma}, OCR \cdot q_{CC}) < 0$, if $f_{CC}(\boldsymbol{\sigma}, q_{CC}) = 0$. Hence, during the tunneling process, initially, elastic behavior will occur. In this example, $OCR \in (1.1; 1.5; 2.0)$ is chosen. For $OCR = 1.5$, the adopted distribution of the initial size of the yield locus is depicted in Figure 5.40(b).

For the sake of simplicity, the lateral earth pressure coefficient remains as $K_0 = 1 - \sin\varphi$ throughout this section, although deviation from normally consolidated state changes is supposed to change K_0.

The obtained numerical results concerning the crown settlement and the bench displacement are depicted in Figure 5.41. Expectedly, as a consequence of the great elastic stiffness of the soil and of the increasing distance of the stress points from the yield surface, the inward displacements of the soil become smaller with increasing overconsolidation ratio (see Figures 5.41 and 5.42). Hence, there are differences of the displacements up to about 35% for variations of the OCR (see Figure 5.41). Also the differences of NLE and LE analyses are noteworthy as amounting, e. g., to 10-20% for the crown settlements (see Figure 5.41(a)).

Soil deformation is mainly accompanied by hardening at the bench for $OCR = 1.1$ and $OCR = 1.5$, and softening at the bottom part of the bench and at the shoulder for $OCR = 2.0$ (see Figure 5.43). Hence, with increasing OCR, the stress-redistribution in consequence of the excavation leads to a reduction of hardening and a dominance of softening, as the stress paths are directed to the strain-softening side of the Cam-Clay
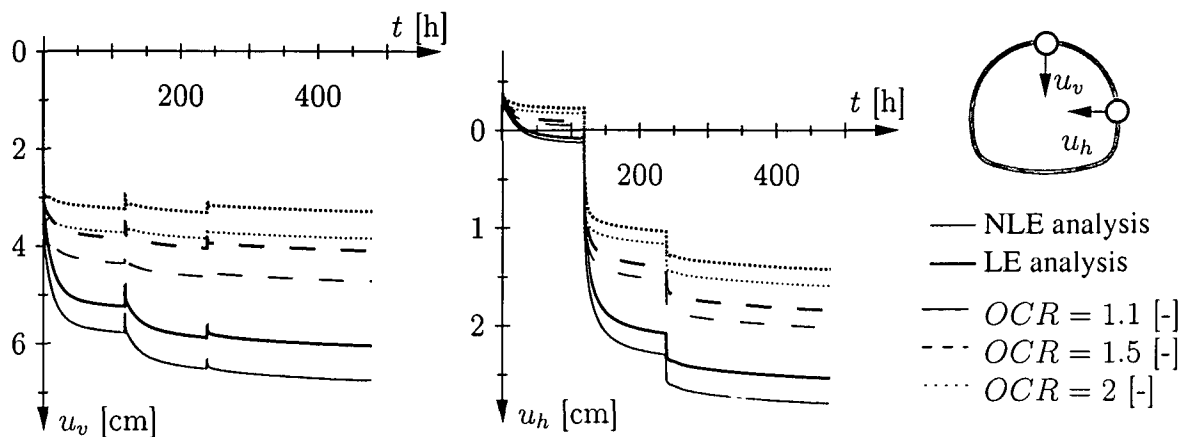
Figure 5.41: Numerical study on the effect of the elastic law for varying OCR: evolution of (a) vertical and (b) horizontal convergence of the excavation with a shotcrete lining for NLE and LE analysis and (a) $OCR = 1.1$, (b) $OCR = 1.5$, and (c) $OCR = 2$
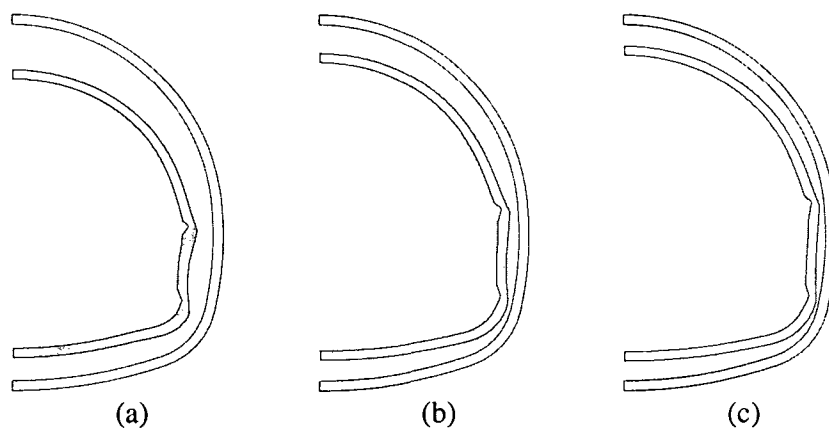

Figure 5.42: Numerical study on the effect of the elastic law for varying OCR: final deformation of the shotcrete lining for NLE analysis and (a) $OCR = 1.1$, (b) $OCR = 1.5$, and (c) $OCR = 2$

loading surface. Resulting from the smaller displacements obtained for larger OCR, the
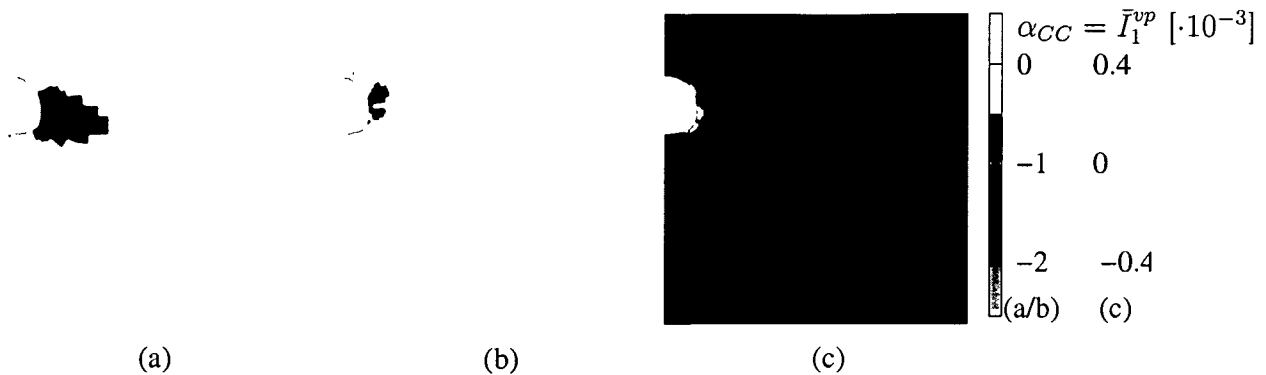

Figure 5.43: Numerical study on the effect of the elastic law for varying OCR:
distribution of the internal hardening variable α_{CC} in soil for NLE analysis
and (a) $OCR = 1.1$, (b) $OCR = 1.5$, and (c) $OCR = 2$

axial forces in the lining are smaller (see Figure 5.44). However, the final loading degree
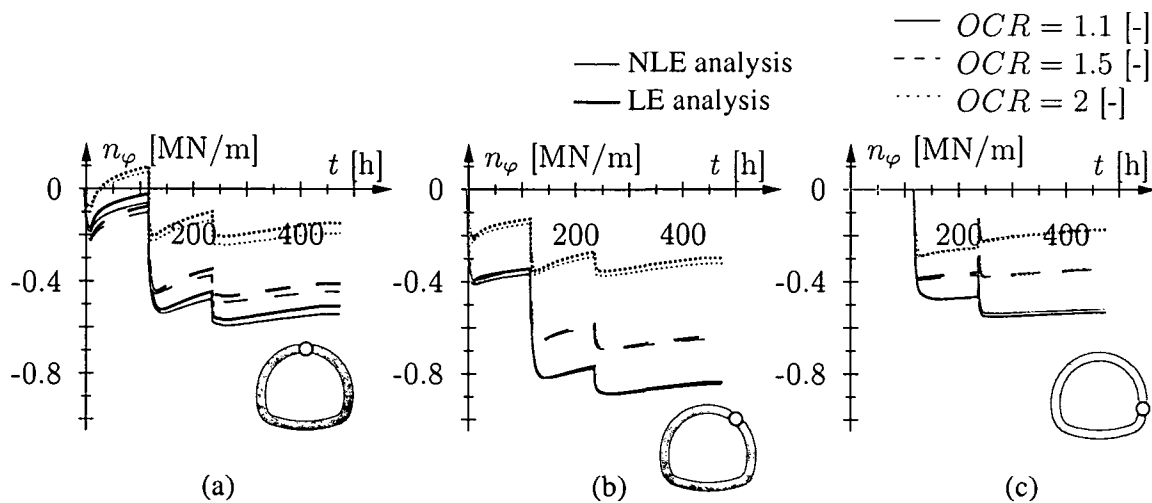
Figure 5.44: Numerical study on the effect of the elastic law for varying OCR:
evolution of axial forces in the shotcrete lining at (a) the crown, (b) the
shoulder, and (c) the bench for different OCR and NLE and LE analysis

of the lining is low.

Associated with larger forces obtained for smaller OCR, the amount of plastification of
the lining is also higher as regards both magnitude and size (see Figure 5.45).

This example confirms that the impact of the elastic law is most pronounced in the soil de-
formation. The influence of this law increases with increasing OCR. The relative difference
between the crown settlements for NLE and LE analysis may reach a value of 20%.
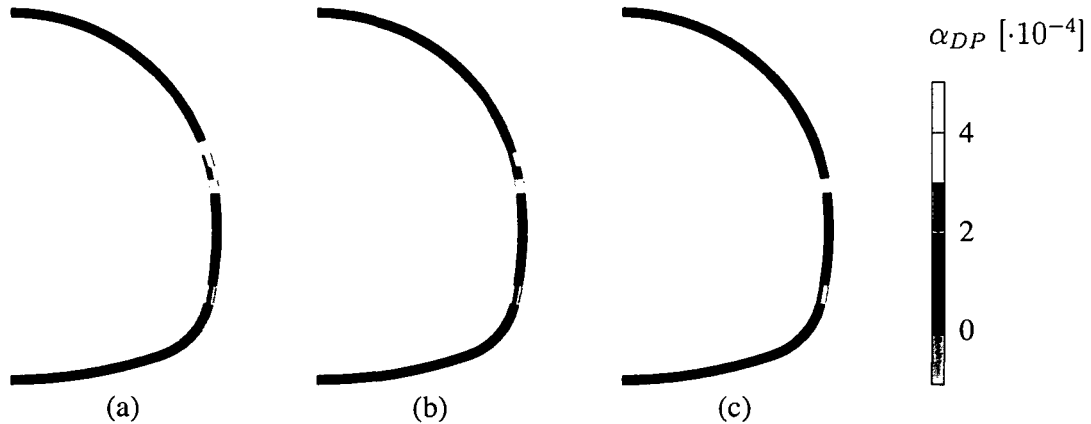
Figure 5.45: Numerical study on the effect of the elastic law for varying OCR: distribution of the internal hardening variable α_{DP} in the shotcrete lining for the NLE analysis and (a) $OCR = 1.1$, (b) $OCR = 1.5$, and (c) $OCR = 2$

5.2.2.3 Effect of soil viscosity η

The global effect of the viscosity of the soil on tunneling is evident: the greater the viscosity, the slower the soil is creeping towards the tunnel opening. The basic interaction between the hydrating shotcrete lining and the creeping soil is also clear: on the one hand, very fast creeping soil loads the hardening shotcrete lining when its strength and stiffness are still rather small, leading to large tunnel displacements and a small degree of loading of the lining. On the other hand, very slow creeping soil loads the hardening shotcrete lining over a longer period, i.e., loading still occurs when a certain strength and stiffness of the lining have already developed. Hence, the slow creeping ground encounters increasing resistance from the hardening shotcrete lining. Hence, tunnel displacements are expected to be small. This interaction was already studied and described in [35]. Furthermore, a longer lasting creep process is expected to result in greater loading of the lining. This is also documented in [35] for the case of disregard of chemical shrinkage and of creep of shotcrete.

However, the focus of the present study is the influence of the elastic law of the soil for varying soil viscosities. The following investigation is performed for $\eta \in (20; 200; 2000)$ [MPa·h]. The chosen viscosities can be related to creep times $\tau = \eta/E$, with $E \approx 140$ MPa, and thus, $\tau \in (0.14, 1.4, 14.0)$ [h]. According to [35], the resulting creep times are in a range where an interaction between creep of soil and hardening of shotcrete can be observed.

The numerically obtained crown and bench displacements (see Figure 5.46) as well as the overall deformation of the shotcrete lining (see Figure 5.47) show the expected trend of the deformations: for slower creep processes, the overall displacements are smaller. However, Figure 5.46 clearly shows that the differences of about 10% resulting from use of different elastic laws are small as compared to the differences obtained from variations of the soil viscosities.

According to the obtained amount of the soil deformation, the plastification of the soil is
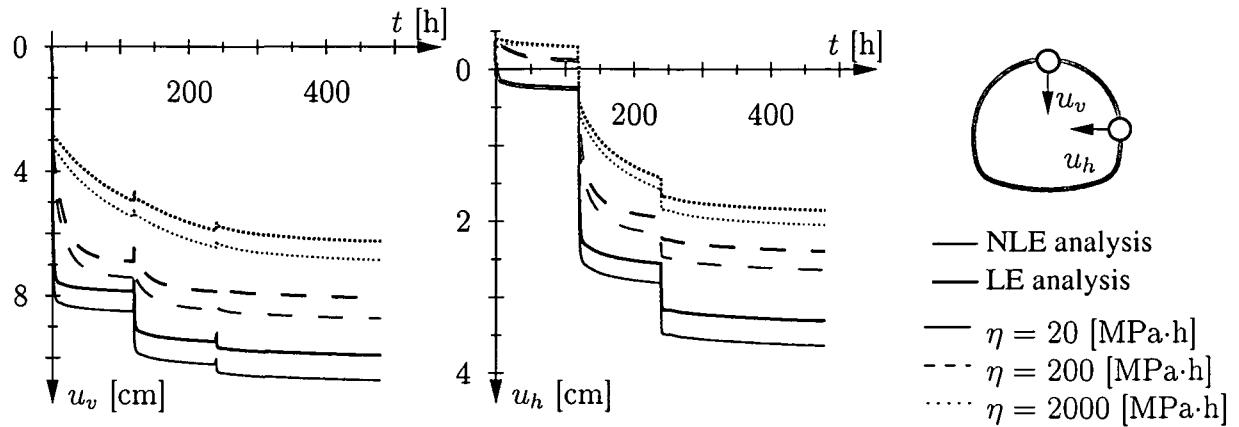
Figure 5.46: Numerical study on the effect of the elastic law for varying η: evolution of (a) the vertical and (b) the horizontal convergence of the excavation with shotcrete lining, for NLE and LE analysis and (a) $\eta = 20$, (b) $\eta = 200$, and (c) $\eta = 2000$ [MPa h]

Figure 5.47: Numerical study on the effect of the elastic law for varying η: final deformation of the shotcrete lining, for NLE analysis and (a) $\eta = 20$, (b) $\eta = 200$, and (c) $\eta = 2000$ [MPa h]

smaller for slower creep processes (see Figure 5.48), because the slow movement of the soil towards the opening is restrained by an already rather stiff shotcrete lining.

Figure 5.48: Numerical study on the effect of the elastic law for varying η: distribution of the internal hardening variable α_{CC} in the soil, for NLE analysis and (a) $\eta = 20$, (b) $\eta = 200$, and (c) $\eta = 2000$ [MPa h]

The same argument applies to plastification of the shotcrete lining, which is depicted in Figure 5.49. First of all, plastification of the shotcrete lining only takes place within the first
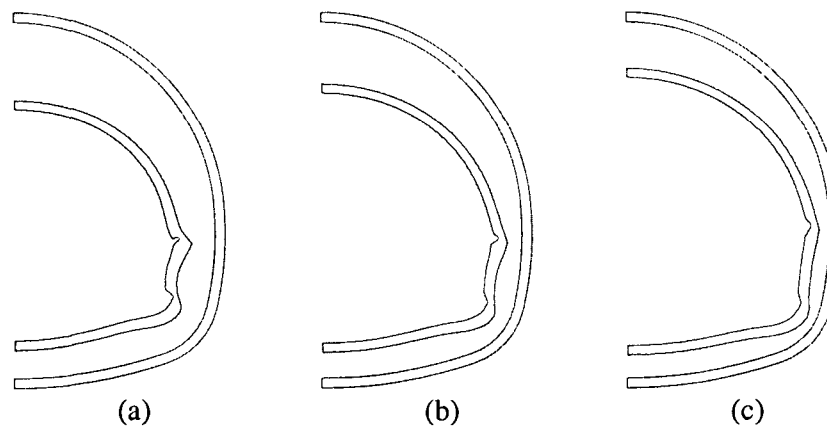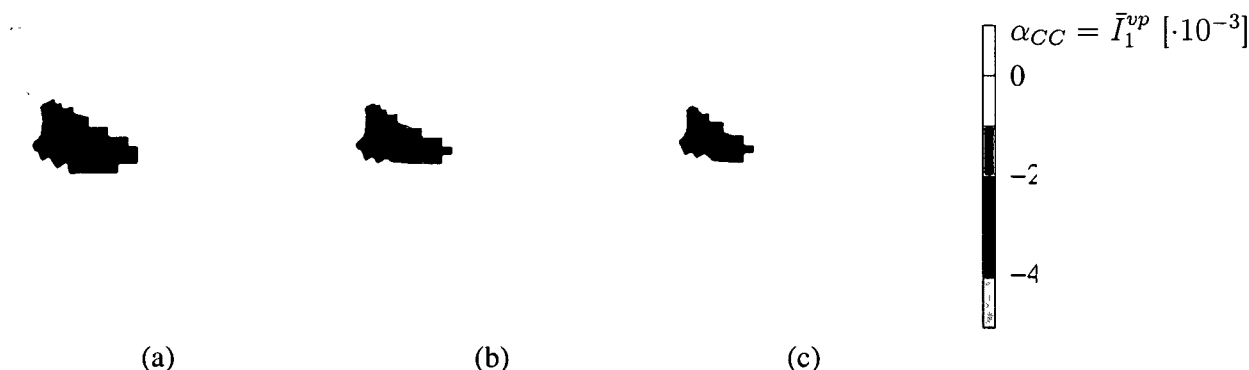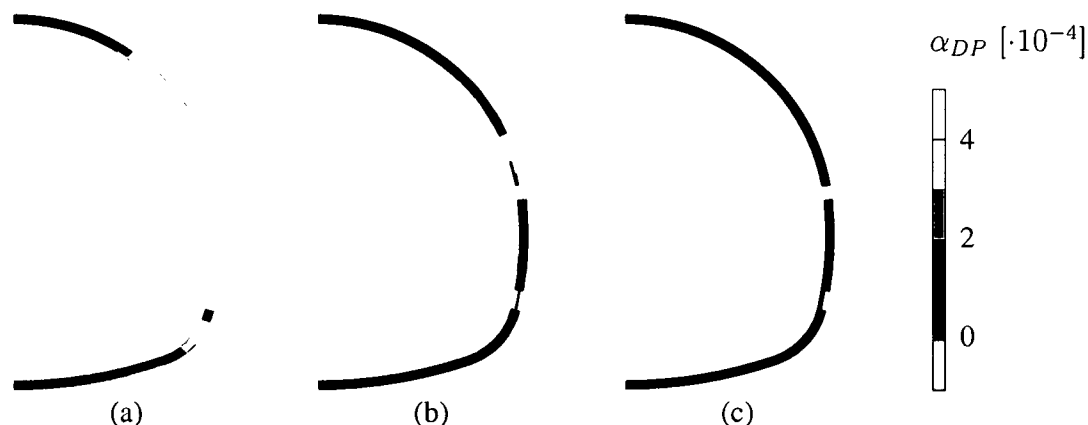

Figure 5.49: Numerical study on the effect of the elastic law for varying η: distribution of the internal hardening variable α_{DP} in the shotcrete lining for NLE analysis and (a) $\eta = 20$, (b) $\eta = 200$, and (c) $\eta = 2000$ [MPa h]

hour after the installation of the lining. During this short period, the slowly moving soil causes less damage to the young shotcrete compared to soil that is moving fast. And, since the loading of the lining, in general, is small, elastic behavior is encountered afterwards.

Finally, the evolution of the axial forces in the lining show the dependence on the soil viscosity (see Figure 5.50): for a small viscosity, the creep and shrinkage strains in the lining visibly reduce the large forces, which quickly developed after installation of the lining. For a large viscosity, lining forces evolve slowly, and creep and shrinkage strains in the shotcrete
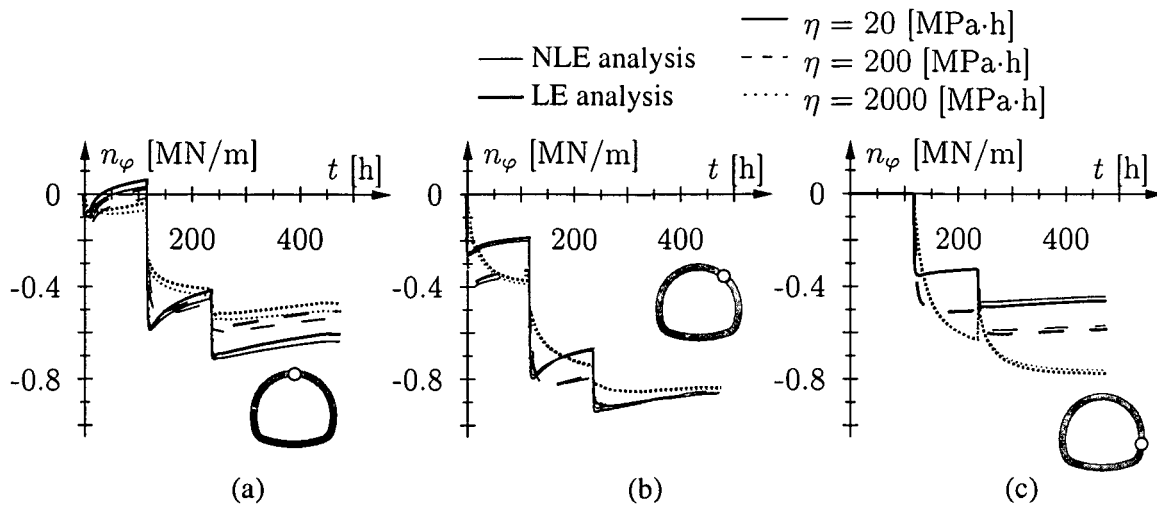
Figure 5.50: Numerical study on the effect of the elastic law for varying η: evolution of axial forces in the shotcrete lining at (a) the crown, (b) the shoulder, and (c) the bench for different η and NLE and LE analysis

do not lead to visible unloading. Referring to Section 5.1, the loading effect from the long lasting creep process dominates the counteracting unloading effect from shotcrete creep and shrinkage within the considered time interval of the numerical simulation. However, as regards the staggered excavation, an interesting observation can be made: at the crown and the shoulders, there is a trend for larger final lining forces for slow soil creep after the excavation of the heading. This trend changes during the subsequent excavation steps. Finally, there are larger lining forces for fast creeping soil. This observation is ascribed to the load-dependent influence of shotcrete creep. For initially small loading, the creep strains are small. With increasing loading, the influence of creep of shotcrete increases. Hence, the reduction of the loading caused by shotcrete creep evolves later for slow loading processes, whereas it evolves earlier for fast loading processes. However, as opposed to the crown, the trend does not change in the bench, as the unloading effect of shotcrete creep and shrinkage is less visible there. Anyway, the comparison of NLE and LE analysis reveals that there are only minor differences in the lining forces.

5.2.3 Concluding remarks

It was shown in Section 3.4.2 (see Figure 3.29) that the choice of the elastic law has a significant influence when the hydrostatic stresses and the volumetric strains, respectively, are changing considerably. However, the numerical results presented in Sections 5.2.1 and 5.2.2 revealed that the differences of the results from analyses using the nonlinear elastic law and analyses using a linear elastic law for the soil are moderate. Generally, in tunneling processes, the ground deformation and, hence, the stress redistribution, is increasingly confined by the hardening of the shotcrete lining. Consequently, in excavation of tunnels

there are neither large changes of hydrostatic stresses nor of respective volumetric strain. Therefore, the effect of the choice of the elastic law is small.

Nevertheless, the numerical results presented in Section 5.2.2 illustrate the strong dependence of changes of the geological conditions on the structural response. Hence, accurate estimation of geological conditions is essential.

Chapter 6

Summary, conclusions, and outlook

This work has dealt with numerical simulations of the excavation of tunnels according to the NATM. A review of the current tunneling practice and the possibilities of computational mechanics has illustrated the usefulness of the application of FE simulations to excavation processes for qualitative purposes as regards the influence of construction schemes or of additional tunnel support means.

In the light of inevitable uncertainties regarding the soil properties and geologic conditions, simple elasto-viscoplastic material models accounting for hardening/softening for granular and cohesive soil, respectively, were developed.

The developed material models were shown to be useful for numerical simulation of tunneling. This statement is based on the fact that the phenomena observed in laboratory experiments concerning the excavation of a tunnel were also observed in the results from respective numerical analyses.

Numerical applications to tunneling processes are contained in Chapter 5. These applications refer to the influence of horizontal jet grouting prior to the excavation in granular and cohesive soil, respectively, and the effect of the choice of the elastic law on the response of the structure.

Numerical results such as the ones presented in Section 5.1 provide insight into the influence of ground improvement as regards the apparent geological conditions. Structural interactions can be investigated and effects of different construction schemes or ground improvement strategies with regards to apparent ground conditions can be assessed by numerical investigation. Hence, optimization of tunneling processes with respect to apparent ground conditions is feasible.

However, taking into account the inevitable uncertainties associated with the required input data of soil for these numerical analyses, the obtained results provide more qualitative rather than quantitative information. Additionally, the lack of experimental evidence on cemented cohesive soil makes assumptions on respective input data for numerical analyses necessary. Consequently, the numerical results obtained from these analyses should serve as an estimate of the real structural response. Nevertheless, with sufficiently accurate input

data at hand, also qualitative statements regarding the structural effect of application of specific tunnel support means are feasible. Other findings reported in Chapter 5 are that

- long-term creep of early-age cement-based materials is negligible in the presented numerical analyses, and

- the description of the elastic behavior by a linear or non-linear elastic law, respectively, does not influence the structural response to tunneling considerably. Instead, an accurate determination of primary soil conditions is found to be highly important with respect to the structural response to tunneling.

As regards the future work, some recommendations are given in the following:

- Hydromechanical effects, which may alter the behavior of the soil crucially, and, hence, may dominate the structural response to the excavation, should be accounted for in tunneling simulations. A respective three-phase model addressing the transportation problem for two-dimensional problems is given, e.g., in [65].

- Experimental determination of intrinsic material functions for soilcrete with different kinds of aggregate is necessary in order to obtain more realistic numerical results for jet grouting processes in cohesive soil.

- Another ground improvement technique is soil freezing, which is increasingly used for temporary stabilization of the soil surrounding an excavation. Hence, there is a need for experimental determination of intrinsic material functions for frozen soil and for a respective constitutive model. With such a model and sufficient experimental data at hand, structural effects of ground freezing can be studied numerically and a comparison between different ground improvement techniques, as well as the optimization of the tunnel construction process with ground freezing become feasible.

Bibliography

[1] S. Akutagawa, S. Sakurai, and K. Ogawa. An analytical and experimental investigation on stability of underground openings. In J.X. Yuan, editor, *Proceedings of the 9th International Conference on Computer Methods and Advances in Geomechanics*, pages 1495–1500, Wuhan, China, 1997. Balkema, Rotterdam, The Netherlands.

[2] J.P. Bardet. *Experimental Soil Mechanics*. Prentice Hall, New Jersey, 1997.

[3] Z. Bažant and S. Baweja. Short form of creep and shrinkage prediction model B3 for structures of medium sensitivity. *Materials and Structures*, (29):587–593, 1996.

[4] Z.P. Bažant, T.B. Belytschko, and T.P. Chang. Continuum theory for strain softening. *Journal of Engineering Mechanics (ASCE)*, 110:1666–1692, 1984.

[5] Z.P. Bažant, A.B. Hauggard, S. Baweja, and F.-J. Ulm. Microprestress solidification theory for concrete creep, part I: Aging and drying effects. *Journal of Engineering Mechanics, ASCE*, 123(11):1188–1194, 1997.

[6] L. Bjerrum. Enginering geology of Norwegian normally-consolidated marine clays as related to settlements of buildings. *Geotechnique*, 17:81–118, 1967.

[7] H. Bock and P. Hartkorn. Zum Stand der in-situ-Spannungsmessungen für den Tunnelbau [Current state of in-situ-stress measurements in tunneling]. *Felsbau*, 13(6):363–366, 1995. In German.

[8] R.I. Borja, R.A. Regueiro, and T.Y. Lai. FE modelling of strain localization in soft rock. *Jounal of Geotechnical and Geoenvironmental Engineering*, 126(4):1–9, 2000.

[9] R.I. Borja and C. Tamagnini. Numerical implementation of a mathematical model for finite strain elastoplastic consolidation. In D.R.J. Owen, E. Oñate, and E. Hinton, editors, *Computational Plasticity, Proceedings of the 5th International Conference*, pages 1631–1640, Barcelona, 1997. CIMNE, Barcelona.

[10] Ch. Brandstätter. Experimentelle Untersuchung der Eigenschaften des Bodenmörtels, der beim Düsenstrahlverfahren entsteht [Experimental investigation of properties of jet grouted soil mass]. Master's thesis, Vienna University of Technology, Vienna, Austria, 2001. In German.

[11] Ch. Brandstätter, R. Lackner, Ch. Pichler, and H.A. Mang. Application of jet grouting in NATM tunneling. In S. Valliappan et al., editor, *Proceedings of the 1st Asian Pacific Congress on Computational Mechanics*, Sydney, Australia, 2001.

[12] R. Butterfield. A natural compression law for soils (an advance on *e*-log *p*). *Geotechnique*, 29:469–480, 1979.

[13] C. Callari, F. Auricchio, and E. Sacco. Finite-element implementation of a finite strain Cam-Clay model. In D.R.J. Owen, E. Oñate, and E. Hinton, editors, *Computational Plasticity, Proceedings of the 5th International Conference*, pages 1649–1656, Barcelona, 1997. CIMNE, Barcelona.

[14] A. Caquot. *Equilibre des massifs à frottement interne [Equilibrium of rock masses with internal friction]*. Gauthier-Villars, Paris, 1934. In French.

[15] P. Catharin. Hydratationswärme und Festigkeitsentwicklung [Hydration heat and strength evolution]. Technical Report 31, Forschungsinstitut des Vereins der österreichischen Zementfabrikanten, Vienna, Austria, October 1978. In German.

[16] A. Cividini and G. Gioda. Finite element undrained analysis with a pore pressure tension cut off. In G.A. Holzapfel, W. Moser, and G. Reichard, editors, *Advanced Numerical Analyses of Soilds and Structures, and Beyond*, pages 1–11. Verlag der Technischen Universität Graz, 2004.

[17] O. Coussy. *Mechanics of porous continua*. Wiley, Chichester, 1995.

[18] Y.F. Dafalias, M.T. Manzari, and M. Akaishi. A simple anisotropic clay plasticity model. *Mechanics Research Communications*, 29:241–245, 2002.

[19] E.H. Davis, M.J. Gunn, R.J. Mair, and H.N. Seviratne. The stability of shallow tunnels and underground openings in cohesive material. *Geotechnique*, 30(4):30–48, 1980.

[20] R. de Borst and H.B. Mühlhaus. Gradient-dependent plasticity: Formulation and algorithmic aspects. *International Journal for Numerical Methods in Engineering*, 35:521–539, 1992.

[21] J. Desrues and W. Hammad. Shear banding dependency on mean stress level in sand. In E. Dembicki, G. Gudehus, and Z. Sikora, editors, *Numerical Methods for Localization and Bifurcation of Granular Bodies*, pages 57–67. TU Gdańsk, Poland, 1989.

[22] F.L. DiMaggio and I.S. Sandler. Material models for granular soils. *Journal of Engineering Mechanics, ASCE*, pages 935–950, 1971.

[23] G. Duvaut and J.L. Lions. *Les Inequations en Mechanique et en Physique [The inequalities in mechanics and physics]*. Dunod, Paris, 1972. In French.

[24] D. Fitl. Der Tunnel Frankfurter Kreuz [The Frankfurter Kreuz tunnel]. *Felsbau – Rock and Soil Engineering*, 15(5):347–350, 1997. In German.

[25] G. Gioda and A. Cividini. Finite element analysis of time dependent effects in tunnels. In N. D. Cristescu and G. Gioda, editors, *Visco-plastic Behaviour of Geomaterials*, pages 209 – 244, International Centre for Mechanical Sciences, Udine, 1994. Springer Verlag, Wien.

[26] G. Gioda and L. Locatelli. Back analysis of the measurements performed during the excavation of a shallow tunnel in sand. *International Journal for Numerical and Analytical Methods in Geomechanics*, 23:1407–1425, 1999.

[27] G. Gioda and S. Sakurai. Back analysis procedure for the interpretation of field measurements in geomechanics. *International Journal for Numerical and Analytical Methods in Geomechanics*, 11:555–583, 1987.

[28] Keller Grundbau GmbH. The soilcrete - jet grouting proccess. brochure 67-3E.

[29] J. Graham and G.T. Houlsby. Anisotropic elasticity of a natural clay. *Geotechnique*, 33(2):165–180, 1983.

[30] A.E. Groen and R. de Borst. Three-dimensional finite element analysis of tunnels and foundations. *HERON*, 42(4):183–214, 1997.

[31] G. Guatteri, P. Mosiici, A. Koshima, and V. Doro-Altan. Application of jet grouting to tunnel portals and top headings in NATM tunnelling: Brazilian experience. In A.L. Bell, editor, *Grouting in the ground*, pages 455–471, London, England, 1994. Thomas Telford, London.

[32] G. Gudehus. Stoffgesetze [Material laws]. In U. Smoltczyk, editor, *Grundbautaschenbuch, 5. Aufl.*, pages 159–187. Ernst & Sohn, Berlin, 1996. In German.

[33] G. Gudehus and H.-J. Leinenkugel. Kriechen und Relaxation im Boden [Creep and relaxation in the ground]. *Der Bauingenieur*, 49:285–293, 1974. In German.

[34] K. Hashiguchi. Short communication: On the linear relations of V-$\ln p$ and $\ln v$-$\ln p$ for isotropic consolidation of soils. *International Journal for Numerical and Analytical Methods in Geomechanics*, 19:367–376, 1995.

[35] Ch. Hellmich. *Shotcrete as part of the New Austrian Tunneling Method: from thermochemomechanical material modeling to structural analysis and safety assessment of tunnels*. PhD thesis, Vienna University of Technology, Vienna, Austria, 1999.

[36] Ch. Hellmich, M. Lechner, R. Lackner, J. Macht, and H.A. Mang. Creep in shotcrete tunnel shells. In S. Murakami and N. Ohno, editors, *Creep in Structures 2000 – Proceedings of the 5th IUTAM Symposium on Creep in Structures*, pages 217–229, Nagoya, Japan, 2001. Kluwer Academic Publishers, Dordrecht.

[37] Ch. Hellmich, F.-J. Ulm, and H. A. Mang. Consistent linearization in finite element analysis of coupled chemo-thermal problems with exo- or endothermal reactions. *Computational Mechanics*, 24(4):238–244, 1999.

[38] Ch. Hellmich, F.-J. Ulm, and H. A. Mang. Multisurface chemoplasticity I: Material model for shotcrete. *Journal of Engineering Mechanics (ASCE)*, 125(6):692–701, 1999.

[39] R. Hill. Acceleration waves in solids. *Journal of the Mechanics and Physics of Solids*, 10:1–16, 1962.

[40] A. Hillerborg, M. Modeer, and P.E. Petersson. Analysis of crack formation and crack growth in concrete by means of fracture mechanics and finite elements. *Cement and Concrete Research*, 6:773–782, 1976.

[41] G. T. Houlsby. The use of a variable shear modulus in elastic-plastic models for clays. *Computers and Geotechnics*, 1:3–13, 1985.

[42] Th. Huemer, R. Lackner, and H.A. Mang. Implementation and application of an algorithm for adaptive finite element analysis of concrete plates. In Z. Bittnar, G. Pijaudier-Cabot, and B. Gérard, editors, *Mechanics of Quasi-Brittle Materials and Structures*, Prague, Czech Republic, March 1999. Hermes Science Publications, Paris.

[43] J. Jaky. A nyugalmi nyomas tenyezoje [The coefficient of earth pressure at rest]. *Magyar Mernok es Epitesz-Egylet Kozlonye*, 1944. In Hungarian.

[44] M. Jiràsek and Th. Zimmermann. Analysis of rotating crack model. *Journal of Engineering Mechanics (ASCE)*, 124(8):842–851, 1998.

[45] M. Kahl. *Primär- und Sekundärspannungszustände in überkonsolidiertem Ton [Primary and secondary stress states in overconsolidated clay]*. PhD thesis, Technical University of Braunschweig, Germany, 1991. In German.

[46] Y. Klausner. *Fundamentals of Continuum Mechanics of Soils*. Springer Verlag, New York, 1991.

[47] W.T. Koiter. *General theorems for elastic-plastic solids*, volume I, chapter IV, pages 167–218. North-Holland Publishing Company, Amsterdam, 1960.

[48] D. Kolymbas. Vereinfachte statische Berechnung der Tunnelfirste [Simplified static analysis of the tunnel crown]. *Rock Mechanics*, 14(4), 1982. In German.

[49] R. Lackner, Ch. Hellmich, and H.A. Mang. Constitutive modeling of cementitious materials in the framework of chemoplasticity. *International Journal for Numerical Methods in Engineering*, 53(10):2357–2388, 2002.

[50] P. V. Lade and C. T. Liu. Experimental study of drained creep behaviour of sand. *Journal of Engineering Mechanics*, 124(8):912–920, 1998.

[51] P.V. Lade and S. Inel. Rotational kinematic hardening model for sand. In Pietruszczak and Pande, editors, *Numerical Models in Geomechanics*, pages 9 – 14. Balkema, Rotterdam, 1997.

[52] P.V. Lade and J.A. Yamamuro. Undrained sand behavior in axisymmetric tests at high pressures. *Jounal of Geotechnical Engineering*, 122(2):120–129, 1996.

[53] T.Y. Lai, R.I. Borja, B.G. Duvernay, and R.L. Meehan. Capturing strain localization behind a geosynthetic-reinforced soil wall. *International Journal for Numerical and Analytical Methods in Geomechanics*, 27:425 – 451, 2003.

[54] H.-J. Lang and J. Huder. *Bodenmechanik und Grundbau [Soil mechanics and foundation engineering]*. Springer, Berlin–Heidelberg,Germany, 1990.

[55] R.W. Lewis and B.A. Schrefler. *The finite element method in the static and dynamic deformation and consolidation of porous media*. John Wiley & Sons, Chichester, 2 edition, 1998.

[56] H. Liebsch and C. Haberland. Soft ground tunnelling in urban areas by NATM. *Felsbau – Rock and Soil Engineering*, 16(2):78–90, 1998.

[57] B. Maidl. *Handbuch des Tunnel- und Stollenbaus [Handbook of tunneling and mining]*, volume 1. Glückauf, Essen, Germany, 1984. In German.

[58] T. Marcher and P.A. Vermeer. Macromodelling of softening in non-cohesive soils. In P.A. Vermeer, S. Diebels, W. Ehlers, H.J. Herrmann, S. Luding, and E. Ramm, editors, *Continuous and discontinuous modelling of cohesive-frictional materials, Lecture Notes in Physics*, volume 568, pages 89–108. Springer, Berlin, 2001.

[59] P. Melix. *Modellversuche und Berechnungen zur Standsicherheit oberflächennaher Tunnel [Experiments and computations concerning the stability of shallow tunnels]*. PhD thesis, Universität Karlsruhe, Germany, Karlsruhe, 1986. In German.

[60] H.B. Mühlhaus and L. Vardoulakis. The thickness of shear bands in granular materials. *Geotechnique*, 33(3):271–283, 1978.

[61] L. Müller-Salzburg and E. Fecker. Grundgedanken und Grundsätze der "Neuen Österreichischen Tunnelbauweise" [Fundamental concepts and principles of the New Austrian Tunneling Method]. Felsmechanik Kolloquium, pages 247–262, Karlsruhe, Germany, 1978. Trans Tech Publications. In German.

[62] R. Nova, R. Castellanza, and C. Tamagnini. A constitutive model for bonded geomaterials subject to mechanical and/or chemical degradation. *International Journal for Numerical and Analytical Methods in Geomechanics*, 27:705 – 732, 2003.

[63] J. Oliver. Modelling strong discontinuities in solid mechanics via strain softening constitutive equations. Part 1: Fundamentals. *International Journal for Numerical Methods in Engineering*, 39:3601–3623, 1996.

[64] J. Oliver. Modelling strong discontinuities in solid mechanics via strain softening constitutive equations. Part 2: Numerical simulation. *International Journal for Numerical Methods in Engineering*, 39:3601–3623, 1996.

[65] G. Öttl. *A three-phase FE-model for dewatering of soils by means of compressed air.* PhD thesis, University of Innsbruck, Austria, 2003.

[66] R.H.G. Parry. Triaxial compression and extension tests on remoulded saturated clay. *Geotechnique*, 10:166–180, 1960.

[67] B. Pichler, R. Lackner, and H.A. Mang. Soft-computing-based parameter identification as the basis for prognoses of the structural behavior of tunnels. In G. Beer, editor, *Numerical Simulation in Tunneling*, pages 201 – 223. Springer, Berlin, 2003.

[68] B. Pichler and H.A. Mang. Parameter identification for sophisticated material models by means of iterative back analyses based on soft computing. In Z. Waszczyszyn et al., editor, *CD-ROM Proceedings of the 2nd European Conference on Computational Mechanics*, Cracow, Poland, 2001.

[69] C. Pichler, R. Lackner, L. Martak, and H.A. Mang. Optimization of jet-grouted support in NATM tunneling. In N. Bicanić, R. de Borst, H.A. Mang, and G. Meschke, editors, *Computational Modelling of Concrete Structures, Proceedings of the EURO-C 2003 Conference*. Balkema, Rotterdam, 2003. To appear.

[70] Ch. Pichler, R. Lackner, Y. Spira, and H.A. Mang. Thermochemomechanical assessment of ground improvement by jet grouting in tunneling. *Journal of Engineering Mechanics (ASCE)*, 129(8):951–962, 2003.

[71] L. v. Rabcewicz. *Gebirgsdruck und Tunnelbau [Ground Pressure and Tunnelling]*. Springer, Vienna, Austria, 1944. In German.

[72] R.A. Regueiro and R.I. Borja. A finite element model of localized deformation in frictional materials taking a strong discontinuity approach. *Finite Elements in Analysis and Design*, 33:283–315, 1999.

[73] K.H. Roscoe and J.B. Burland. On the generalized stress strain behavior of 'wet' clay. In J. Heyman and F. A. Leckie, editors, *Engineering Plasticity*, pages 535–609. Cambridge University Press, Cambridge, England, 1968.

[74] W. Ruetz. Das Kriechen des Zementsteins im Beton und seine Beeinflussung durch gleichzeitiges Schwinden [Creep of cement in concrete and the influence of simultaneous shrinkage on this type of creep]. *Deutscher Ausschuß für Stahlbeton,* , Heft 183, 1966. In German.

[75] S. Sakurai and K. Takeuchi. Back analysis of measured displacements of tunnels. *Rock Mechanics and Rock Engineering*, 16:173–180, 1983.

[76] A. Schofield and P. Wroth. *Critical State Soil Mechanics*. McGraw-Hill, London, 1968.

[77] J. Sercombe, Ch. Hellmich, F.-J. Ulm, and H. A. Mang. Modeling of early-age creep of shotcrete. I: model and model parameters. *Journal of Engineering Mechanics (ASCE)*, 126(3):284–291, 2000.

[78] J.C. Simo. Algorithms for static and dynamic multiplicative plasticity that preserve the classical return mapping schemes of the infinitesimal theory. *Computer Methods in Applied Mechanics and Engineering*, 99:61–112, 1992.

[79] J.C. Simo and T.J.R. Hughes. *Computational inelasticity*. Springer, Berlin, Germany, 1998.

[80] J.C. Simo, J.G. Kennedy, and S. Govindjee. Non-smooth multisurface plasticity and viscoplasticity. Loading/unloading conditions and numerical algorithms. *International Journal for Numerical Methods in Engineering*, 26:2161–2185, 1988.

[81] J.C. Simo and G. Meschke. A new class of algorithms for classical plasticity extended to finite strains. Application to geomaterials. *Computational Mechanics*, 11:253–278, 1993.

[82] J.C. Simo, J. Oliver, and F. Armero. An analysis of strong discontinuities induced by strain-softening in rate-independent inelastic solids. *Computational Mechanics*, 12:277–296, 1993.

[83] J.C. Simo and R.L. Taylor. A return mapping algorithm for plane stress elastoplasticity. *International Journal of Numerical Methods in Engineering*, 22(3):649–670, 1986.

[84] P. Steinmann and K. Willam. Finite elements for capturing localized failure. *Archives of Applied Mechanics*, 61:259–275, 1991.

[85] D. Sterpi. An analysis of geotechnical problems involving strain softening effects. *International Journal for Numerical and Analytical Methods in Geomechanics*, 23:1427–1454, 1999.

[86] T. Tanaka, H. Mori, and M. Kikuchi. Finite deformation elastoplastic analysis of underground structures and retaining walls. In J.X. Yuan, editor, *Proceedings of the 9th International Conference on Computer Methods and Advances in Geomechanics*, pages 1465–1470, Wuhan, China, 1997. Balkema, Rotterdam, The Netherlands.

[87] K. Terzaghi. *Theoretical Soil Mechanics*. John Wiley & Sons, New York, 1943.

[88] F-J. Ulm. Couplages thermochémomécaniques dans les bétons : un premier bilan. [Thermochemomechanical couplings in concretes: a first review]. Technical report, Laboratoires des Ponts et Chaussées, Paris, France, 1998. In French.

[89] F.-J. Ulm and O. Coussy. Modeling of thermochemomechanical couplings of concrete at early ages. *Journal of Engineering Mechanics (ASCE)*, 121(7):785–794, 1995.

[90] F.-J. Ulm and O. Coussy. Strength growth as chemo-plastic hardening in early age concrete. *Journal of Engineering Mechanics (ASCE)*, 122(12):1123–1132, 1996.

[91] I. Vardoulakis, M. Goldscheider, and G. Gudehus. Formation of shear bands in sand bodies as a bifurcation problem. *International Journal for Numerical and Analytical Methods in Geomechanics*, 2:99–128, 1978.

[92] G.M. Vavrovsky. *Entspannung, Belastungsentwicklung und Versagensmechanismen bei Tunnelvortrieben mit geringer Überlagerung [Relaxation, evolution of loading and failure mechanisms for tunneling with low overburden]*. Dissertation, Montanuniversität Leoben, Leoben, Austria, 1987. In German.

[93] G.M. Vavrovsky. Gebirgsdruckentwicklung, Hohlraumverformung und Ausbaudimensionierung [development of ground pressure, deformation of cavity and dimensioning of lining]. *Felsbau – Rock and Soil Engineering*, 12:312–329, 1994. In German.

[94] P.A. Vermeer and R. de Borst. Non-associated plasticity for soils, concrete and rock. *HERON*, 29(3):3–64, 1984.

[95] W. Wissmann. Zur statischen Berechnung beliebig geformter Stollen- und Tunnelauskleidungen mit Hilfe von Stabwerkprogrammen [On static analysis of arbitrarily formed linings of mines and tunnels using computer programs for beam structures]. *Der Bauingenieur*, 43(1):1–8, 1968. In German.

[96] W. Wittke, B. Pierau, and C. Erichsen. Der Einsatz von Hochdruckinjektionen zur Baugrundverbesserung und für den Tunnelbau im Lockergestein [Application of jet grouting in ground improvement and tunneling in granular material]. In G. Riedmüller, W. Schubert, and S. Semprich, editors, *Düsenstrahlverfahren: Möglichkeiten und Grenzen der Anwendung*, Christian Veder Kolloquium, pages 155–183, Graz, Austria, 2000. Gruppe Geotechnik Graz, Graz. In German.

[97] F.H. Wittmann. *Creep and shrinkage mechanisms*, chapter 6, pages 129–161. Wiley, Chichester, 1982.

[98] D.M. Wood. *Soil Behaviour and Critical State Soil Mechanis*. Cambridge University Press, Cambridge, 1990.

[99] J.A. Yamamuro and P.V. Lade. Drained sand behavior in axisymmetric tests at high pressures. *Jounal of Geotechnical Engineering*, 122(2):109–119, 1996.

[100] M. Zytinski, M. F. Randolph, R. Nova, and C. P. Wroth. Short Communications: On modelling the unloading-reloading behaviour of soils. *International Journal for Numerical and Analytical Methods in Geomechanics*, 2:87–94, 1978.

Appendix A

Remarks on the consistency of geometrically linear versus nonlinear formulations for the Cam-Clay model

As described in Section 3.4, the elastic law of the Cam-Clay model is derived from a volumetric variable - hydrostatic pressure diagram defining also the hardening behavior of the material. Consequently, this approach implies a definition of the geometric formulation, depending on the choice of the volumetric variable. Therefore, volumetric deformation measures will be discussed in the following with respect to the underlying kinematic theory.

For the sake of simplicity, a Cam-Clay model shall be calibrated such that the yield surface exhibits no hydrostatic tensile resistance ($t = 0$). Therefore, the variables q_{CC} and q_0 refer directly to the actual hydrostatic preconsolidation pressure and to the initial hydrostatic preconsolidation pressure, respectively. The hardening law used for the Cam-Clay model is based on the assumption of a linear relation between the specific volume v and the natural logarithm of $(-p)$ (Figure A.1). The strain measure to be used in the problem must be related to the specific volume in accordance with the underlying kinematic description. According to [98], the evolution of the total volumetric strain is defined as

$$\dot{I}_1 = \frac{\dot{v}}{v} \, . \tag{A.1}$$

In Equation (A.1), the deformed volume is used as the reference volume, thus accounting for the large compressibility of soft soils. This formulation, however, implies large volumetric deformations. A geometrically linear formulation of the Cam-Clay model is

$$\dot{I}_1 = \frac{\dot{v}}{v_0} \, . \tag{A.2}$$

In Equation (A.2) it is assumed that no significant volume changes occur. This formulation has been used in this work.
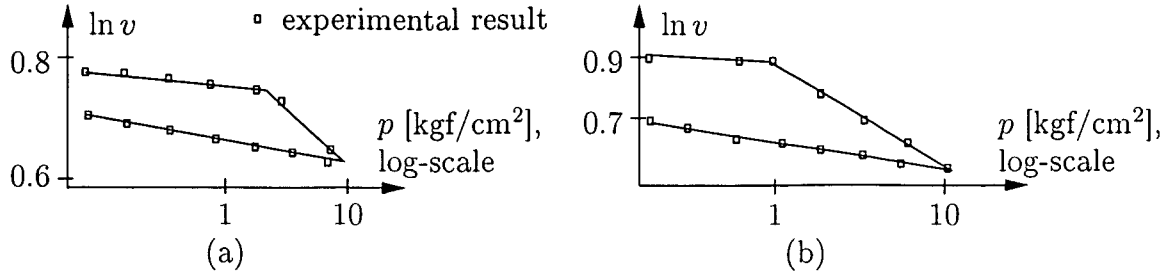
Figure A.1: Compressibility of clays: (a) Boston blue clay, (b) Chicago clay (from [12])

Another proposal for hardening of clays is based on experimental evidence contained in [12]. From these experiments, a linear relation between $\ln v$ and $\log p$ was extracted rather than a linear relation between v and $\log p$ (see Figure A.1). According to [12], such a relation between $\ln v$ and $\log p$ was observed for a wide range of hydrostatic pressures connected with large volumetric strains.

These observations serve as the basis for a geometrically nonlinear description using a linear relation between $\ln v$ and $\ln p$. Therefore, an evolution equation for the volumetric strains of the form

$$\dot{\bar{I}}_1 = \frac{\dot{v}}{v} \, , \tag{A.3}$$

as proposed by [98], is consistent with a linear $\ln v - \ln p$ diagram.

Using Equation (A.2) together with a linear $v - \ln(-p)$ diagram in a small-strain formulation and employing Equation (A.1), together with a linear $\ln v - \ln(-p)$ diagram, in a large-strain formulation, similar expressions for the volumetric elastic law and the hardening law can be derived. The extension of the volumetric stress-strain law from the small strain regime to the large strain regime and the similarities of the derived expressions are described below.

Small strain formulation. The volumetric stress-strain law restricted to small strains is based on a linear relation between v and $\ln(-p)$ according to Figure A.2(a). The rate of the total volumetric strain is obtained as

$$\dot{\bar{I}}_1 = \frac{\dot{v}}{v_0} \, . \tag{A.4}$$

The total volumetric strains are decomposed additively into an elastic and a plastic part. This results in the following relation:

$$\bar{I}_1 = \frac{(v - v_0)}{v_0} = \bar{I}_1^e + \bar{I}_1^p = \frac{(v - v_\kappa)}{v_0} + \frac{(v_\kappa - v_0)}{v_0} \, , \tag{A.5}$$

with v denoting the actual specific volume and v_κ standing for the specific volume corresponding to the initial hydrostatic pressure p_0. Inserting the expression for $(v - v_\kappa)$
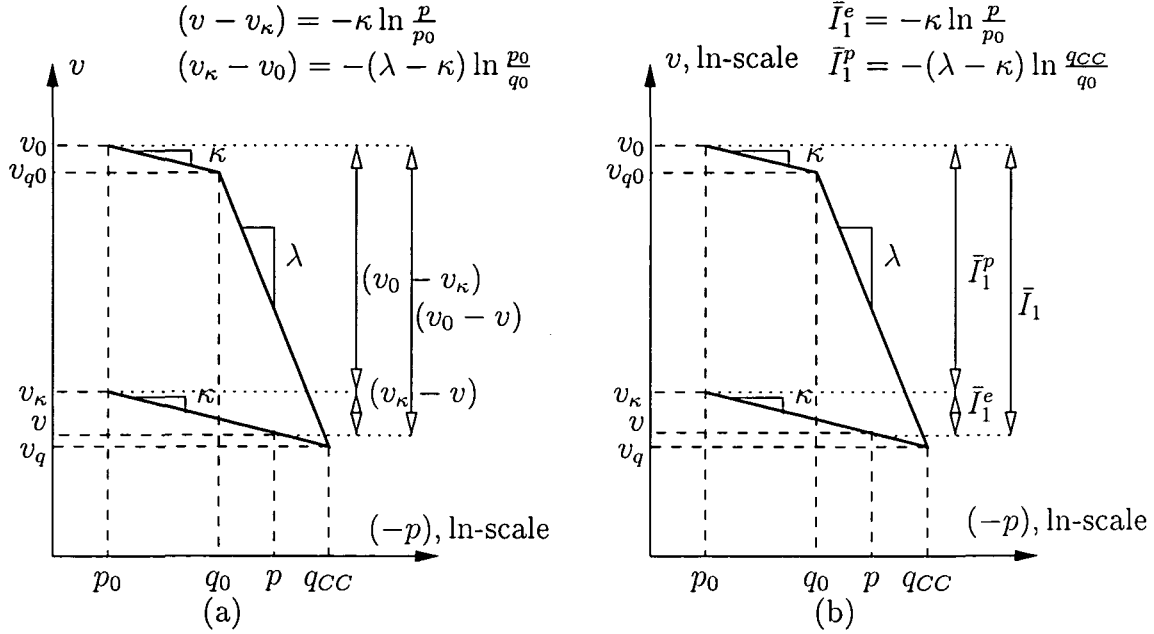
Figure A.2: Consistent extension of the linear relation between (a) v and $\ln(-p)$, valid for small strains, to the linear relation between (b) $\ln v$ and $\ln(-p)$, valid for large strains

(see Figure A.2(a)) into $\bar{I}_1^e = (v - v_\kappa)/v_0$ from Equation (A.5), the volumetric part of the hyperelastic relation

$$p = \frac{1}{3}I_1 = p_0 \exp\left(\frac{-v_0}{\kappa}\bar{I}_1^e\right) \tag{A.6}$$

is obtained. Analogously, inserting the expression for $(v_\kappa - v_0)$ (see Figure A.2(a)) into $\bar{I}_1^p = (v_\kappa - v_0)/v_0$ from Equation (A.5), the nonlinear hardening law

$$q_{CC} = q_0 \exp\left(\frac{-v_0}{\lambda - \kappa}\bar{I}_1^p\right) \tag{A.7}$$

is obtained, with q_0 denoting the initial preconsolidation pressure.

Large strain formulation. As far as the large deformation theory is concerned, it follows from the equation of definition of the rate of the total volumetric strains,

$$\dot{\bar{I}}_1 = \frac{\dot{v}}{v}, \tag{A.8}$$

that

$$\bar{I}_1 = \ln\frac{v}{v_0}. \tag{A.9}$$

This form is consistent with the logarithmic strains in the context of the multiplicative large strain theory from Figure A.2(b) and [78], [81], [13], [9]. From the additive split of

the elastic and the plastic volumetric strains , i.e., from

$$\bar{I}_1 = \bar{I}_1^e + \bar{I}_1^p = \ln \frac{v}{v_\kappa} + \ln \frac{v_\kappa}{v_0} \, , \tag{A.10}$$

and from Figure A.2(b), the laws for the volumetric elastic deformations and for hardening follow as

$$p = p_0 \exp\left(\frac{-1}{\kappa} \bar{I}_1^e\right) \tag{A.11}$$

and

$$q_{CC} = q_0 \exp\left(\frac{-1}{\lambda - \kappa} \bar{I}_1^p\right) \, , \tag{A.12}$$

respectively. Hence, up to the constant factor v_0, the stress-strain law for volumetric deformations and the hardening law are identical for the small strain and the large strain regime. Therefore, the extension of the model implemented for small strains to large strains is straightforward (cf. [34]).

Curriculum Vitae

Personal Details

Name	Yvonne Spira
Date and place of birth	26.08.1971, Kamp-Lintfort, Germany
Nationality	German
Family	2 children (*07.02.1999 and *21.11.2001)
Private address	1039 Massachusetts Avenue, Apt. 504
	Cambridge, MA 02138, USA

Education

1982 - 1991	Lise-Meitner high school, Geldern, Germany
1991 - 1997	Civil engineering, Ruhr-University Bochum, Specialization in the area: Structural engineering
09/1997	Graduation to Dipl.-Ing.
10/1994 - 03/1995	ERASMUS stipend as exchange student at the University of Wales, Swansea, United Kingdom

Scientific Experience

05/1995 - 03/1997	student assistant, Institute for Statics and Dynamics, Ruhr-University Bochum, Germany (Head of Institute: Prof. Krätzig)
10/1997 - 12/1998, 04/2000 - 09/2001, 02/2002 - 12/2003	research assistant, Institute for Strength of Materials, Vienna University of Technology, Austria (Head of Institute: Prof. Mang)
01/2004 - 08/2004	project assistant, Institute for Strength of Materials, Vienna University of Technology, Austria (Head of Institute: Prof. Mang)
09/2004 - today	research stay at the MIT in Cambridge, Massachusetts,USA with a mobility grant from the Akademisch-Soziale Arbeitsgemeinschaft Österreich